



Doctoral thesis

# Integrated Vehicle Dynamics Controller for Electric Traction Drives and Mechatronic Drivetrain Components

Martin Ringdorfer

---

Institute of Automation and Control  
Graz University of Technology

Supervisor: Univ. Prof. Martin Horn

Graz, October 2013

# Abstract

In “state-of-the-art” passenger cars, a large number of control systems (e.g. driver assistance and vehicle guidance systems) support the driver and other occupants. One such control system is “Electronic Stability Control” (ESC). This system is nearly undetectable for the driver as long as the motion of the car is consistent with the desired behavior of the car. In the case of undesired driving behavior or dangerous driving situations, ESC influences the vehicle motion by coordinated friction brake interventions. From the economic standpoint, the need for careful use of the available, environmentally friendly resources has gained remarkable importance in recent years. This led to the introduction of electric traction drives in the vehicle, including the integration of safety-related control systems that need to be adapted to the requirements of being both effective and energy saving.

The introduction of electric actuators (e.g. traction drives) can extend the existing vehicle dynamics controller functions in terms of recovering energy. Instead of converting the kinetic energy into thermal losses, it is useful to operate the traction drives as generators. This energy is used for charging the electrical energy storage system, which is known as energy recuperation. In some cases, the application of recuperation strategies may lead to overbraked wheels, which results in vehicle motion that does not match the driver’s expectations. Such situations are unfavorable in terms of driving comfort, energy recuperation and driving safety. Nevertheless, they require an interruption of energy recuperation to be replaced by an intervention of the vehicle dynamics controller. The recuperation discontinuity and the ensuing vehicle dynamics controller action should be substituted by combined traction machine control and friction brake control.

This thesis describes research conducted into the development of an integrated vehicle dynamics controller, especially for electric vehicles. The combined control of friction brakes and electric traction machines guarantees that most of the vehicle dynamics control actions are performed by utilizing electric traction machines. In addition in the case of insufficient brake actuator dynamics, the traction machines are applied to improve the brake actuator response.

The possibility of controlling single-wheel traction machines independently from each other leads to the opportunity to influence the vehicles yaw motion without friction brake interventions. These functional benefits extend the range of state-of-the-art “Energy Managers” and also bridge the gap to the ESC technologies that are available on today’s market. Demonstrating the advantages of electric yaw motion control demands a new yaw motion control structure. In the present work, a cascaded control structure was selected and utilized for vehicle yaw motion control. The performance of the derived yaw motion controller in combination with the wheel actuators was evaluated by means of standard driving maneuvers and the performance is compared here to a conventional electronic stability control system.

# Kurzfassung

Heutzutage besitzen konventionelle Personenfahrzeuge eine Vielzahl an Steuer- und Regelungssystemen (wie z.B. Fahrerassistenzsysteme), die den Fahrer unterstützen. Eines dieser Regelsysteme ist das sogenannte "Elektronische Stabilitätsprogramm" (ESC). Dieses System ist für die Fahrzeuginsassen kaum bemerkbar, solange die Fahrzeugbewegung im Einklang mit den Fahrereingaben steht. Im Falle von kritischen Fahrsituationen kann das ESC die Fahrzeugbewegung durch gezielte, radindividuelle Brems Eingriffe beeinflussen, um das Fahrzeug wieder in einen sicheren Zustand überzuführen. Neben den Sicherheitsaspekten steht unter anderem auch Energieeffizienz und Umweltfreundlichkeit von Kraftfahrzeugen im Mittelpunkt heutiger Fahrzeugentwicklungen. Darin ist auch einer der Gründe zu sehen, warum heutzutage vermehrt elektrische Traktionsantriebe in Fahrzeugen eingesetzt werden. Mit der Anwendung von Traktionsantrieben wurde auch die Idee geboren, diese zur Realisierung von Fahrzeugsicherheitsfunktionen im elektronischen Stabilitätsprogramm einzusetzen.

Mit der Einbeziehung von Traktionsantrieben in die Fahrdynamikregelung kann die Energieeffizienz des Fahrzeuges gesteigert werden. Wird die kinetische Energie des Fahrzeuges bei Bremsvorgängen in Form von elektrischer Energie gespeichert, so nennt man dies "Rekuperation". In einigen wenigen Fahrsituationen kann dies aber auch zur ungewollten Beeinflussung der Fahrzeugbewegung führen. Diese Bewegungsbeeinflussungen sind auch nachteilig für den Fahrkomfort und die Fahrzeugsicherheit. Bei aktuell auf dem Markt verfügbaren Systemen wird daher die Rekuperation beendet, um den beabsichtigten Fahrzustand mit Hilfe eines Fahrdynamikreglereingriffes wieder zu erreichen. Diese Unterbrechung soll mit Hilfe der kombinierten Regelung von Traktionsmaschinen und Radbremsen verhindert werden.

Diese Dissertation befasst sich mit der Entwicklung eines integrierten Fahrdynamikreglers, der speziell für Hybrid- und Elektrofahrzeuge mit Einzelradtraktionsantrieben geeignet ist. Die kombinierte Regelung von konventionellen Reibungsbremsen und elektrischen Traktionsmaschinen ermöglicht es, dass eine überwiegende Mehrzahl der Fahrdynamikreglereingriffe mit Hilfe der Traktionsmaschinen realisiert werden kann. Dies ist wiederum vorteilhaft für die Fahrsicherheit (Bremswegreduktion), zumal die Elektromaschinen auch Vorteile hinsichtlich Dynamik gegenüber Reibungsbremsen besitzen.

Basierend auf der kombinierten Antriebsregelung bietet die Anwendung von Einzelradantrieben zusätzlich die Möglichkeit, das Fahrzeuggierverhalten ohne die Zuhilfenahme der Bremse zu beeinflussen. Diese funktionellen Vorteile können zur Erweiterung heutiger Fahrzeug-Betriebsstrategien genutzt werden. Es zeigt sich, dass die Vernetzung von Betriebsstrategie und Fahrdynamikregelsystemen neben der Steigerung des Fahrvergnügens auch einen Mehrwert an Fahrsicherheit (Unterdrückung von Über-/Untersteuerreaktionen) generieren. Um die Potentiale, die durch den Einsatz von Elektromaschinen entstehen,

darstellen zu können, wurde zusätzlich zum Antriebsstrangregler ein Gierbewegungsregler in Form einer kaskadierten Reglerstruktur entwickelt. Diese ermittelt die Sollwerte, die mit Hilfe einer kombinierten Regelung der Antriebsstrangaktuatoren so umgesetzt werden, dass Fahrvergnügen, Energieeffizienz und Fahrsicherheit vereint werden können. Die dadurch entstandenen Vorteile gegenüber vorhandenen Fahrstabilitätsprogrammen werden mittels standardisierten Testmanövern bestätigt.

## Statutory declaration

I declare that I have authored this thesis independently, that I have not used other than the declared sources / resources and that I have explicitly marked all material which has been quoted either literally or by content from the used sources.

# Acknowledgement

The research for this thesis was conducted while I was employed at the “Magna Project House Europe” and at the “Alpen-Adria University Klagenfurt” and was supported by a grant from the “Austrian Research Promotion Agency (FFG)”.

Special thanks are due to Univ. Prof. Martin Horn, whose enthusiasm, encouragement and challenging questions contributed substantially to this thesis and to Univ. Prof. Peter Fischer for his interests in this topic. I would also like to express my gratitude to my colleagues at the “Control and Mechatronic Systems Group” at the Alpen-Adria University Klagenfurt as well as at the “Institute of Automation and Control” at the Graz University of Technology. They provided me a positive and supportive environment for my research and studies, and also helped me see beyond my own perspective on many occasions.

From the Magna Project House Europe, I would like to acknowledge in particular Dipl.-Ing. Manfred Speiser, who supported my work on such an interesting topic.

Of course, I must not to forget to thank my family, who gave me the inspiration and energy I needed to complete this challenging project.

Finally, I would like to thank all of my friends and colleagues who are not explicitly mentioned, but who have supported me throughout this project.

*Many thanks to all of you!*

# Contents

<b>1</b>	<b>Introduction</b>	<b>13</b>
<b>2</b>	<b>Vehicle dynamics control systems</b>	<b>22</b>
2.1	Antilock braking system - ABS	22
2.2	Electronic stability control system - ESC	26
2.3	Control system architecture	28
2.3.1	State-of-the-art electronic stability control system architecture	28
2.3.2	Electronic stability control system for electric vehicles using single-wheel propulsion	29
<b>3</b>	<b>Tire models and vehicle models</b>	<b>32</b>
3.1	Tire force characteristics	32
3.2	Tire force approximation for wheel slip controller design	36
3.3	Tire force approximation for vehicle stability analysis	36
3.4	Wheel motion model	37
3.5	Lateral vehicle models	39
3.5.1	Linear bicycle model	39
3.5.2	Non-linear two-track model	40
<b>4</b>	<b>Drivetrain actuators</b>	<b>42</b>
4.1	Friction brake	42
4.2	Synchronous machines	44
4.2.1	Classification of synchronous machines	44
4.2.2	Mathematical representation of a synchronous machine	47
4.2.3	Torque control of a synchronous machine with interior magnets	49
4.2.4	Drag torque generation of a synchronous machine with interior magnets during electrical system faults	55
4.2.5	Machine approximation for wheel slip controller design	58
<b>5</b>	<b>Combined actuator control</b>	<b>60</b>
5.1	State-of-the-art wheel motion control	60
5.1.1	Conventional vehicle	60
5.1.2	Electric vehicle	60
5.2	Wheel motion control for electric vehicles using combined actuator control	65
5.2.1	Fail-silent properties of combined actuator control	69

<b>6</b>	<b>Wheel slip control</b>	<b>71</b>
6.1	Wheel slip controller design . . . . .	71
6.2	Simulation results . . . . .	76
6.2.1	Comparison between ABS and HAS . . . . .	76
6.2.2	Robustness tests . . . . .	82
6.3	Test bench results . . . . .	82
6.3.1	Test procedure . . . . .	83
6.3.2	Test results . . . . .	83
<b>7</b>	<b>Lateral vehicle dynamics control</b>	<b>90</b>
7.1	Reference value computation for yaw motion control . . . . .	90
7.2	Yaw motion control . . . . .	92
7.2.1	Sliding mode yaw rate control . . . . .	92
7.2.2	Torque coordination . . . . .	93
7.2.3	Sliding mode vehicle sideslip angle control . . . . .	99
7.3	Performance analysis of the vehicle yaw motion controller . . . . .	101
7.4	Vehicle motion control during standardized test maneuvers . . . . .	103
7.4.1	Emergency braking . . . . .	103
7.4.2	Steering wheel step maneuver . . . . .	104
7.4.3	Power lift-off . . . . .	107
7.4.4	Sine with dwell . . . . .	110
7.4.5	Double lane change . . . . .	114
7.4.6	Summary . . . . .	116
<b>8</b>	<b>Vehicle dynamics control during electrical faults</b>	<b>117</b>
8.1	Electrical system faults during braking . . . . .	117
8.1.1	Braking under low- $\mu$ conditions . . . . .	117
8.1.2	Braking under high- $\mu$ conditions . . . . .	119
8.1.3	Braking under split- $\mu$ conditions . . . . .	121
8.2	Electric system faults during straight-ahead driving . . . . .	125
8.3	Electric system faults during vehicle cornering . . . . .	128
8.4	Summary . . . . .	131
<b>9</b>	<b>Conclusion and Outlook</b>	<b>132</b>
<b>A</b>	<b>Sliding mode control</b>	<b>134</b>
<b>B</b>	<b>Test bench</b>	<b>139</b>
B.1	Test bench layout . . . . .	139
B.2	Test bench control layout . . . . .	141
B.3	Wheel slip control with on/off-valves . . . . .	141
B.4	Stick slip effects . . . . .	143
B.5	Load force variation . . . . .	143

# Nomenclature

<i>Abbreviation</i>	<i>Explanation</i>
ABS	Antilock Braking System
AC	Alternating Current
AFS	Active Front Steering
ASC	Acceleration Slip Control(ler)
COG	Center Of Gravity
DC	Direct Current
ECU	Electronic Control Unit
ED	Electric Drive
EM	Energy Manager / Energy Management
EMF	Electromotive Force
ESC	Electronic Stability Control
ESS	Energy Storage System
ETD	Electric Traction Drive
EV	Electric Vehicle
F / R	Front / Rear
FOC	Field-Oriented Control
HAS	Hybrid Actuator System
HCU	Hybrid Control Unit
HEV	Hybrid Electric Vehicle
IEA	International Energy Agency
L / R	Left / Right
MTPA	Maximum Torque Per Ampere
min / max	Minimum/maximum
PHEV	Plug-in Hybrid Electric Vehicle
PI	Proportional-Integral
PMSM	Permanent Magnet Synchronous Machine
PT1	First order lag element
OEM	Original Equipment Manufacturers
ROA	Region Of Attraction
SM	Sliding Mode
SOC	State Of Charge
VDC	Vehicle Dynamics Control(ler)

<i>Symbol</i>	<i>Unit</i>	<i>Explanation</i>
$F_{\max}$	N	maximum tire force
$F_{\infty}$	N	tire force at $\lambda=1$ or $\alpha=\pi/4\text{rad}$
$F_x$	N	longitudinal tire force
$F_y$	N	lateral tire force
$F_z$	N	vertical tire force
$F_{z,N}$	N	nominal vertical tire force
$J_{\text{veh}}$	$\text{kgm}^2$	vehicle moment of inertia
$J_y$	$\text{kgm}^2$	wheel moment of inertia (y-axis)
$J_z$	$\text{kgm}^2$	vehicle moment of inertia (z-axis)
$a_x$	$\text{m/s}^2$	longitudinal acceleration
$a_y$	$\text{m/s}^2$	lateral acceleration
$c_{\lambda}$	N	longitudinal tire stiffness
$c_{\alpha}$	N/rad	lateral tire stiffness
$g$	$\text{m/s}^2$	gravitational acceleration
$h_{\text{COG}}$	m	distance between road and center of gravity
$l_F$	m	distance between center of gravity and front axle
$l_R$	m	distance between center of gravity and rear axle
$l_T$	m	track width
$m$	kg	vehicle mass
$r$	m	tire radius
$v$	m/s	vehicle velocity
$v_{\text{whl}}$	m/s	wheel velocity
$x$	-	longitudinal coordinate
$y$	-	lateral coordinate
$z$	-	vertical coordinate
$\alpha$	rad	wheel sideslip angle
$\beta$	rad	vehicle sideslip angle
$\beta_d$	rad	reference vehicle sideslip angle
$\delta$	rad	wheel steering angle
$\delta_D$	rad	steering wheel angle (driver input)
$\lambda$	-	wheel slip
$\lambda_c$	-	critical wheel slip
$\lambda_d$	-	desired wheel slip
$\mu$	-	road surface friction coefficient
$\dot{\psi}$	rad/s	vehicle yaw rate
$\dot{\psi}_d$	rad/s	reference vehicle yaw rate
$\omega$	rad/s	angular wheel velocity

Table 1: Vehicle related symbols

<i>Symbol</i>	<i>Unit</i>	<i>Explanation</i>
$K_{\text{brk}}$	Nm/Pa	brake torque constant
$T$	Nm	yaw torque
$T_{\text{brk}}$	Nm	friction brake torque
$T'_{\text{brk,d}}$	Nm	energy management intended friction brake torque
$T_{\text{brk,d}}$	Nm	energy management intended friction brake torque (corrected by the torque coordinator)
$T_{\text{brk,p}}$	Nm	disc brake torque
$T_{\text{c}}$	Nm	friction brake controller torque
$T_{\text{d,d}}$	Nm	driver intended propulsion torque
$T_{\text{p}}$	Nm	feed-forward torque
$T'_{\text{td,d}}$	Nm	energy management intended electric propulsion torque
$T_{\text{td,d}}$	Nm	energy management intended electric propulsion torque (corrected by the torque coordinator)
$T_{\text{whl}}$	Nm	wheel torque
$T_{\text{z}}$	Nm	vehicle dynamics controller yaw torque
$T_{\text{z,FL}}, T_{\text{z,FR}},$ $T_{\text{z,RL}}, T_{\text{z,RR}}$	Nm	yaw torque potential of each wheel
$T_{\lambda}$	Nm	wheel slip controller torque
$p_{\text{act}}$	Pa	brake pedal pressure
$p_{\text{brk}}$	Pa	brake pressure
$p_{\text{d}}$	Pa	desired brake pressure
$t$	s	time
$\Delta\beta$	rad	sideslip angle dead zone
$\Delta\dot{\psi}$	rad/s	yaw rate dead zone
$\beta_{\text{iim}}$	rad	sideslip angle limit
$\beta_{\text{max}}$	rad	maximum achievable sideslip angle
$\tilde{\beta}$	rad	sideslip angle control error
$\phi$	-	boundary layer thickness
$\gamma$	-	weighting factor
$\tilde{\lambda}$	-	wheel slip control error
$\hat{\mu}$	-	equivalent road surface friction coefficient
$\tilde{\psi}$	rad/s	yaw rate control error
$\dot{\psi}_{\text{C}}$	rad/s	sideslip angle controller yaw rate
$\dot{\psi}_{\text{e,d}}$	rad/s	estimated desired yaw rate
$\sigma$	-	sliding variable
$\tau_{\text{b}}$	s	brake pressure time constant
$\tau_{\text{ed}}$	s	machine torque time constant

Table 2: Vehicle dynamics controller related symbols

<i>Symbol</i>	<i>Unit</i>	<i>Explanation</i>
$I_{dc}$	A	direct current-link current
$I_{max}$	A	maximum current
$L_d$	H	reluctance inductance
$L_q$	H	main inductance
$P$	-	number of pole pairs
$R$	$\Omega$	ohmic resistance
$T_i$	Nm	machine torque
$T_{i,d}$	Nm	desired machine torque
$T_m$	Nm	motor/generator drive torque
$T_{m,d}$	Nm	desired motor/generator drive torque
$T_{max}$	Nm	maximum motor/generator torque
$U_{dc}$	V	direct current-link voltage
$U_{max}$	V	maximum voltage
$i_a/i_b/i_c$	A	phase current
$i_d$	A	field current
$i_{d,d}$	A	desired field current
$i_q$	A	torque current
$i_{q,d}$	A	desired torque current
$i_\alpha, i_\beta$	A	transformed phase currents ( $\alpha, \beta$ -system)
$k_g$	-	gear stage ratio
$n$	1/s	machine speed
$n_n$	1/s	nominal machine speed
$u_a/u_b/u_c$	V	phase voltage
$u_\alpha, u_\beta$	V	transformed phase voltages ( $\alpha, \beta$ -system)
$u_d, u_q$	V	transformed phase voltages (d,q-system)
$\Phi$	Vs	permanent magnet flux
$\Phi_e$	Vs	flux produced by $i_d$ and $i_q$
$\Phi_{max}$	Vs	maximum allowed flux
$\omega_e$	rad/s	angular electric field velocity
$\xi$	-	saliency ratio

Table 3: Traction drive related symbols

<i>Symbol</i>	<i>Explanation</i>
$\mathcal{G}_{\text{brk}}(s)$	brake torque transfer function in $s$ -domain
$\mathcal{G}_{\text{ed}}(s)$	machine torque transfer function in $s$ -domain
$\mathcal{G}_{\lambda}(s)$	wheel slip transfer function in $s$ -domain
$J$	cost function
$\mathcal{L}$	Laplace operation
$\mathcal{P}$	hybrid actuator system controller weighting parameter set
$s$	Laplace variable
$u$	control input
$x$	state variable
$y$	system output

Table 4: Mathematical and control related symbols

# Chapter 1

## Introduction

From the time when pure muscle power was used for propulsion, continuing through the application of steam engines, and right up to the current stage of what we know as “modern means of transportation”, locomotion and mobility have always been important issues for mankind. Continuous innovation has been driven by the ongoing desire to extend the existing human limits and to improve the “state-of-the-art”.

Due to today’s economic wealth, vehicles have evolved from pure working machines to status symbols. International trading, fast-growing consumer markets and especially personal needs have caused the number of road participants to increase in the recent decades. The number of kilometers traveled per passenger and per year within the European Union is steadily increasing [Eur10]. For example, from 1995 to 2008 the number of “kilometers driven by utilizing a passenger car” increased by 21% (see Figure 1.1a). The growing number of road users requires improved traffic coordination and regulation. Nevertheless, the statistics also show that the increase in traffic volumes has also led to a disproportionate increase in the probability of being involved in a road accident. Therefore, additional measures must be taken to maintain safe traveling conditions. The statistics clearly show that the number of road accidents involving personal injuries decreased slightly between 1995 and 2008 (see Figure 1.1b). Separating the road accidents into accidents with fatalities and without fatalities, Figure 1.2a also shows that the number of accidents with fatalities has fortunately decreased within the same period as well. Both trends are the result of changing traveling habits and inventions related to new technologies and safety systems.

According to [Kra06] and [Kra07], vehicle safety can be subdivided into *active vehicle safety* and *passive vehicle safety*. Active safety involves all activities for accident prevention, while in contrast passive safety comprises all activities designed to mitigate the consequences of accidents. Based on these definitions, Figure 1.3 provides an overview of active and passive safety in the form of a matrix that, takes into account the different interacting factors and the levels of safety. Besides *human beings* and *environmental influences*, a third central factor exists - the *vehicle*. The influences of the vehicle and its potential to prevent or mitigating accidents are remarkable. Focusing on the vehicle-related measures for vehicle safety, many active safety systems have been introduced into today’s modern cars. Some examples are shown in Figure 1.4. A consideration of the time-line of the market launches of these active safety systems reveals a correlation to Figures 1.1b and Figure 1.2a. The significant decreases in the road accidents and fatalities

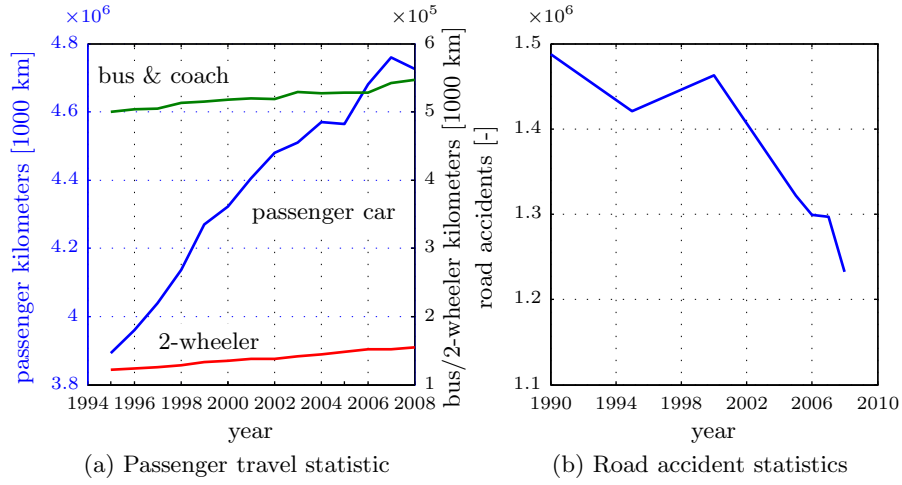


Figure 1.1: Passenger travel and road accident statistics [Eur10]

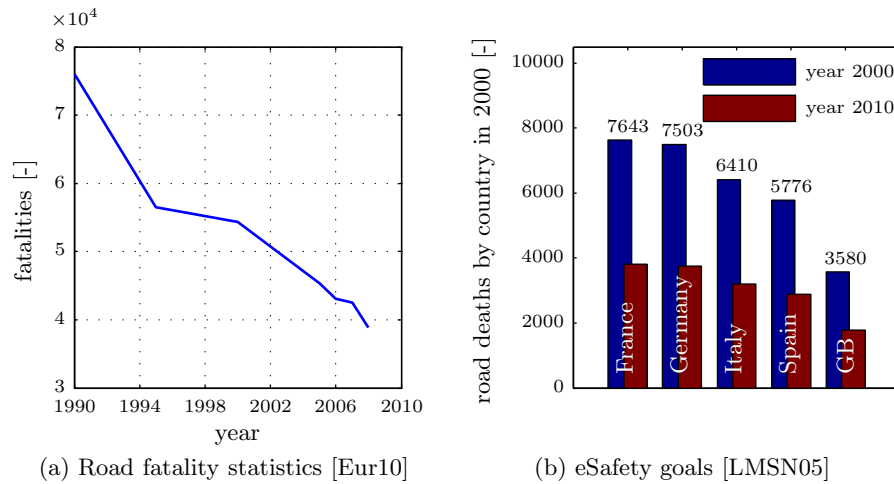


Figure 1.2: Road accident and fatality statistics

Safety of road traffic		
Human	Vehicle	Environment
Safety of road participant	Safety of means of transport	Safety of roads
Active safety (crash avoiding)		
Psychology	Driving safety	Road design
Medical science	Operating safety	Accident blackspots
Legal security	Detectability	Traffic law
Passive safety (crash result reducing)		
First aid	Self protection	Rescue service
Insurance protection	Protection of road users	Scene of accident Sideway disarming

Figure 1.3: Active and passive safety [Kra06]

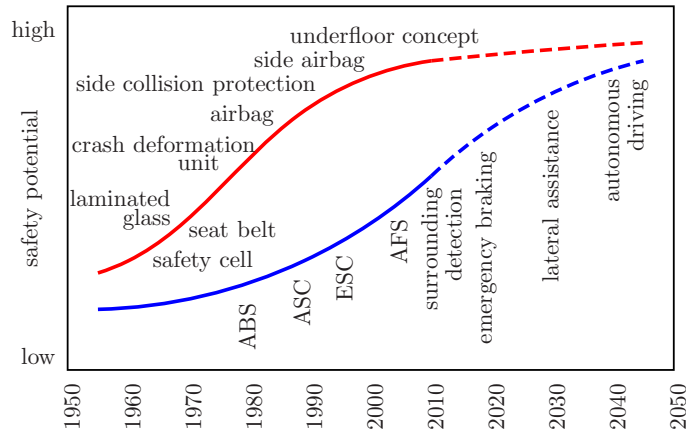
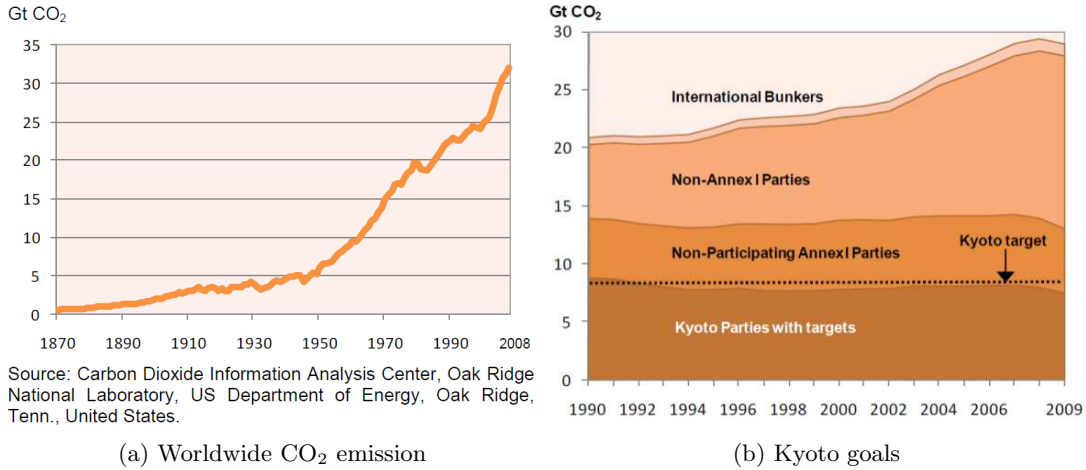


Figure 1.4: Active and passive safety systems [Sch04]

that occurred a few years after the introduction of Antilock Braking Systems (ABS) and Electronic Stability Control (ESC) offer clear proof of the value of such systems. The ABS is a subordinated control loop of the ESC which seeks to control the wheel slip by appropriately varying the wheel brake pressure in order to keep the wheel motion in a desired manner. The ESC in turn controls the vehicle motion by coordinating the wheel-related ABS interventions and by defining the reference value for the wheel slip [KN00]. Even though most safety systems are standard in European cars [BGA07], the European Union started the *eSafety initiative* [LMSN05], which sought to further reduce the number of road deaths by 50% by 2010 (based on the records of the year 2000) by encouraging a higher market penetration of vehicle safety systems. Figure 1.2b shows the ambitious goal of this initiative in the context of the most populous European countries. Statistics if the goals have been reached are not present yet.

Although modern passenger cars are equipped with various chassis or drivetrain control

Figure 1.5: CO<sub>2</sub> emission statistics [Int11a]

systems (e.g. Active Front Steering (AFS), ESC), mutual interference between these systems decreases their effectiveness. According to [Trä05], the separation of the system's regions of operation is therefore a crucial step towards guaranteeing safe driving (see Section 2.3). In order to reach the *eSafety* goal, an integrated control must be implemented to ensure that the interaction of the various safety systems will provide mutual support rather than mutual interference [Ise06, Ras09, Rie09]. Examples of such topologies can be found in [KAKH08] and [HE08]. In summary, it can be stated that the implementation of vehicle dynamics control devices and the assurance of their coordinated interaction are crucial for modern vehicles safety.

Beyond the aforementioned efforts dedicated to vehicle safety, the environmental aspects in terms of air pollution are also important. Data from the International Energy Agency (IEA) [Int11a] demonstrate clearly, that overall CO<sub>2</sub>-emissions have increased dramatically since the middle of the 19<sup>th</sup> century (see Figure 1.5a). To counteract this trend, the United Nations has sought to regulate the output of greenhouse gases, especially the CO<sub>2</sub>-emissions. The Kyoto protocol called for industrialized countries to reduce their emissions by 5.2% per year from 2008 to 2012. Even in countries that signed the protocol, emissions continue to increase, and calculations from the IEA have shown (see Figure 1.5b) that the emission goals cannot be reached without additional efforts. To reach these target values governments have to enact laws for emission reduction. For example in Austria, an adaptation of oil tax law<sup>1</sup> and the fuel consumption tax law<sup>2</sup> took place in 2008. According to [Bun08] the emission rate of vehicles is coupled to different tax classes. These taxes are paid by the vehicle holders, when registering their cars. This measure makes energy-efficient and environmentally friendly vehicles more attractive. Furthermore vehicle manufacturers are motivated (forced) to improve the emissions of their cars by meeting legal regulations as e.g. [Eur07]. The directive described in [Eur07] deals with the limits of engine exhaust gases due to fossil fuels. Within modern combustion

<sup>1</sup>Mineralölsteuergesetz

<sup>2</sup>Normverbrauchsabgabegesetz

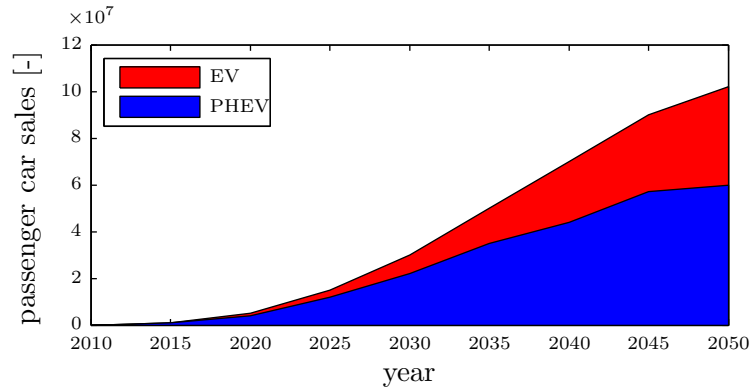


Figure 1.6: Annual global EV and PHEV sales [Int11b]

engines this is only possible with costly aftertreatments.

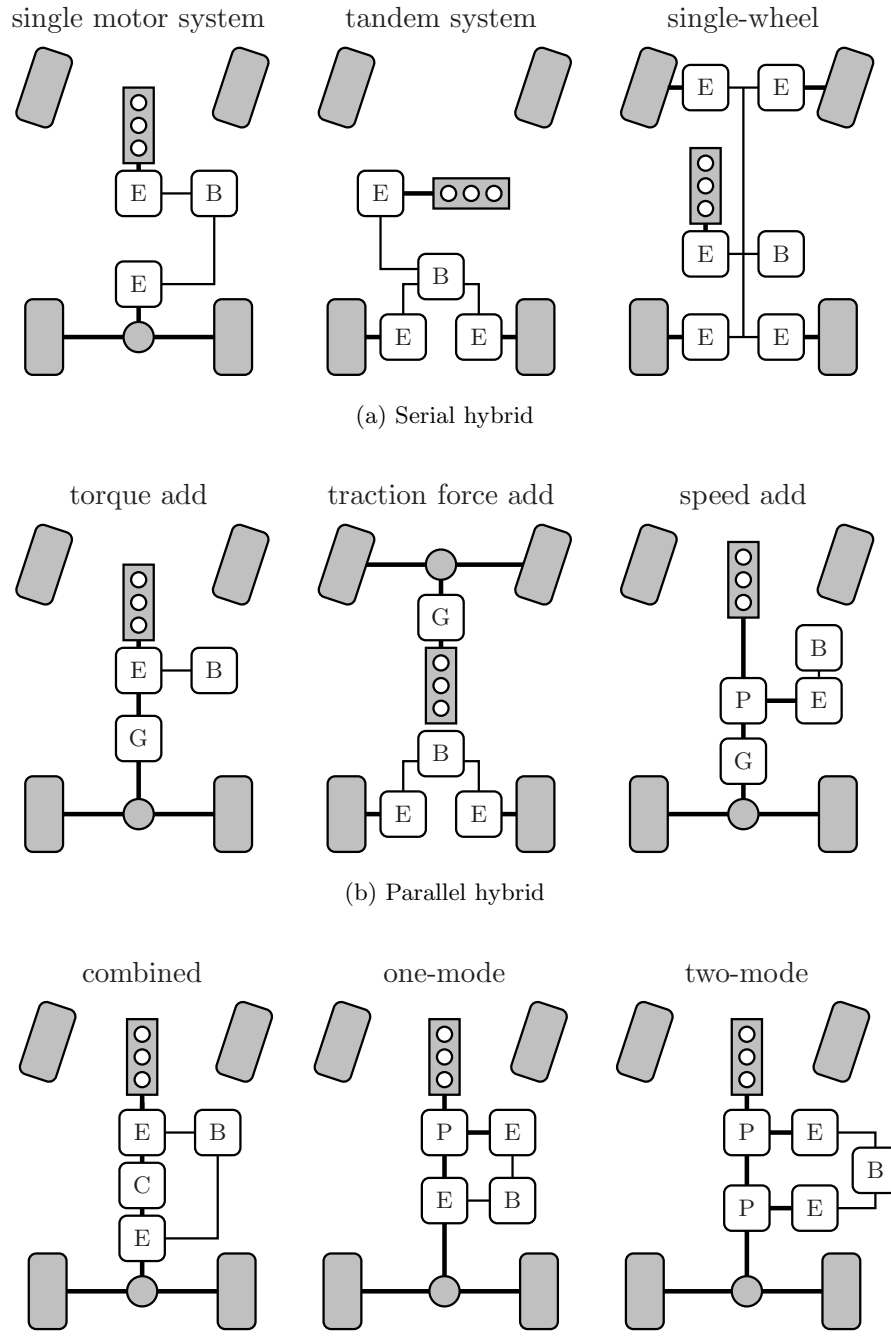
In contrast to such aftertreatment systems, other approaches being developed today concentrate on exploiting different energy sources [Int11b]. For example, vehicles which apply electric propulsion are known as Electric Vehicles (EV) or Hybrid Electric Vehicles (HEV). The number of electrically propelled vehicles is expected to increase from 2015 to 2050 (see Figure 1.6) [Int11b]. Based on the combination of combustion engine and electric motor(s)/generator(s), HEVs can be split up into the following categories:

- serial hybrid
- parallel hybrid
- power-split hybrid
- pure EV.

Figure 1.7 and [ERWL05] provide a rough overview of the complexity of different drivetrain topologies. In a *serial hybrid topology*, the Electric Drives (ED) or the Electric Traction Drives (ETD) must operate continuously during driving, while in a *parallel hybrid topology* permanent ETD operation is not mandatory. The required propulsion torque can also be supplied solely by the internal combustion engine. In a *power-split topology*, the mechanically required power is split up into a mechanical path and an electrical path. Measuring the degree of hybridization enables a second means of differentiation into the following categories

- micro hybrid
- mild hybrid
- full hybrid
- plug-in hybrid (PHEV)

The *micro hybrid* is very similar to conventional vehicles. Instead of a conventional starter motor, a more powerful starter machine is deployed. First, this machine helps to recuperate deceleration energy at a rate that is so low that passengers will not notice.



E...electric drive/electric traction drive; B...battery; G...gear box; P...planetary gear; C...clutch

(c) Power-split hybrid

Figure 1.7: Structures of electrical and hybrid electrical drivetrains [Hof10]



Figure 1.8: EV concept drivetrain (with kind permission of [Vol13])

Second, the starter is used to provide combustion engine start-stop functionality to save fuel while the vehicle is stopped at a traffic light, for example. However, this starter machine does not contain sufficient power for accelerating the vehicle.

A *mild hybrid* is similar to the micro hybrid, but the electric machine in this case is also able to support the combustion engine during start and acceleration, which is often known as *boosting*. However, pure electric traction is impossible.

In contrast, in a *full hybrid* vehicle it is possible to accelerate the vehicle with the traction machine only. For short distances, it is also practicable to drive 100% electrically.

However, longer distances require *plug-in hybrids*. These vehicles usually have the same topologies as full hybrids, but they feature larger battery capacities and a connection to external power supplies, which allows the charging of the batteries via a conventional power supply. The main source of propulsion is the electric traction machine, which is typically supported by a so-called *range extender*. A range extender is essentially a downsized combustion engine that charges the battery in the case of a low state-of-charge while the vehicle is driving 100% electrically. This kind of hybrid vehicle is the link to a fully electrified vehicle.

According to estimates, the market for EVs and PHEVs will continue to rise (see Figure 1.6). Initial serial production cars (for example the *Mitsubishi i-MiEV*, the *Tesla Roadster*) are already available on the market. In addition, drivetrain concepts such as in the *Volvo ReCharge* (see Figure 1.8) have already been presented at different motor shows, including [Ver13, NAI13].

The special feature of the *ReCharge* is the application of single-wheel traction drives. This new type of propulsion is the top class of EVs due to the different degrees of freedom it provides. Each wheel can be controlled independently, which offers the potential to improve the vehicle's energy efficiency and implement new safety-related functionalities.

In particular, new generations of ESC will not only control friction brakes, but rather will combine vehicle dynamics control and driving efficiency in a new Vehicle Dynamics Controller (VDC). Structures such as the one outlined in Figure 1.9 are seen as the future of vehicle concepts. The difficulty in introducing such topologies is that the conventional ESC functionality is no longer fully applicable. New control algorithms and new strategies for blending traction machine and friction brakes have to be developed. The experience gained in the last decade, as well as an additional focus on gaining auxiliary benefits from

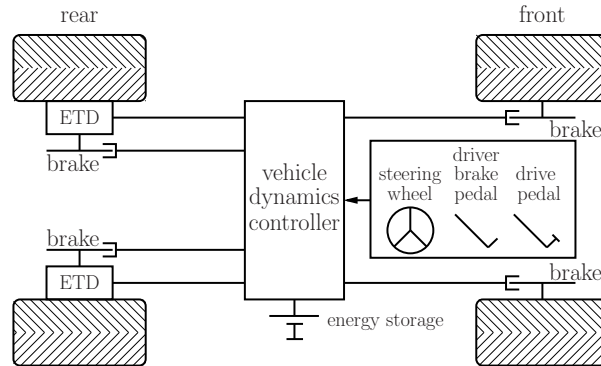


Figure 1.9: Electric vehicle topology

the application of energy-efficient traction machines, can lead to new performance levels.

The research for the present thesis focused on such new concepts that are required to harmonize energy efficiency and vehicle safety. The main objective was to develop a vehicle dynamics controller that would extend the functionality of present Energy Management (EM) systems, while maintaining driving safety. State-of-the-art model-based control concepts were used to achieve this goal.

The structure of the thesis is as follows (see Figure 1.10):

**Chapter 2** introduces the basics of vehicle dynamics and of vehicle dynamics control systems.

**Chapter 3** deals with basic mathematical models for tire forces, wheel and vehicle motion.

**Chapter 4** describes the drivetrain actuators that are applied for vehicle dynamics control.

**Chapter 5** deals with the combined control of traction machines and friction brake. Using the results from Chapter 4, it demonstrates how new performance levels can be achieved by applying intelligent interaction strategies (“blending strategies”).

**Chapter 6** focuses on the development of a robust wheel slip controller that accesses the hybrid actuator system which consists of single-wheel traction machines and conventional friction brakes.

**Chapter 7** discusses the utilization of a cascaded control structure to achieve robust vehicle dynamics control and depicts the potential of single-wheel actuation.

**Chapter 8** illustrates the risks and performance of the single-wheel traction machine applications in the case of selected electrical system faults.

The **Appendix** covers the basic elements for the methods required in the previous chapters.

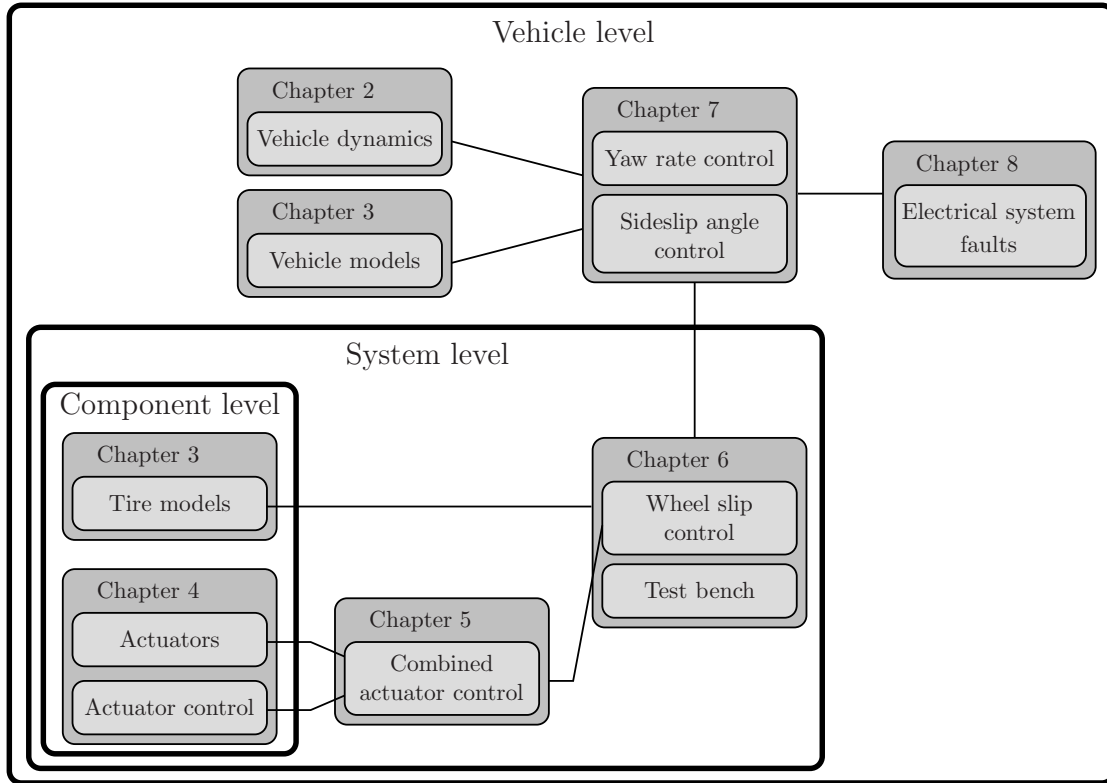


Figure 1.10: Thesis content structure

### Research environments

For the controller design and for explaining their operation principles, simplified mathematical models (implemented in Matlab/Simulink<sup>TM</sup>) are used.

The vehicle simulation results presented in this thesis were obtained using the vehicle dynamics simulation framework Dyna4<sup>TM</sup>.

To evaluate the performance of the developed wheel slip controller and its underlying combined actuator controller, the ABS test bench of the Control and Mechatronics System Group at the Alpen-Adria University Klagenfurt was utilized.

## Chapter 2

# Vehicle dynamics control systems

The introduction of ABS and ESC has decreased the amount and the severity of vehicle accidents (see Chapter 1). To continue this trend and to enforce the implementation of vehicle dynamic control systems, the European Union and the United States have changed their laws (e.g. [Tod11, Nat07]). Since 2011, the utilization of vehicle control systems has been mandatory for every new homologated vehicle. In order to provide a clearer understanding of the operating principle behind vehicle dynamics control systems, this chapter explains their configuration and functionality.

### 2.1 Antilock braking system - ABS

The antilock braking system controls the motion of a single wheel. By applying a wheel torque  $T_{\text{whl}}$ , which results from a brake pressure  $p_{\text{brk}}$ , a wheel slip  $\lambda$  arises. This wheel slip is calculated

$$\lambda = \begin{cases} \frac{v_{\text{whl}} - v}{v_{\text{whl}}} & \text{while acceleration} \\ \frac{v_{\text{whl}} - v}{v} & \text{while deceleration} \end{cases}, \quad (2.1)$$

where  $v_{\text{whl}}$  is the wheel velocity and  $v$  is the vehicle velocity. As can be seen from Figure 2.1, the resulting longitudinal tire force  $F_x$  is a function of the wheel slip  $\lambda$ . For low absolute values of  $\lambda$ , the longitudinal tire force is proportional to  $\lambda$ . This region of operation is called *stable tire force region*. If a critical slip  $\lambda_c$  is exceeded, the absolute value for the tire force decreases, although the slip value increases. This region is the *unstable tire force region*. If the wheel slip  $\lambda$  exceeds  $\lambda_c$ , the wheel tends to lock if no brake torque reduction occurs.

Usually, the wheel torque is controlled with the brake pressure. If the intended torque (i.e. the intended brake pressure) results in a high wheel slip, the wheel tends to lock, and the “wheel stability” is lost. In order to achieve the best braking performance, the wheel slip  $\lambda$  should be adjusted such that  $F_x$  is maximized (see Figure 2.1). The maximum tire force typically occurs at

$$|\lambda_c| \approx 0.12. \quad (2.2)$$

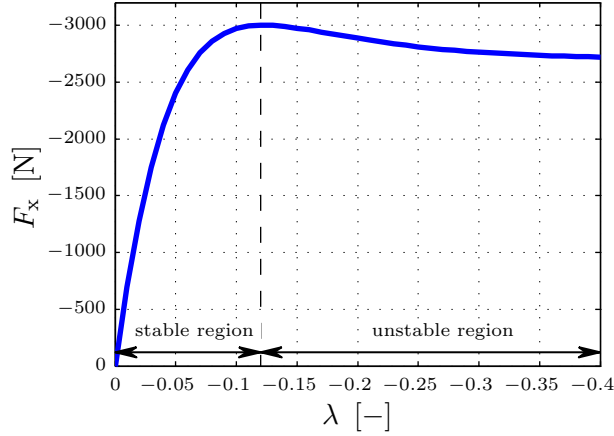


Figure 2.1: Longitudinal tire force characteristic

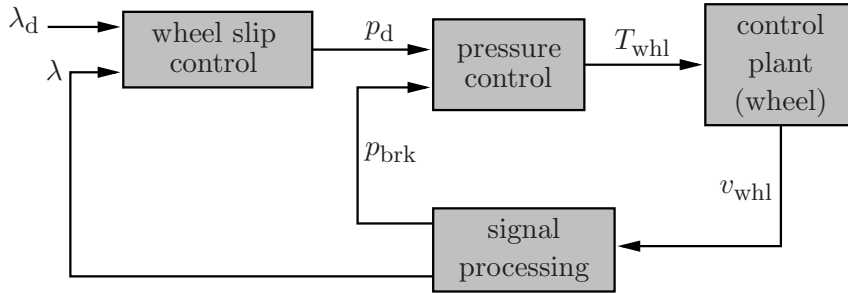


Figure 2.2: ABS control loop [Ise06] (with adaptations by the author)

As the value of  $\lambda_c$  is not known exactly, the ABS uses  $\lambda_d$  as its reference value.  $\lambda_d$  is a rough estimation of  $\lambda_c$  which is either calculated in the ABS or determined by the ESC when an intervention of the yaw motion controller is required. If

$$|\lambda| > |\lambda_d| \tag{2.3}$$

the ABS must reduce the brake torque such that  $\lambda$  matches the desired wheel slip  $\lambda_d$ . This requires a control loop, as shown in Figure 2.2. The brake pressure  $p_{brk}$  results in a wheel torque  $T_{whl}$ , which decelerates the wheel to the wheel velocity  $v_{whl}$ . From the wheel velocity  $v_{whl}$ , the wheel slip  $\lambda$  and the current brake pressure  $p_{brk}$  can be calculated. This is done in a signal processing unit utilizing mathematical models of the brake system and the wheel motion. By comparing  $\lambda$  to the desired wheel slip  $\lambda_d$ , a desired brake pressure  $p_d$  is calculated, which is used to adapt  $T_{whl}$  such that  $\lambda$  equals  $\lambda_d$ .

Kiencke divides the wheel slip control sequence into seven phases, as seen in Figure 2.3 [KN00].

**Phase 1:** The driver increases the brake pressure  $p_{brk}$  to decelerate the vehicle. The wheel torque  $T_{whl}$  causes the wheel deceleration  $\dot{v}_{whl}$ .

**Phase 2:** If the wheel deceleration exceeds the threshold  $a_1$ , the brake pressure  $p_{brk}$  is

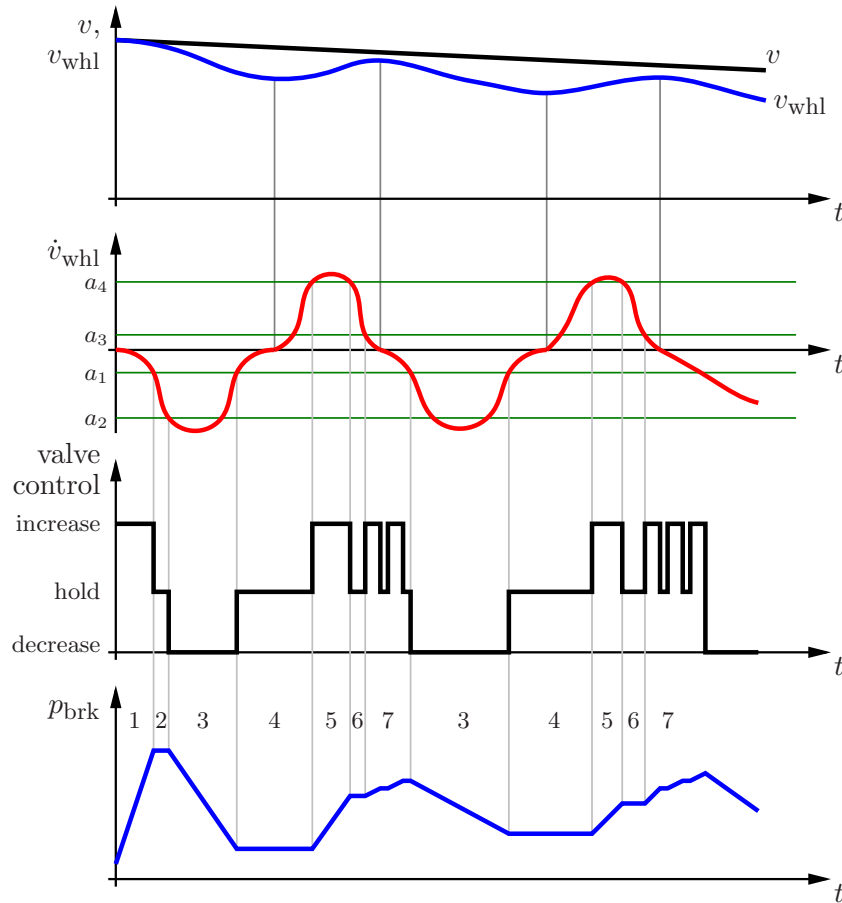


Figure 2.3: Typical ABS control cycle [KN00]

held constant until the wheel deceleration exceeds the second threshold  $a_2$ .

**Phase 3:** In phase 3, the brake pressure is continuously reduced, until the wheel acceleration threshold  $a_1$  is achieved.

**Phase 4:** When the wheel acceleration  $\dot{v}_{\text{whl}}$  is lower than threshold  $a_4$ , the brake pressure is again kept constant.

**Phase 5:** If threshold  $a_4$  is exceeded, the pressure is increased, until the acceleration falls below  $a_4$ .

**Phase 6:** The brake pressure remains constant until the wheel acceleration is reduced to threshold  $a_3$ .

**Phase 7:** As long as the deceleration is higher than threshold  $a_1$ , the brake pressure is slowly increased within equidistant time instances, followed by a short period of constant pressure. When the wheel deceleration exceeds threshold  $a_1$ , the sequence restarts with phase 3. The control sequence operates in a loop until the vehicle stops or the brake pressure is low enough to bring the tire back into the stable region.

Figure 2.4 shows the brake torque control in a real-world vehicle. Figure 2.6 shows the brake pressures and the wheel velocities in the event that a braking maneuver is initiated at split- $\mu$  (see Figure 2.5), where the traction force potentials between the left

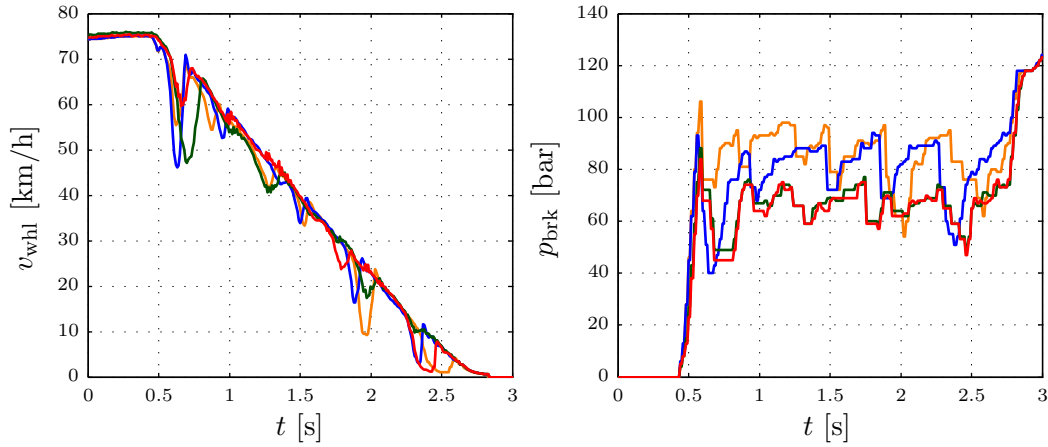


Figure 2.4: Typical ABS cycle for high- $\mu$  braking

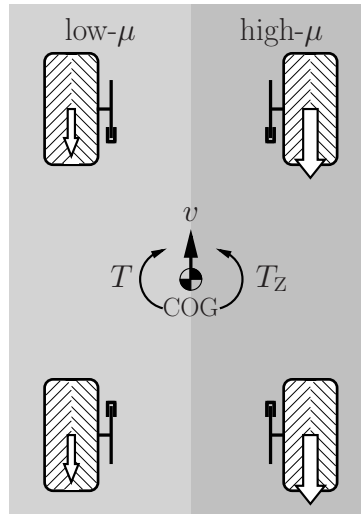
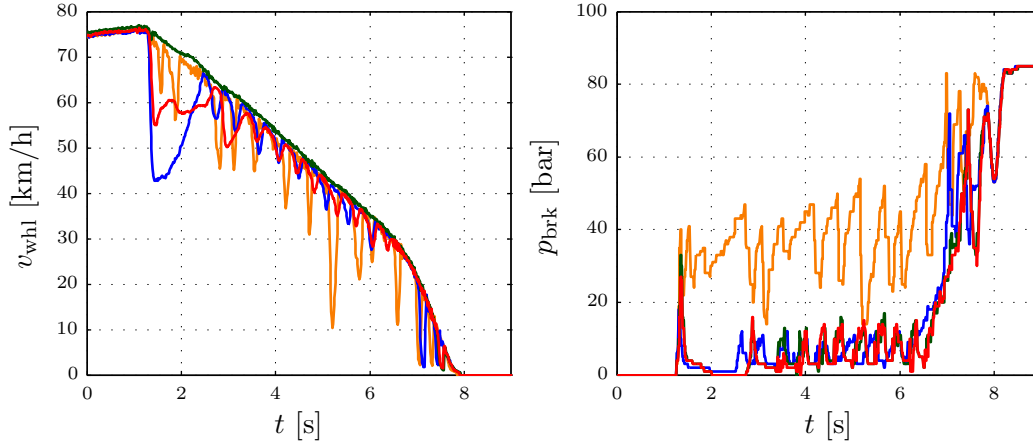


Figure 2.5: Vehicle motion and traction force potential on  $\mu$ -split conditions

and right sides of the vehicle differ significantly. The maximum tire force on the low- $\mu$  side is achieved by a lower brake pressure than that applied on the high- $\mu$  side. Therefore it follows that the tires on the high- $\mu$  side generate a higher tire force than the low- $\mu$  side tires. This introduces a yaw torque  $T$  into the vehicle, which causes the vehicle to spin around its center of gravity (COG). As the ABS is only able to control the wheel motion, an additional control system is needed to counteract this unintended yawing motion, which is called ESC.

In the case of vehicle acceleration, the wheel may begin to spin if the propulsion torque is too high. This situation also results in a loss of “wheel stability”. Beyond controlling the brake pressure, this situation requires an adaptation of the vehicle propulsion torque. The control system that ensures a low wheel slip during acceleration is called Acceleration Slip Control (ASC).

Figure 2.6: Typical ABS cycle for split- $\mu$  braking

## 2.2 Electronic stability control system - ESC

The ESC system focuses on the yaw motion control of the vehicle. If the yaw motion does not match the driver's intention (e.g. due to varying road surface conditions), an additional correction torque  $T_z$  (see Figure 2.5) must be applied. Typically, drivers are not familiar with such situations, as they do not appear very often. This unfamiliarity leads them to conduct excessive corrective steering maneuvers, which make the situation even worse by exceeding physical limits. The assistance of a control system is needed to support the driver. This is usually achieved via single-wheel brake interventions, which are triggered by the ESC. Figure 2.7 shows the resulting vehicle motion using two simple examples that might occur for any driver. The starting point is a cornering maneuver, during which the vehicle should follow the road. This requires appropriate steering from the driver. However, Figure 2.7a shows a case in which the vehicle is unable to follow the desired path due to understeering behavior. Applying a short brake intervention on the rear left wheel induces a yaw torque  $T_z$  that forces the vehicle to stay on track. In the case of oversteering, the vehicle tends to skid (see Figure 2.7b), as the vehicle's yaw motion is faster than what the driver desires. In such cases, a correction torque introduced at the front right wheel can prevent this skidding.

The ESC coordinates the required brake interventions, while the ABS executes them. The ABS is therefore a subordinate control system of the ESC. Figure 2.8 shows a common structure of the resulting control loop. As can be seen from Figure 2.8, the sensor signals from the steering input  $\delta$ , the yaw rate  $\dot{\psi}$ , the lateral acceleration  $a_y$  and the wheel speed  $v_{\text{whl}}$  are used to estimate the vehicle sideslip angle  $\beta$  and the vehicle velocity  $v$ . With the help of a vehicle model, the desired yaw rate  $\dot{\psi}_d$  is calculated. The yaw rate error  $\tilde{\psi}$  is also used for the driving state recognition and the yaw rate controller. Depending on the driving state, either the yaw rate controller or the sideslip angle limitation is activated. Their outputs  $T_{z,\psi}$  and  $T_{z,\beta}$  are needed to calculate the intended wheel slip  $\lambda_d$  for each wheel. To achieve  $\lambda_d$ , the brake pressure  $p_{\text{brk}}$  is applied to the wheels.

State-of-the-art vehicles are equipped with other chassis and drivetrain control systems that can also be used to maintain vehicle stability. For example [Bün98] introduced the

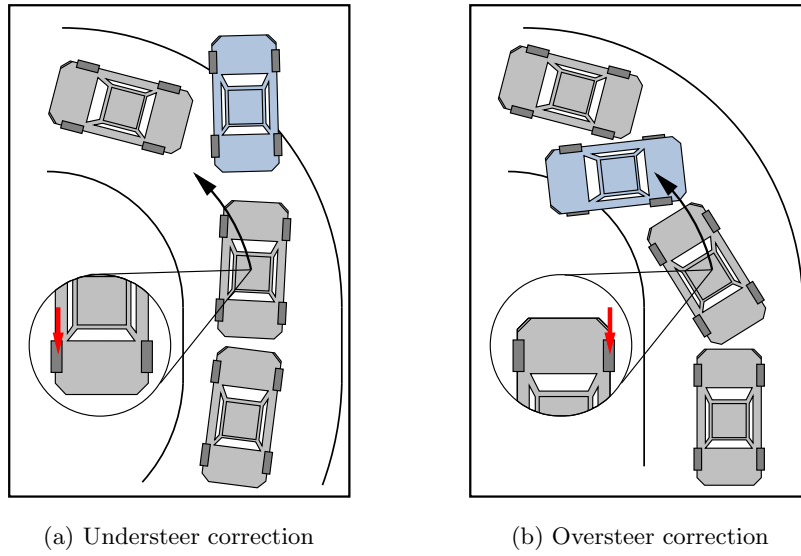


Figure 2.7: Yaw motion control interventions [Ant08]

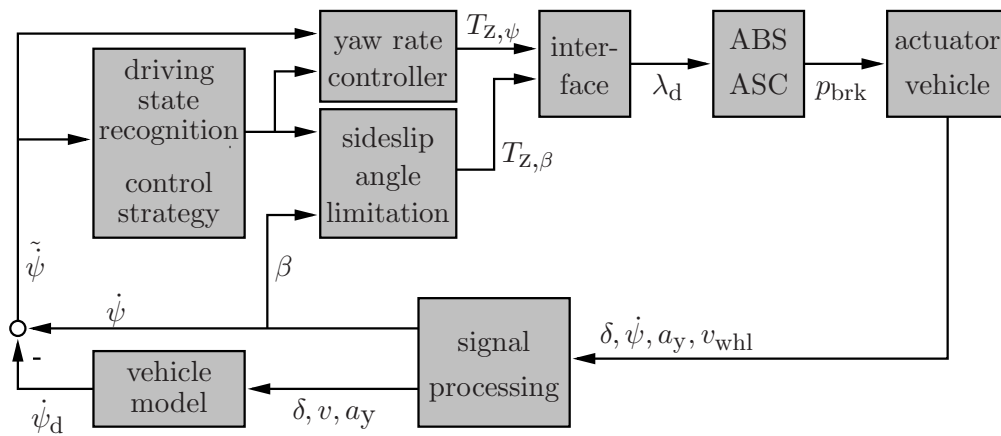


Figure 2.8: ESC control loop [Rau07] (with adaptations by the author)

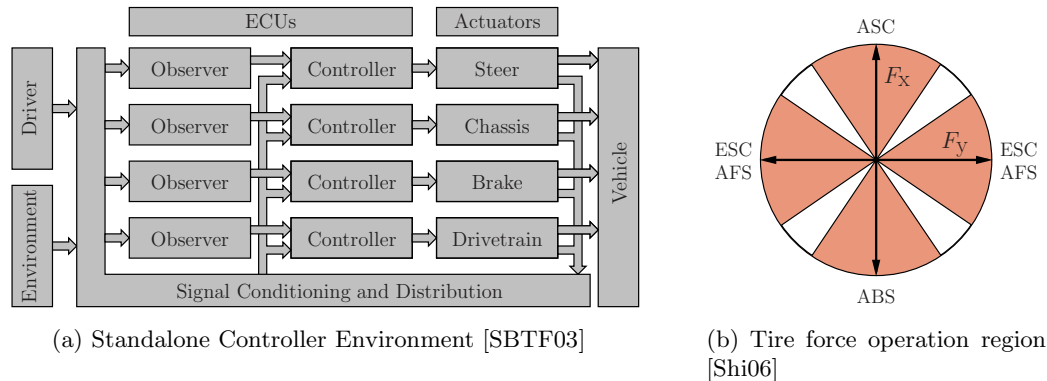


Figure 2.9: Parallel vehicle control system structure

vehicle stability control with AFS support, which adds an additional steering input to that of the driver. Some sports cars are also equipped with active differentials, which are also referred to as torque vectoring differentials [Bic04]. Instead of using brake interventions to apply deceleration torque to the wheel, a yaw torque is generated by accelerating some of the remaining wheels (see Chapter 7 for detailed information about this so-called torque vectoring method). The vehicle yaw motion is considered positive, if the vehicle turns counterclockwise [Deu94].

## 2.3 Control system architecture

### 2.3.1 State-of-the-art electronic stability control system architecture

As the number of control systems in the vehicle increases, the complexity of coordinating these systems increases as well [Trä05]. Typically, the control system topology features a parallel structure, as shown in Figure 2.9a.

The different control systems operate in harmony, whereby each system attempts to establish its set-point (e.g. a reference wheel slip, a target steering angle). The goal of these systems is to generate the tire force needed to achieve the required correction torque  $T_z$ . Figure 2.9b uses *Kamm's circle* to provide some examples of the regions of operation of some common control systems [Shi06, Web05]. ABS and ASC mainly influence the longitudinal force  $F_x$ , while ESC impacts the  $F_x$  and the lateral tire force  $F_y$ . Active steering systems (e.g. AFS) basically influence  $F_y$ . Since the control regions may interfere with one another, the **maximum** potential of every actuator cannot be exploited to stay within the maximum possible tire force region. In particular, this effect is likely to occur when the control algorithms are distributed to different Electronic Control Units (ECUs). Exceeding *Kamm's circle* due to uncoordinated control results in a skidding wheel, which can also be safety-critical. To avoid such situations, safety gaps need to be introduced for actuator operation. In cases where an overlap of the regions of operation may occur, an inferior system performance is probable. In addition, data inconsistency due to calculations in parallel are highly probable. For example when observers calculate the same signal. As long as the vehicle is in an uncritical driving situation, this “coexistence approach” works well. Minor degradations of vehicle motion control rarely occur

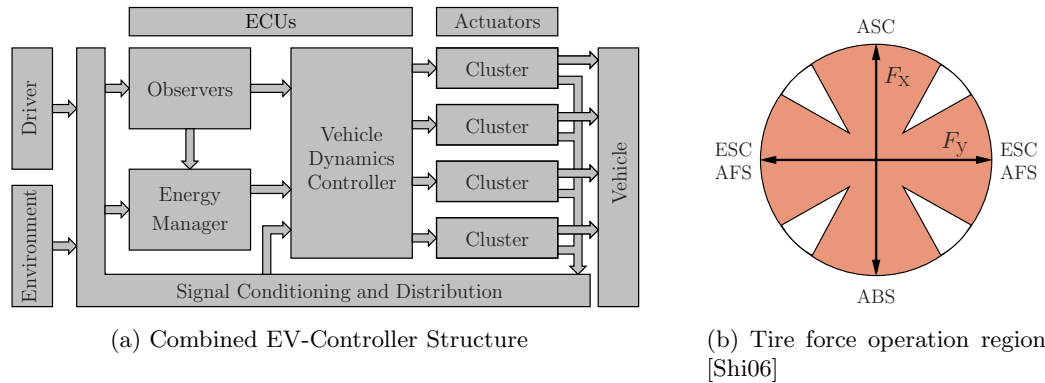


Figure 2.10: Combined vehicle control system structure

and are often not recognizable for the passengers. However, in critical driving situations this behavior is unacceptable, so a strict coordination of the control systems is required. Hence, the maximum available performance is reduced in order to decrease the probability of unforeseeable negative control system interference.

As an example, in the case of an EV application, such a prioritisation might be implemented as follows. An EM algorithm coordinates the propulsion torques in order to provide maximum energy efficiency. When the vehicle starts to decelerate, the traction machine is usually employed to recuperate kinetic energy. As long as the wheel slip is low, the recuperation performs as intended by the energy management. However, when the recuperation torque exceeds  $\lambda_c$ , the wheel enters skidding (see Figure 2.1). Typically, the EM contains no functionality for adapting the recuperation torque based on the road conditions. Therefore, the ESC takes over and commands the EM to stop recuperation. Now, the situation is the same as in conventional cars. The ABS can adapt the brake pressure to achieve the desired wheel slip, and it is not influenced by the traction machine torques. On the other hand, it has the drawback of not exploiting the dynamics of electric traction drives for wheel slip control. Controlling the wheel slip with the support of single-wheel traction drives, for example, would therefore lead to better braking results (see test bench results in Chapter 6).

### 2.3.2 Electronic stability control system for electric vehicles using single-wheel propulsion

The deficiencies mentioned in Section 2.3.1 can be overcome by redesigning the control system topology. One possible approach (shown in Figure 2.10a) is especially well-suited to both the new vehicle topologies and EV applications, where the intention is to introduce smart actuators. Instead of installing the actuator control systems in a parallel structure, they are grouped in actuator clusters. These clusters may consist of several actuators, such as single-wheel steering, traction machine, spring adjustment system or a friction braking system [Jon09]. For all further investigations, it is assumed here that the clusters consist of a single-wheel traction machine and an electronically actuated friction brake. Figure 2.11 shows the schematical structure and an initial prototype of this assembly,

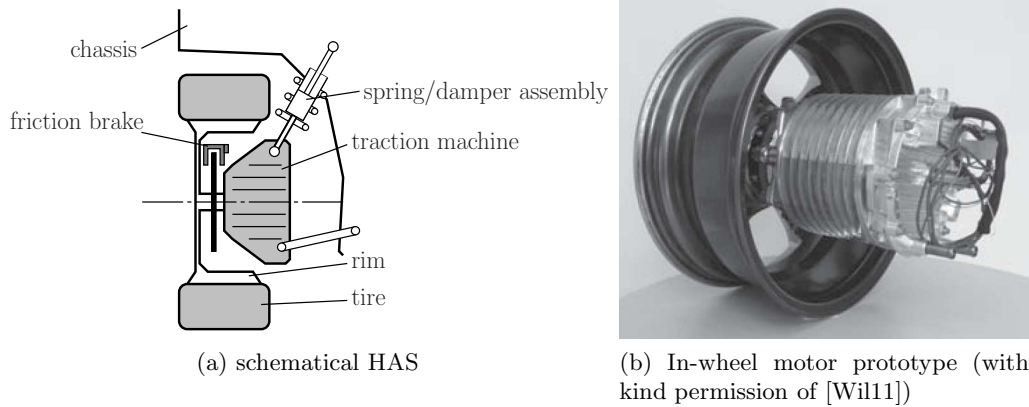


Figure 2.11: Hybrid actuator system

which is referred to as Hybrid Actuator System (HAS).

The information required to control the cluster actuators can be received from sensors or can be estimated by observers. Instead of installing spatially distributed observers, the information is collected by an observer module, whereby the information interchange can be more easily maintained. Information prepared by the observer module is forwarded to the EM and the VDC. In the case of uncritical driving situations, the HAS actuators are only coordinated by the EM, in order to improve energy efficiency and ride comfort. The traction machine is deployed in most cases, whereas the lossy friction brake is only applied when required. The VDC monitors the control signal flow, but no interventions are triggered. However, in critical driving situations (e.g. as outlined in Section 2.2), the control signal flow changes. During this phase, the EM still determines feed-forward control values for the smart actuators, but they are then adapted by the VDC. Instead of completely shutting down recuperation (as in the parallel structure, for example), the EM target values can be used to coordinate the actuators such that energy efficiency and vehicle safety are achieved (see Chapter 5). Since the reference values are now influenced by *one* controller, a coordinated collaboration of all participating actuator systems can be achieved. Each actuator contributes in a way that increases the overall performance and minimizes safety gaps. Overlaps in the actuator operation regions can be avoided (see Figure 2.10b).

Figure 2.12 shows the vehicle topologies considered in this thesis. Figure 2.12a provides a schematic depiction of the actuator configuration in which EV does not employ the electric traction drives during critical driving situations. Only the friction brakes are used for wheel and vehicle motion control, and the system behaves like a conventional vehicle during critical driving situations. In contrast Figure 2.12b shows the EV with an HAS on the rear axle, which is the topology on which this thesis focuses, whereby a wheel slip controller and a yaw motion controller are developed. The friction brake control on the front axle remains the same for both vehicles, and only the controls for the rear axle actuators differ.

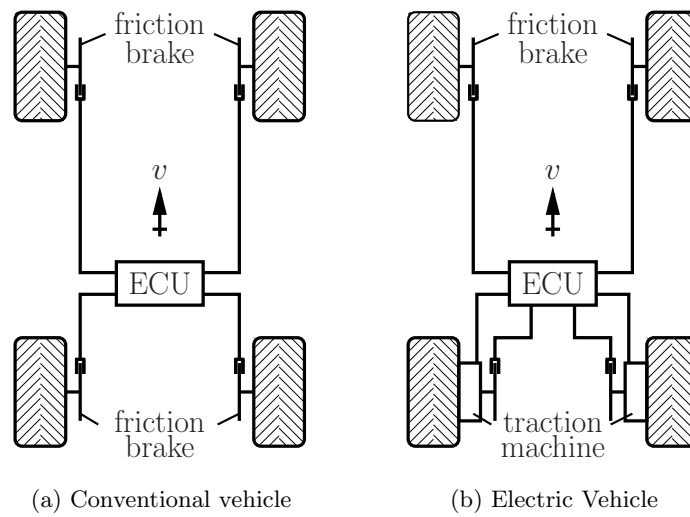


Figure 2.12: Chassis /Drivetrain topology

Chapter 5 offers a detailed explanation of one possible approach to combined actuator control. This structure is then adopted and investigated in detail to create an actuator controller design and a vehicle yaw motion controller design.

## Chapter 3

# Tire models and vehicle models

### 3.1 Tire force characteristics

Tires are the interfaces between the vehicle and the road. They are used for transferring forces back and forth between the vehicle and the road in order to influence the vehicle motion. Tire forces, which can be divided into longitudinal and lateral forces, depend on various parameters, such as load force and road surface friction.

Figure 3.1 shows that the tire force can be separated into the longitudinal tire force  $F_x$  and the lateral tire force  $F_y$ . The tire force generated depends on several parameters, such as rubber compound, road conditions and wearing effects. If the vertical load force  $F_z$  is constant, the tire forces generally look as shown in Figure 3.2. This figure shows that a tire force can only be generated if a wheel slip  $\lambda$  or a wheel sideslip angle  $\alpha$  is present. Based on Figure 3.2, the tire force can be linearized for low values of  $\lambda$  and  $\alpha$ . They can be approximated by

$$F_x = c_\lambda \lambda, \quad (3.1)$$

$$F_y = c_\alpha \alpha \quad (3.2)$$

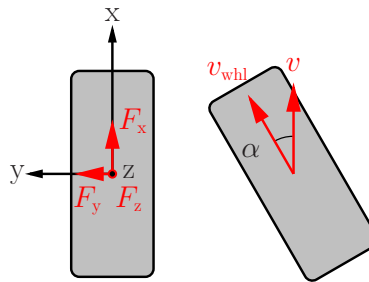
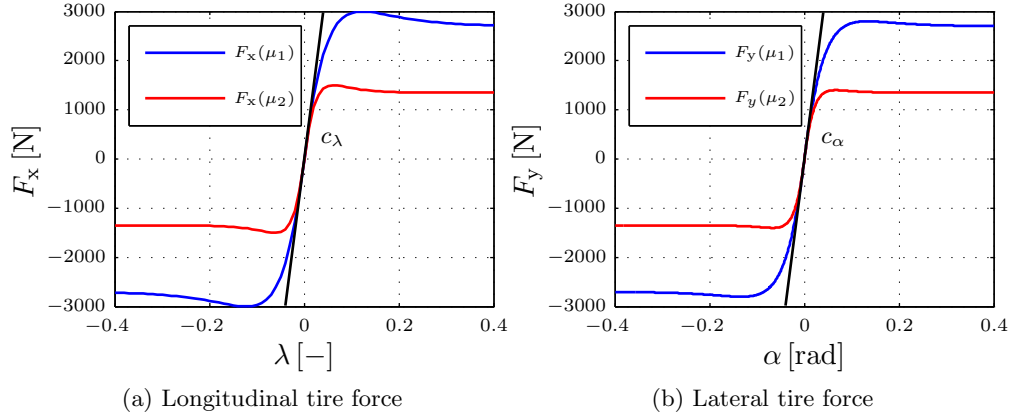


Figure 3.1: Wheel coordinate system and tire forces

Figure 3.2: Longitudinal/lateral tire forces for different road friction coefficients  $\mu$ 

where

$$\lambda = \begin{cases} \frac{\omega r - v}{\omega r} & \text{while acceleration} \\ \frac{\omega r - v}{v} & \text{while deceleration} \end{cases} \quad (3.3)$$

and

$$\alpha_F = \delta - \arctan\left(\frac{l_F \dot{\psi} + v \sin \beta}{v \cos \beta}\right), \quad (3.4)$$

$$\alpha_R = \arctan\left(\frac{l_R \dot{\psi} - v \sin \beta}{v \cos \beta}\right). \quad (3.5)$$

In the equations above,  $c_\lambda$  and  $c_\alpha$  denote the tire stiffness based on the wheel slip  $\lambda$  and the wheel sideslip angles  $\alpha_F$  for the front wheels and  $\alpha_R$  for the rear wheels. The rotational wheel speed is denoted  $\omega$ , while  $v$  is the vehicle speed and  $r$  is the tire radius. As displayed in Figure 3.7,  $l_F$  and  $l_R$  denote the front axle distance and the rear axle distance to the center of gravity. In addition, the yaw rate is denoted by  $\dot{\psi}$ , the vehicle sideslip angle by  $\beta$ , and  $\delta$  is the steering angle.

Instead of describing the wheel slip  $\lambda$  with the wheel velocity  $v_{\text{whl}}$ , it is common to use the angular wheel velocity  $\omega$ , which results from

$$\omega = \frac{v_{\text{whl}}}{r}. \quad (3.6)$$

If the linear region is left, the tire force can be approximated as experienced in [Hir07]. Using the representation according to the *TMsimple* tire model, the longitudinal tire force results in

$$F_x = F_{\max,x}(\mu) \sin\left(B(\mu) \left(1 - e^{-\frac{|\lambda|}{A(\mu)}}\right) \text{sgn}(\lambda)\right) \quad (3.7)$$

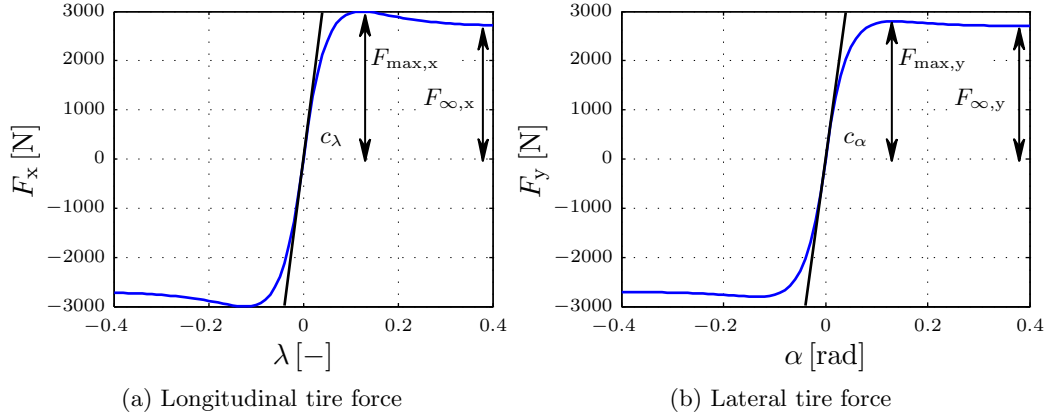


Figure 3.3: TM simple tire forces parameters

where

$$A(\mu) = \frac{F_{\max,x}(\mu) B(\mu)}{c_\lambda}, \quad (3.8)$$

$$B(\mu) = \pi - \arcsin\left(\frac{F_{\infty,x}(\mu)}{F_{\max,x}(\mu)}\right) \quad (3.9)$$

and

$$\text{sgn}(\lambda) = \begin{cases} +1, & \text{if } \lambda > 0, \\ 0, & \text{if } \lambda = 0, \\ -1, & \text{if } \lambda < 0. \end{cases} \quad (3.10)$$

Figure 3.3 shows the required parameters  $F_{\max,x}$ ,  $F_{\infty,x}$  and  $c_\lambda$ .

The same representation holds for the lateral tire force  $F_y$ , if the following terms are replaced within Equations (3.7)-(3.10):

$$F_x \leftrightarrow F_y, F_{\max,x} \leftrightarrow F_{\max,y}, F_{\infty,x} \leftrightarrow F_{\infty,y}, \lambda \leftrightarrow \alpha, c_\lambda \leftrightarrow c_\alpha \quad (3.11)$$

Figure 3.2 demonstrates that the tire forces change when the road friction surface coefficient changes. The same effect occurs if the wheel load force  $F_z$  varies. This degressive characteristic can be implemented by using a polynomial approach. The values for  $c_\lambda$ ,  $c_\alpha$ ,  $F_{\max,x}$ ,  $F_{\max,y}$ ,  $F_{\infty,x}$  and  $F_{\infty,y}$  for nominal load  $F_{z,N}$  and for  $2F_{z,N}$  are required. The corresponding parameters for the longitudinal force calculation can then be determined as

$$F_{\max,x} = a_1 \frac{F_z}{F_{z,N}} + a_2 \left(\frac{F_z}{F_{z,N}}\right)^2, \quad (3.12)$$

$$c_\lambda = b_1 \frac{F_z}{F_{z,N}} + b_2 \left(\frac{F_z}{F_{z,N}}\right)^2, \quad (3.13)$$

$$F_{\infty,x} = c_1 \frac{F_z}{F_{z,N}} + c_2 \left(\frac{F_z}{F_{z,N}}\right)^2 \quad (3.14)$$

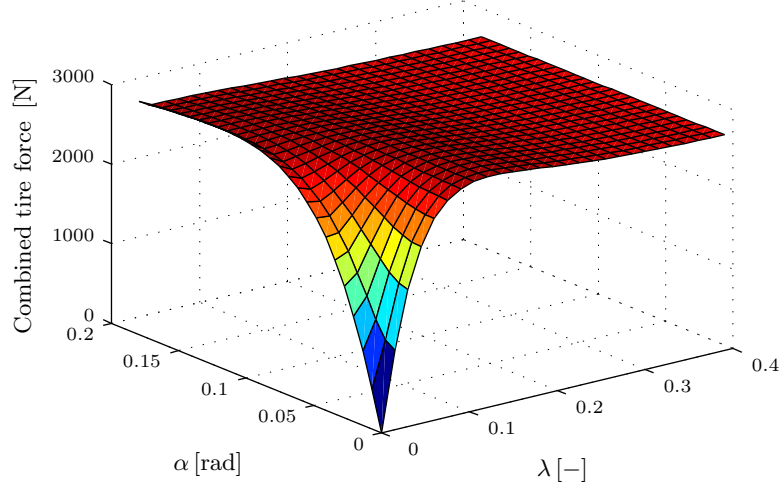


Figure 3.4: Combined TM simple tire forces

where

$$a_1 = 2 F_x(F_{z,N}) - \frac{F_x(2 F_{z,N})}{2}, \quad (3.15)$$

$$a_2 = \frac{F_x(2 F_{z,N})}{2} - F_x(F_{z,N}), \quad (3.16)$$

$$b_1 = 2 c_\lambda(F_{z,N}) - \frac{c_\lambda(2 F_{z,N})}{2}, \quad (3.17)$$

$$b_2 = \frac{c_\lambda(2 F_{z,N})}{2} - c_\lambda(F_{z,N}), \quad (3.18)$$

$$c_1 = 2 F_\infty(F_{z,N}) - \frac{F_\infty(2 F_{z,N})}{2}, \quad (3.19)$$

$$c_2 = \frac{F_\infty(2 F_{z,N})}{2} - F_\infty(F_{z,N}). \quad (3.20)$$

Equations (3.12)-(3.20) are applicable for the lateral tire force  $F_y$  as well if replacement values (3.11) are applied. Both a new set  $\{a_1, a_2, b_1, b_2, c_1, c_2\}$  and  $F_{\max,y}$ ,  $c_\alpha$  and  $F_{\infty,x}$  for calculating  $F_y$  arise.

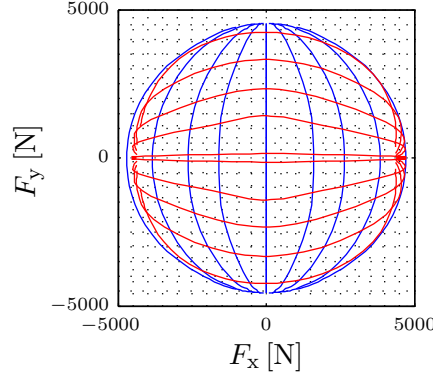
All of the tire-force-related equations stated above are only valid if either longitudinal or lateral tire forces occur. Simultaneous occurrence of longitudinal and lateral forces affect the tire forces, as shown in Figure 3.4. They can be calculated using Equations (3.21)-(3.24)

$$\tan(\kappa) = \frac{A_x B_y F_{\max,x} \alpha}{A_y B_x F_{\max,y} \lambda}, \quad (3.21)$$

$$F = \frac{1}{2} (F_x + F_y + (F_x - F_y) \cos(\kappa)), \quad (3.22)$$

$$F_x(\lambda, \alpha) = F \cos(\kappa), \quad (3.23)$$

$$F_y(\lambda, \alpha) = F \sin(\kappa), \quad (3.24)$$

Figure 3.5: *Kamm's circle*

where  $A_x, B_x$  and  $F_{\max,x}$  correspond to the longitudinal tire force and  $A_y, B_y$  and  $F_{\max,y}$  correspond to the lateral tire force.  $A_x, B_x, A_y$  and  $B_y$  are calculated using Equations (3.8) and (3.9). Maximum available combined tire forces are limited due to *Kamm's circle*, as shown in Figure 3.5.

### 3.2 Tire force approximation for wheel slip controller design

From the relations described in Section 3.1, it is clear that  $F_{\max}$  varies based on the road surface friction coefficient  $\mu$  and the load force  $F_z$ . These relations can be used to generate a simulation model. However, controller design requires, a simpler representation. In most cases, the tires are operated within the region (see Figure 2.1), where the condition

$$\frac{\partial F_x}{\partial \lambda} > 0 \quad (3.25)$$

holds. Assuming that the load force  $F_z$  is constant,  $F_x$  can be approximated by

$$F_x(\mu, \lambda) = F_{\max}(\mu = 1) \mu \tanh((p_0 + p_1 \mu + p_2 \mu^2 + p_3 \mu^3) \lambda). \quad (3.26)$$

The coefficients  $p_0 - p_3$  are constant and can be calculated from the relations introduced in Section 3.1. Figure 3.6 shows an example of the original tire forces and the approximated tire forces. The corresponding approximation (3.26) will be used for the wheel slip controller design process.

### 3.3 Tire force approximation for vehicle stability analysis

For the analysis of the lateral stability of a vehicle it requires values for the lateral tire forces. Using the same procedure as in Section 3.2, the lateral forces can be represented as

$$F_y(\mu, \alpha) = F_{\max}(\mu = 1) \mu \tanh((q_0 + q_1 \mu + q_2 \mu^2 + q_3 \mu^3) \alpha), \quad (3.27)$$

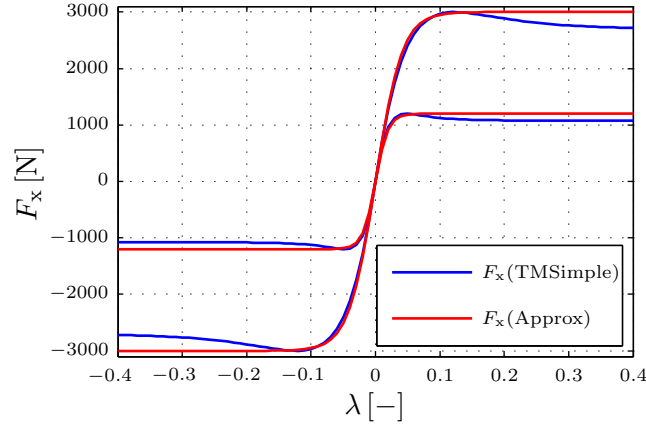


Figure 3.6: Tire force approximation

where  $q_0 - q_3$  are constant coefficients. Since lateral vehicle maneuvers cause a high load shift between the left and right sides of the vehicle, Equation (3.27) has to be extended to

$$F_{y,ij} = F_{\max}(\mu = 1) \mu \tanh((q_0 + q_1 \mu_{ij} + q_2 \mu_{ij}^2 + q_3 \mu_{ij}^3) \alpha_{ij}) \frac{F_{z,ij}}{F_{z,N}} \quad (3.28)$$

$$\forall \begin{cases} i \in \{F, R\} \\ j \in \{L, R\} \end{cases}$$

where

$$F_{z,FL} = \frac{m g}{2} \frac{l_F}{l_F + l_R} - \frac{m a_y}{2} \frac{h_{\text{COG}}}{l_T}, \quad (3.29)$$

$$F_{z,FR} = \frac{m g}{2} \frac{l_F}{l_F + l_R} + \frac{m a_y}{2} \frac{h_{\text{COG}}}{l_T}, \quad (3.30)$$

$$F_{z,RL} = \frac{m g}{2} \frac{l_R}{l_F + l_R} - \frac{m a_y}{2} \frac{h_{\text{COG}}}{l_T}, \quad (3.31)$$

$$F_{z,RR} = \frac{m g}{2} \frac{l_R}{l_F + l_R} + \frac{m a_y}{2} \frac{h_{\text{COG}}}{l_T}. \quad (3.32)$$

In this representation,  $m$  denotes the vehicle mass,  $h_{\text{COG}}$  is the distance between the center of gravity and the road surface and  $l_T$  is the vehicles track width.  $a_y$  is the lateral acceleration, and  $g$  is the gravitational acceleration. This extension also assumes that the vehicle velocity  $v$  is constant, so the load shift based on the longitudinal acceleration  $a_x$  is not considered. In addition, these relations are only valid for static conditions, and dynamics within the load shift are not considered. Consideration of the dynamic load shift requires a roll model, such as the one described in [MW04]. Figure 3.7 provides a view of where forces act and the geometrical relations involved.

### 3.4 Wheel motion model

Figure 3.8 shows the most basic model for describing the longitudinal motion of a vehicle and a wheel. It assumes that a tire load mass  $m_{\text{whl}}$  is acting on one wheel. For reasons

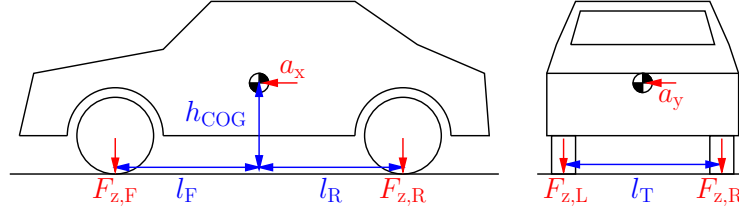


Figure 3.7: Vehicle geometries

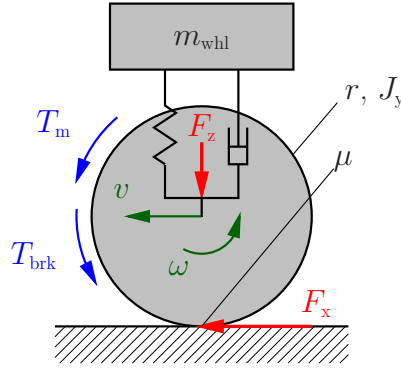


Figure 3.8: Wheel motion model

of simplicity, it is further assumed that the spring-damper assembly in Figure 3.8 can be excluded and the vertical tire stiffness is very high. Applying the principle of angular momentum yields

$$(J_y + J_{\text{veh}}) \dot{\omega} = T_m + T_{\text{brk}} - F_x r. \quad (3.33)$$

In this equation,  $J_y$  is the moment of inertia of the wheel, and  $J_{\text{veh}}$  is the moment of inertia caused from the wheel mass  $m_{\text{whl}}$ . It can be calculated as

$$J_{\text{veh}} = r^2 m_{\text{whl}}. \quad (3.34)$$

The angular wheel acceleration is denoted by  $\dot{\omega}$ , and  $F_x$  is the longitudinal wheel force (see Section 3.1). The propulsion torques  $T_m$  and  $T_{\text{brk}}$  are produced by the traction drive and the friction brake (see Chapter 4). During braking, the wheel slip  $\lambda$  is defined as in Equation (3.3). For controlling  $\lambda$ , it is necessary to compute its time-derivative  $\dot{\lambda}$ . Assuming that the vehicle velocity remains constant for a very short period of time (e.g. the cycle time of the control algorithm), the time derivative of  $\lambda$  as defined in Equation (3.3) yields

$$\dot{\lambda} = \frac{(\dot{\omega} r - \dot{v}) v}{v^2} - \frac{(\omega r - v) \dot{v}}{v^2} \stackrel{\dot{v}=0}{\Rightarrow} \dot{\omega} = \frac{\dot{\lambda} v}{r} \quad (3.35)$$

In the case of a constant load force  $F_z$ , Equation (3.1) can be applied. When considering only the wheel torque  $T_{\text{whl}}$ , it reads as

$$T_{\text{whl}} = T_m + T_{\text{brk}}. \quad (3.36)$$

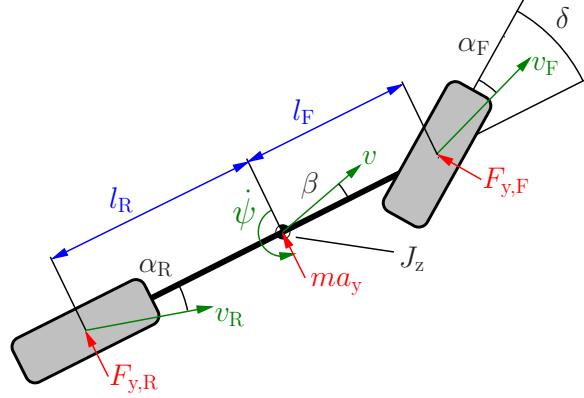


Figure 3.9: Bicycle model

The transfer function  $\mathcal{G}_\lambda(s)$  relating  $\lambda$  and  $T_{\text{whl}}$  can be calculated via (3.1), (3.35), (3.33) and (3.36), that is

$$\mathcal{G}_\lambda(s) = \frac{\mathcal{L}(\lambda)}{\mathcal{L}(T_{\text{whl}})} = \frac{1}{s(J_y + J_{\text{veh}}) \frac{v}{r} + c_\lambda r}. \quad (3.37)$$

$\mathcal{L}(\lambda)$  and  $\mathcal{L}(T_{\text{whl}})$  denote the Laplace-transforms of  $\lambda$  and  $T_{\text{whl}}$ . From (3.37) it can be concluded that the wheel dynamics within the linear tire force range behave like a time-variant first order lag element (PT1 element).

This model is not suitable for investigating lateral vehicle motion, which requires a bicycle model or a two-track model instead.

## 3.5 Lateral vehicle models

### 3.5.1 Linear bicycle model

The description of the yawing motion of a vehicle also requires mathematical models. According to [RS40], the simplest representation for this purpose is the linear bicycle model, which represents the linear vehicle behavior under some special conditions (e.g. constant velocity  $v$ , low lateral acceleration  $a_y$ , dry road conditions at high- $\mu$ ). The bicycle model assumes that the wheels on one axle are combined to one wheel as shown in Figure 3.9. Utilizing the principle of linear and angular momentum, it follows that

$$J_z \ddot{\psi} = F_{y,F} l_F - F_{y,R} l_R, \quad (3.38)$$

$$m a_y = F_{y,F} + F_{y,R} \quad (3.39)$$

where  $J_z$  is the moment of inertia of the vehicle, and  $\ddot{\psi}$  is the yaw acceleration. For a constant vehicle velocity  $v$  and low sideslip angles  $\alpha_F$  and  $\alpha_R$ , a linear tire characteristic based on Equation (3.2) is assumed. The tire forces can be calculated as

$$F_{y,F} = c_{\alpha,F} \alpha_F, \quad (3.40)$$

$$F_{y,R} = c_{\alpha,R} \alpha_R. \quad (3.41)$$

Based on [MW04] and Equations (3.4) and (3.5), the linearized sideslip angles can be calculated for low values as

$$\alpha_F = -\beta + \delta - \frac{l_F}{v} \dot{\psi} \quad (3.42)$$

and

$$\alpha_R = -\beta + \frac{l_R}{v} \dot{\psi}. \quad (3.43)$$

Using this relation, the lateral tire forces result in

$$F_{y,F} = -c_{\alpha,F} \beta + c_{\alpha,F} \delta - \frac{c_{\alpha,F} l_F}{v} \dot{\psi}, \quad (3.44)$$

$$F_{y,R} = -c_{\alpha,R} \beta + \frac{c_{\alpha,R} l_R}{v} \dot{\psi}. \quad (3.45)$$

Bringing lateral motion and yaw motion together [Ise06], it follows that

$$a_y = v \left( \dot{\psi} + \dot{\beta} \right). \quad (3.46)$$

Finally, the Equations (3.39) and (3.38) result in the state space model

$$\begin{bmatrix} \ddot{\psi} \\ \dot{\beta} \end{bmatrix} = \begin{bmatrix} -\frac{c_{\alpha,R} l_R^2 + c_{\alpha,F} l_F^2}{J_z v} & \frac{c_{\alpha,R} l_R - c_{\alpha,F} l_F}{J_z} \\ \frac{c_{\alpha,R} l_R - c_{\alpha,F} l_F}{m v^2} - 1 & -\frac{c_{\alpha,F} + c_{\alpha,R}}{m v} \end{bmatrix} \cdot \begin{bmatrix} \dot{\psi} \\ \beta \end{bmatrix} + \begin{bmatrix} \frac{c_{\alpha,F} l_F}{J_z} \\ \frac{c_{\alpha,F}}{m v} \end{bmatrix} \delta. \quad (3.47)$$

As this model is very simple, it is often used for designing yaw motion controller or for determining the reference values for lateral vehicle motion.

### 3.5.2 Non-linear two-track model

Often, the linear model is extended with nonlinear tire characteristics. In addition, the simplification of grouping the wheels of one axle is no longer applied.

The following statements are based on [Sma00]. In contrast to [Sma00], the tire model presented in Section 3.1 is used here. The starting points are once again Equations (3.38) and (3.39). The lateral tire forces  $F_{y,F}$  and  $F_{y,R}$  of one axle are now calculated from the tire forces  $F_{y,FL}$ ,  $F_{y,FR}$ ,  $F_{y,RL}$  and  $F_{y,RR}$ :

$$F_{y,F} = F_{y,FL} + F_{y,FR}, \quad (3.48)$$

$$F_{y,R} = F_{y,RL} + F_{y,RR}. \quad (3.49)$$

As the vehicle velocity  $v$  is assumed to be constant, the longitudinal tire forces  $F_{x,FL}$ ,  $F_{x,FR}$ ,  $F_{x,RL}$  and  $F_{x,RR}$  can be excluded. Together with (3.46), the differential equations for the state variables  $\psi$  and  $\beta$  read as

$$\ddot{\psi} = \frac{(F_{y,FL} + F_{y,FR}) l_F - (F_{y,RL} + F_{y,RR}) l_R}{J_z}, \quad (3.50)$$

$$\dot{\beta} = \frac{F_{y,FL} + F_{y,FR} + F_{y,RL} + F_{y,RR}}{m v} - \dot{\psi}. \quad (3.51)$$

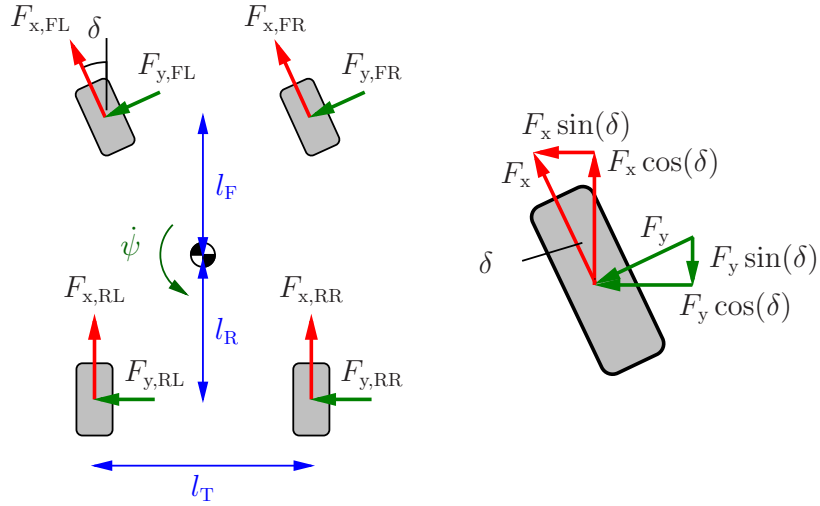


Figure 3.10: Two-track model

When calculating the yawing behavior during braking, the longitudinal tire forces have to be considered. Using the geometrical relations introduced in Figure 3.7 leads to the situation shown in Figure 3.10. The principle of angular momentum yields

$$\begin{aligned}
 J_z \ddot{\psi} &= F_{x,FL} \sin(\delta) l_F - F_{x,FL} \cos(\delta) \frac{l_T}{2} + F_{y,FL} \cos(\delta) l_F + F_{y,FL} \sin(\delta) \frac{l_T}{2} + \\
 &+ F_{x,FR} \sin(\delta) l_F + F_{x,FR} \cos(\delta) \frac{l_T}{2} + F_{y,FR} \cos(\delta) l_F - F_{y,FR} \sin(\delta) \frac{l_T}{2} - \\
 &- F_{y,RL} l_R - F_{x,RL} \frac{l_T}{2} - F_{y,RR} l_R + F_{x,RR} \frac{l_T}{2}.
 \end{aligned} \tag{3.52}$$

The required nonlinear tire forces  $F_{x,FL}$ ,  $F_{y,FL}$ ,  $F_{x,FR}$ ,  $F_{y,FR}$ ,  $F_{x,RL}$ ,  $F_{y,RL}$ ,  $F_{x,RR}$  and  $F_{y,RR}$  can be calculated as outlined in Section 3.1. In contrast to (3.42) and (3.43), the tire forces are now valid for higher  $\alpha$  values as well. Therefore, the linearisation shown in Section 3.1 is not allowed. Assuming that the sideslip angles on both sides are equal, they can be calculated as defined in (3.4) and (3.5).

## Chapter 4

# Drivetrain actuators

As explained in Chapter 2, the vehicle motion control should be performed with a friction brake on the front axle and a hybrid actuator system on the rear axle. The HAS consists of a single-wheel traction machine and a hydraulic friction brake.

### 4.1 Friction brake

Figure 4.1a shows a schematic representation of a state-of-the-art friction brake. The driver depresses the brake pedal and, with the support of a vacuum booster and a piston, originates the pressure  $p_{\text{brk}}$ . This pressure pushes the brake pads against the brake disc and generates a brake torque  $T_{\text{brk}}$ . Figure 4.1b shows common brake pressure characteristic for such brake systems. As there is a direct connection between the brake pedal and the hydraulic circuit, the characteristic cannot be altered during vehicle operation. Depending on the amount of kinetic energy being recuperated, the resulting brake pedal characteristic changes. For the driver, this feels unusual or even uncomfortable. Since energy recuperation is an important feature of EVs/HEVs, their effects must not be noticeable for the driver. Therefore, it must be possible to modify the direct connection between pedal actuation and friction brake torque [DDKAF11]. Figure 4.2a shows one schematical construction that could meet this requirement. Examples of future brake systems are also mentioned in [Pfe11] and [Fei12]. The mechanical connection between pedal and brake pressure (brake torque) can be constructed as shown in Figure 4.2b. Due to a modified pedal travel mechanism, the friction brake can apply a brake pressure only when higher pedal travel values are reached (decoupled characteristic). The resulting gap between the decoupled brake characteristic and the conventional characteristic can be overcome by external brake actuators or by recuperation, for example. If the brake characteristic is completely decoupled from the driver's input, the system is known as a brake-by-wire system [BB07, AS01]. Using energy management algorithms, the ratio between recuperative braking torque and mechanical braking torque can be varied, which is known as *blending*.

For the mechanical brake system, it is necessary to find a relation between the brake pedal input (brake pedal travel) representing the driver's intended deceleration torque, and the resulting wheel braking torque  $T_{\text{brk}}$ . If the brake pedal is actuated very quickly, the brake pressure dynamics are slower than the pedal dynamics. Hence, the brake pedal

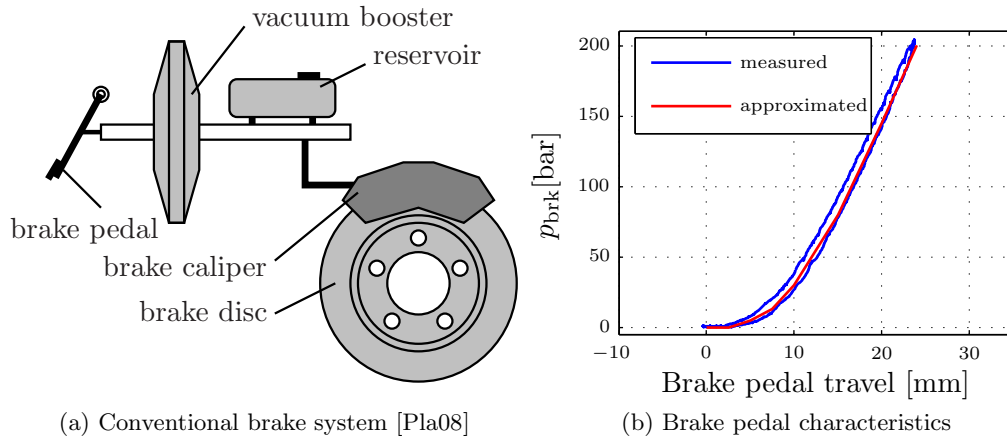


Figure 4.1: Conventional brake system

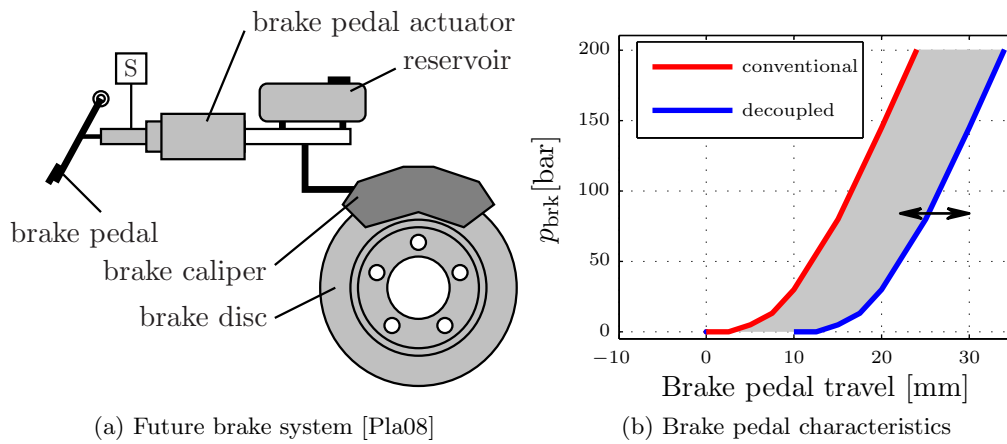


Figure 4.2: HEV/EV brake system

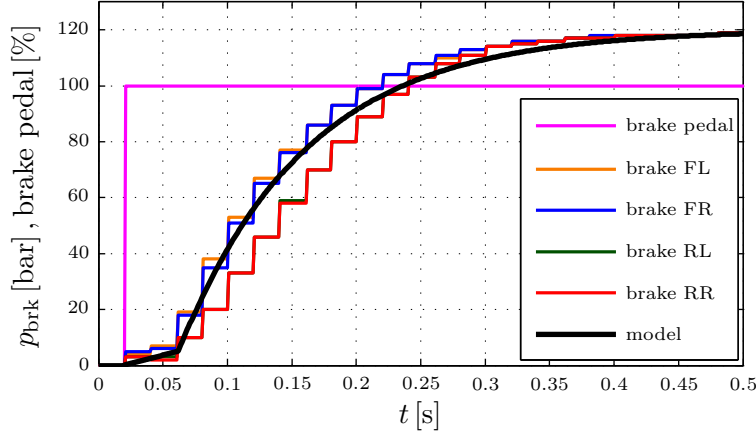


Figure 4.3: Brake system response

input can be regarded as a desired brake pressure  $p_d$ . The pressure  $p_{\text{brk}}$  can usually be measured in a vehicle. Figure 4.3 shows an example of the pressure caused by a brake pedal input. As the brake pedal travel is usually not available, only the boolean signal for brake actuation is shown. When the brake pedal is pressed, the pressure in the front axle brake circuit rises faster than the pressure in the rear brake circuit. This is due to longer brake pipes and due to overcoming venting gaps. When a certain pressure is achieved, the pressure rises with a high slew rate. As stated in [MW04], the relation between brake pressure and its resulting braking torque is mainly constrained by mechanical and geometrical dependencies, which are summarized by the proportional factor  $K_{\text{brk}}$ . As has been confirmed by measurements (see Figure 4.3), the step response of the desired brake pressure  $p_d$  can be regarded as the step response of a PT1 transfer function, if the venting behavior is omitted. This assumption is acceptable for the controller design, as the venting gap only occurs at the beginning of the brake intervention. Once the kisspoint has been overcome, the response shows a PT1 behavior. Hence, the transfer function for the mechanical brake system is given by

$$\mathcal{G}_{\text{brk}}(s) = \frac{\mathcal{L}(T_{\text{brk,p}})}{\mathcal{L}(p_d)} = K_{\text{brk}} \frac{1}{s\tau_b + 1}. \quad (4.1)$$

$\mathcal{L}(T_{\text{brk,p}})$  and  $\mathcal{L}(p_d)$  denote the Laplace-transforms of  $T_{\text{brk,p}}$  and  $p_d$ . As the disc brake torque  $T_{\text{brk,p}}$  is strictly positive, it follows that the brake torque considering the wheel rotation is

$$T_{\text{brk}} = T_{\text{brk,p}} \operatorname{sgn}(-\omega). \quad (4.2)$$

## 4.2 Synchronous machines

### 4.2.1 Classification of synchronous machines

State-of-the-art EVs apply electric traction machines for propulsion. For each vehicle, the drivetrain topology and power class will determine whether it is better to apply a

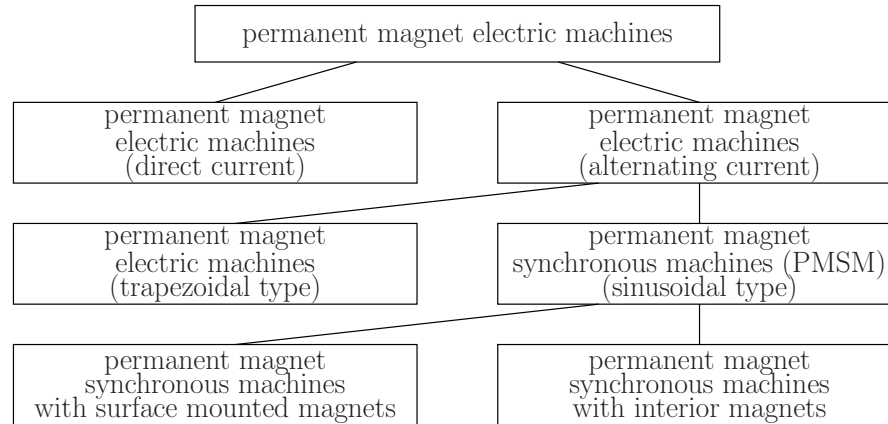


Figure 4.4: Permanent magnet electric machines classification [Cha02]

synchronous or an asynchronous machine (see Figure 1.7). In particular, synchronous machines are becoming increasingly relevant for such applications because they offer:

- good dynamic behavior (low moment of inertia)
- high torque compared to size (the air gap is next to the outer radius)
- robustness (no commutator ring)
- no heating losses within the rotor
- relatively simple cooling

However, aside from all these advantages, there are also the disadvantages of setting-up a drag torque. Therefore, in the automotive industry, they are only applied as permanent drives or in the case of non-permanent operation, if coupled motion can be avoided (e.g. for air conditioning compressor drives). In the discussion of the effects of electric system faults, Chapter 4.2.4 places a special emphasis on the generation of the drag torque. These results are then used in Chapter 8, which investigates their impact on the vehicle dynamics.

According to [Cha02], permanent magnet electric machines can be classified as shown in Figure 4.4. An interesting differentiation of Permanent Magnet Synchronous Machines (PMSMs) is thereby provided by the placement of the magnets. As shown in Figure 4.5, there are machines with surface magnets and machines with buried magnets (interior magnets). For rotors with magnets on the surface, it is essential that they are secured with a fiberglass layer, due to the high centrifugal forces that occur at higher speeds. This disadvantage leads to a lifetime safety topic, which requires separate investigations. Furthermore, such types of machines are also avoided due to their relatively high cost. In contrast, the magnets can also be integrated into the rotor [SE02]. Although this requires high efforts, this configuration offers an interesting benefit. The magnets can be arranged such that the resulting magnetic rotor field is not homogeneous around the rotor's surface. For example, if the magnets are buried (as in Figure 4.5b), their field lines build up local minima and local maxima of magnetic density. As a result, the main inductance  $L_d$  is not equal to the reluctance inductance  $L_q$ , as is the case with the

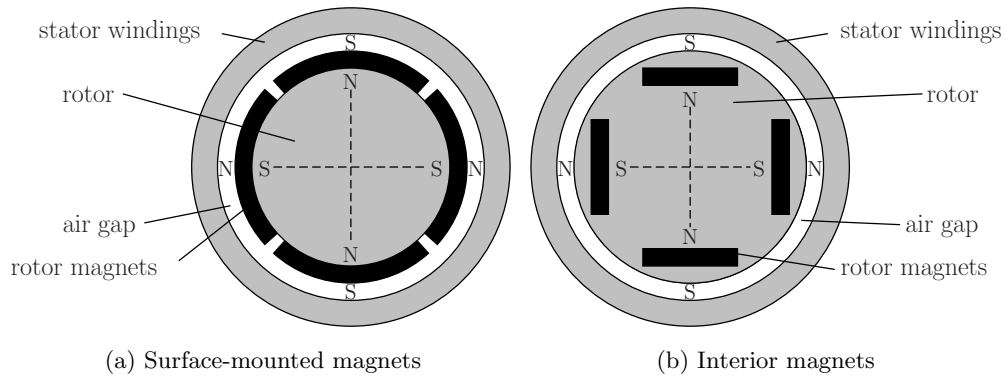


Figure 4.5: PMSM rotor magnet locations [Cha02]

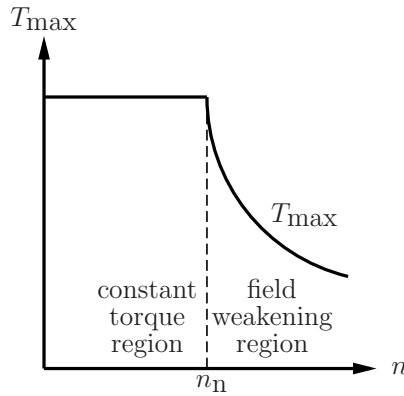


Figure 4.6: PMSM torque characteristic

surface magnets case. As will be shown in Chapter 4.2.3, this circumstance can be used to establish an additional reluctance torque. For the same package size, it is therefore possible to generate a higher amount of torque (due to an increased torque-to-space ratio) than with machines with surface-mounted magnets. For this reason, interior magnet types are preferred. Section 4.2.3 explains how this beneficial torque can be exploited.

Figure 4.6 shows the typical characteristics for motor operation. For generator operation, the maximum available torque  $T_{\max}$  can be mirrored at the abscissa. For all further investigations, it is assumed that a positive machine torque  $T_m$  indicates motor operation, while a negative machine torque represents generator operation.

*Constant torque region:* At low speeds,  $T_{\max}$  is constant. In this region the stator voltage and the stator current can be adapted to generate the desired maximum torque. The machine operates in its “constant torque region” until the rotor speed exceeds the nominal speed  $n_n$ . If the speed increases further, the magnetic field must be weakened, as the maximum voltage has already been reached.

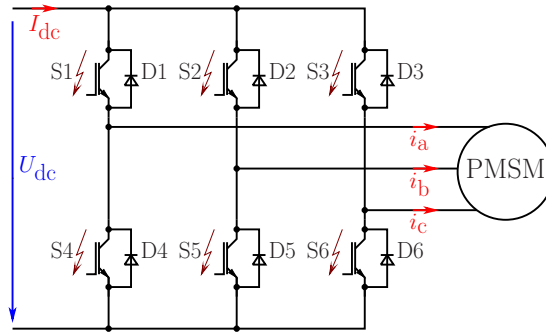


Figure 4.7: B6-Inverter bridge

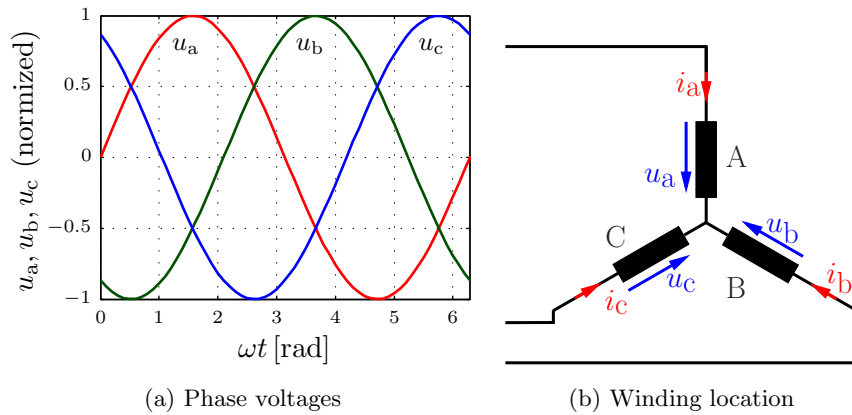


Figure 4.8: Three-phase system

*Field weakening region/constant power region:* The weakening of the magnetic field is required for speeds exceeding the nominal speed  $n_n$ . Otherwise the rotating magnets would generate an excessive induced stator voltage, which would lead to machine damage. In maintaining a sufficiently low magnetic field, the stator field has to counteract the rotor field. A further increase of the stator current is also impossible. As a certain fraction of the stator current is required to weaken the magnetic field, the maximum available torque is reduced. Since voltage and current have to be kept constant, this operating region is also known as the “constant power region”.

To operate a synchronous machine, it is necessary to generate an alternating current net. For a three-phase machine, a B6-Inverter bridge (see Figure 4.7) is typically applied. The six switching elements S1-S6 are controlled such that the DC-link measures (direct current)  $U_{dc}$  and  $I_{dc}$  are transferred into AC measures (alternating current) as shown in Figure 4.8a.

#### 4.2.2 Mathematical representation of a synchronous machine

The space vector representation is used to display a three-phase system. Thereby, it is assumed that only sinusoidal measures occur. The resultant space vector is determined by

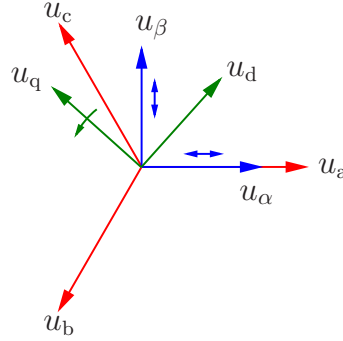


Figure 4.9: Coordinate transformation: a-b-c system  $\leftrightarrow$   $\alpha$ - $\beta$  system  $\leftrightarrow$  d-q system

three stator windings (A, B, C), which are spatially displaced by  $2\pi/3\text{rad}$  (see Figure 4.8b). The three stator phase voltages  $u_a$ ,  $u_b$  and  $u_c$  are usually sinusoidal and time-shifted by  $2\pi/3\text{rad}$  as well (see Figures 4.8a and 4.9). In order to derive a simple mathematical model, which is required for the design of the machine controller and the wheel slip controller, the following assumptions are made:

- the machine has a constant, ideal efficiency of 100%
- all inductances are constant (saturation effects are not taken into account)

For the stator side, the traction drive can be described in the a-b-c coordinate system (stator-fixed system). The schematically shown windings A, B and C consist of an ohmic resistance in serial connection with an inductance. In accordance with Table 3, the representation results in

$$u_i = R_i i_i + \frac{d\Phi_i}{dt} \quad \forall i \in \{a,b,c\} \quad (4.3)$$

where  $R_i$  is the ohmic resistance,  $i_i$  is the phase current, and  $\Phi_i$  is the magnetic flux. This representation consists of AC measures, which are difficult to handle due to their orientation. Therefore, an easier representation is required for the controller design. Transforming system (4.3) from the stator-fixed coordinate system into the rotor-fixed coordinate system (d-q system) facilitates the controller design. The d-q system contains only transient DC measures, as opposed to the AC measures found within the a-b-c system. The transformation can be performed using the *Clarke* transformation (transformation from the a-b-c system into the  $\alpha$ - $\beta$  system) followed by the *Park* transformation (transformation from the  $\alpha$ - $\beta$  system into the d-q system). Figure 4.9 shows an example of both transformations for the phasor diagram. Detailed information about this procedure is available in [VB08]. The mathematical representation within the d-q coordinate system results in

$$u_d = R i_d + L_d \frac{di_d}{dt} - \omega_e L_q i_q, \quad (4.4)$$

$$u_q = R i_q + L_q \frac{di_q}{dt} + \omega_e L_d i_d + \omega_e \Phi, \quad (4.5)$$

$$\omega_e = 2\pi n P, \quad (4.6)$$

where  $P$  is the number of pole pairs, and  $\omega_e$  is the electrical angular velocity. Using these results, the machine torque is calculated as

$$T_i = \frac{3}{2} P \Phi i_q + \frac{3}{2} P (L_d - L_q) i_d i_q. \quad (4.7)$$

Depending on the type of machine (surface-mounted magnets or interior magnets), the relations between  $L_q$  and  $L_d$  change:

$$L_d = L_q \text{ for surface-mounted magnets type} \quad (4.8)$$

$$L_d \neq L_q \text{ for interior magnets type} \quad (4.9)$$

If a surface magnet type is chosen, the second term in Equation (4.7) is eliminated, which is not the case for interior magnet types. Among other reasons, the torque component added by the second term, known as *reluctance torque*, accounts for the common preference for interior magnet types.

Due to the orientation of the coordinates within the d-q system, it follows that

$$u = \sqrt{u_d^2 + u_q^2} \quad (4.10)$$

and

$$i = \sqrt{i_d^2 + i_q^2}. \quad (4.11)$$

$u$  is the amplitude of the voltage space vector, and  $i$  is the amplitude of the resulting current space vector.

As for VDC applications, the synchronous machine is typically used in combination with a spur gear stage (gear ratio  $k_g$ ), whereby the motor/generator drive torque  $T_m$  can be calculated as

$$T_m = T_i k_g. \quad (4.12)$$

Furthermore, the machine speed  $n$  can be transformed to the wheel level using the equation

$$v_{\text{whl}} = \frac{2\pi r}{k_g} n. \quad (4.13)$$

### 4.2.3 Torque control of a synchronous machine with interior magnets

For the control of electric traction drives in EVs, it is proposed to use the Field-Oriented Control (FOC). This method has a low torque ripple compared to direct torque control, which is beneficial for drive comfort and wheel slip control reasons. Usually, the FOC is maintained in applying a cascaded control structure, as shown in Figure 4.10.

The inner loop is a current control loop. The references for the voltages  $u_d$  and  $u_q$  are calculated by the  $i_d/i_q$ -controllers, which try to track reference currents  $i_{d,d}$  and  $i_{q,d}$ . As the control action is performed in the d-q system, the transformation of  $u_d$  and  $u_q$  into the a-b-c system is already included. The three resulting voltages  $u_a$ ,  $u_b$  and  $u_c$  are established by a power inverter stage (see Figure 4.7), which is directly connected to the PMSM. Measuring two stator currents and applying the inverse *Clarke/Park* transformation provides the field current  $i_d$  and the torque current  $i_q$ .

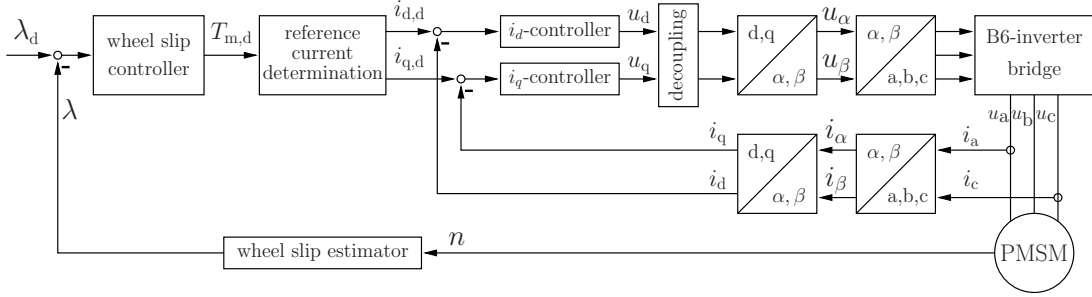


Figure 4.10: Control loop for field-oriented control

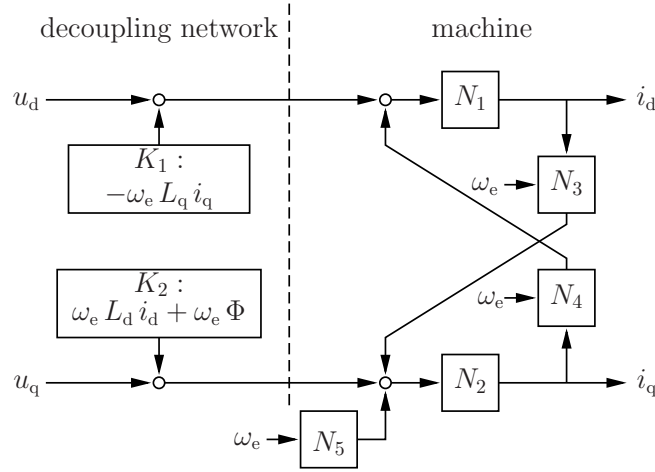


Figure 4.11: PMSM decoupling network

The outer control loop is typically a speed control loop, in which the speed error is used to determine the machine torque. In the case of VDC applications, it is proposed to utilize the wheel slip  $\lambda$  instead of the machine speed. Therefore, the wheel slip error is used to determine the desired machine torque  $T_{m,d}$ , and a coordination module is required to determine the appropriate reference currents  $i_{d,d}$  and  $i_{q,d}$ . For VDC applications, the reference value  $\lambda_d$  is typically determined by a vehicle motion controller. Chapter 6 provides additional details about wheel slip control.

In Equation (4.7), the torque control is maintained by controlling the currents  $i_d$  and  $i_q$ . Equations (4.4) and (4.5) show that the currents  $i_d$  and  $i_q$  are coupled. Displaying the differential equations graphically directly reveals the cross linkage (see Figure 4.11). This coupling is crucial for the design of the current controllers. This obstacle can be overcome by introducing decoupling mechanisms, such as those proposed in [Lun08]. Inserting the two correction terms  $K_1$  and  $K_2$  compensates for the linkage paths through  $N_3$  and  $N_4$ .

$$N_1 = \frac{1}{L_d} \frac{1}{s + \frac{R}{L_d}}; \quad N_2 = \frac{1}{L_q} \frac{1}{s + \frac{R}{L_q}}; \quad N_3 = -\omega_e L_d; \quad N_4 = \omega_e L_q; \quad N_5 = -\omega_e \Phi \quad (4.14)$$

Applying the decoupling network

$$K_1 = -\omega_e L_q i_q, \quad (4.15)$$

$$K_2 = \omega_e L_d i_d + \omega_e \Phi, \quad (4.16)$$

the decoupled systems result in the Laplace domain as

$$\frac{\mathcal{L}(i_d)}{\mathcal{L}(u_d)} = \frac{1}{L_d} \frac{1}{s + \frac{R}{L_d}} \quad (4.17)$$

and

$$\frac{\mathcal{L}(i_q)}{\mathcal{L}(u_q)} = \frac{1}{L_q} \frac{1}{s + \frac{R}{L_q}}. \quad (4.18)$$

For these two PT1 transfer functions, it is possible to design two independent current controllers, for example by using the loop shaping technique introduced in [SP96]. Instead of the derived control laws for Equations (4.17) and (4.18), the decoupling networks  $K_1$ ,  $K_2$  and the controllers have to be implemented in the ECU.

The reference values for the current controllers ( $i_{d,d}$ ,  $i_{q,d}$ ) are calculated using Equation (4.7). Since  $T_i$  results from a non-unique relation for  $i_d$  and  $i_q$ , many different combinations of  $i_d$  and  $i_q$  result in the same torque value. Due to mode-dependent physical constraints

$$u \leq U_{\max}, \quad (4.19)$$

$$i \leq I_{\max} \text{ and} \quad (4.20)$$

$$i_d < 0 \quad (4.21)$$

are present. Thus, not every combination is feasible. In the following sections, it is therefore necessary to distinguish between three modes of operation:

- constant torque mode
- field weakening mode
- field weakening mode (full load)

### Constant torque region

In the constant torque region, it is basically up to the user to calculate the reference currents, as long as mechanical constraints are not violated and the inverter operates within its limits. Following the results from [MGB07], the drive should be operated such that its losses are minimal. This can only be guaranteed, if an appropriate choice of  $i_d$  and  $i_q$  is applied to the machine. Figure 4.12 shows the desired optimal currents. From Equation (4.11), the torque current  $i_q$  is calculated as

$$i_q = \sqrt{i^2 - i_d^2}. \quad (4.22)$$

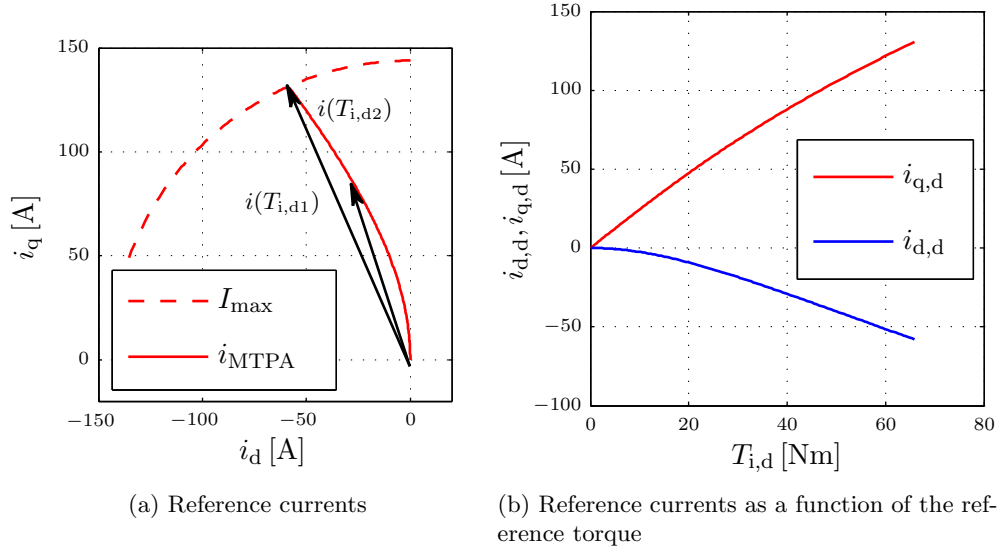


Figure 4.12: Reference currents for Maximum Torque Per Ampere mode

This current can be substituted into Equation (4.7), which leads to

$$T_i = \frac{3}{2} P (\Phi + (L_d - L_q) i_d) \sqrt{i^2 - i_d^2}. \quad (4.23)$$

The optimum current can be calculated by setting the first partial derivate of Equation (4.23) with respect to  $i_d$  to zero, that is

$$\begin{aligned} \frac{\partial T_i}{\partial i_d} &= -\frac{3}{2} P \Phi \frac{i_d}{\sqrt{i^2 - i_d^2}} + \frac{3}{2} P (L_d - L_q) \sqrt{i^2 - i_d^2} - \\ &- \frac{3}{2} P (L_d - L_q) \frac{i_d^2}{\sqrt{i^2 - i_d^2}} \stackrel{!}{=} 0. \end{aligned} \quad (4.24)$$

The appropriate field current  $i_d$  can now be calculated as

$$i_d = -\frac{\Phi}{4(L_d - L_q)} \pm \sqrt{\left(\frac{\Phi}{4(L_d - L_q)}\right)^2 + \frac{i^2}{2}}. \quad (4.25)$$

Using Equations (4.22), (4.23) and (4.25) leads to the results shown in Figure 4.12b. These values are usually stored in the ECU via a lookup-table. Using the choices for  $i_{d,d}$  and  $i_{q,d}$  guarantees that the resulting current  $i$  is a minimum, while the reference torque  $T_{i,d}$  is established. Hence, this mode is called *Maximum Torque Per Ampere* mode (MTPA). Figure 4.12a shows an example of the orientation of  $i$  for two arbitrarily selected torques  $T_{i,d1}$  and  $T_{i,d2}$ . The calculated reference values  $i_{d,d}$  and  $i_{q,d}$  can be used as long as  $n_n$  is not exceeded. If  $n_n$  is exceeded, the reference currents have to be adapted in order to fulfill field constraints.

### Field weakening region

For the field weakening operation, it is assumed that

- stationary conditions are present  $\left(\frac{di_d}{dt} = 0 \text{ and } \frac{di_q}{dt} = 0\right)$  and
- the ohmic resistance is sufficiently small.

Applying these assumptions to Equations (4.4) and (4.5) leads to

$$u_d = -\omega_e L_q i_q, \quad (4.26)$$

$$u_q = \omega_e L_d i_d + \omega_e \Phi \quad (4.27)$$

When operating in the constant torque region, the applied voltage  $u$  can be increased until  $U_{\max}$  is reached (see Figure 4.6). When operating in the field weakening region, no further increase of  $u$  is possible. The maximum allowed flux can be computed as

$$\Phi_{\max} = \frac{U_{\max}}{\omega_e}. \quad (4.28)$$

If this maximum value is exceeded for a longer time, the magnetic elements are persistently damaged. A violation of this limit should therefore be avoided at all times. Using the results from Equations (4.10), (4.26) and (4.27), the existing flux  $\Phi_e$  for an arbitrary choice of  $i_d$  and  $i_q$  is given as

$$\Phi_e = \sqrt{(L_q i_q)^2 + (L_d i_d + \Phi)^2}. \quad (4.29)$$

This equation expresses the effective flux [MGB07], which must fulfill the constraint

$$\Phi_e \leq \Phi_{\max}. \quad (4.30)$$

In Figure 4.13, the feasible flux  $\Phi_{\max}$  for different angular electric field velocities  $\omega_e = \omega_1 = 2\pi n_n P$  and  $\omega_e = \omega_2 > \omega_1$  is plotted in the d-q plane. As the speed increases these ellipses shrink. In this case, the currents must be selected such that the desired torque is established according to Equation (4.7) and constraint (4.30) is fulfilled.

In order to provide a better understanding of the actions that occur during field weakening, Figure 4.14 shows the transition from the MTPA mode to the field weakening mode. When the machine is operated with a torque  $T_{i,d}$ , the reference currents can be determined as shown in Section 4.2.3. If the angular electric field velocities reach  $\omega_1$ , the field constraint (4.30) is violated. In order to prevent machine damage, it is no longer possible to operate the machine with  $i_1$ . Another choice for  $i_d$  and  $i_q$  is required. If the intended torque should also be preserved for higher speeds as well (e.g. for  $\omega_e = \omega_2 > \omega_1$ ), the current must change along the “constant torque line” according to  $\omega$  until (4.30) is not violated. The reference currents eventually result in  $i_2$ , for example. When operating along the “constant torque line”, the inverter operates within its performance limits.

The torque can be kept constant for speeds  $\omega > \omega_2$ , as long the “constant torque line” intersects the inverter limits. This intersection point is highlighted in Figure 4.14 as operation point “A”. The length of the current vector now exceeds the inverter’s limits. If the velocity increases further, a torque reduction is inevitable. The current vector has to change along the dashed line (i.e.  $i_3$ ) in order to fulfill constraint (4.30).

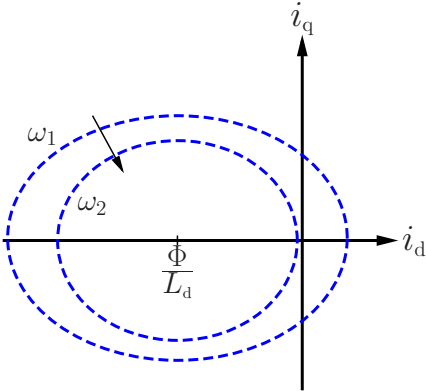


Figure 4.13: Field-weakening constraints

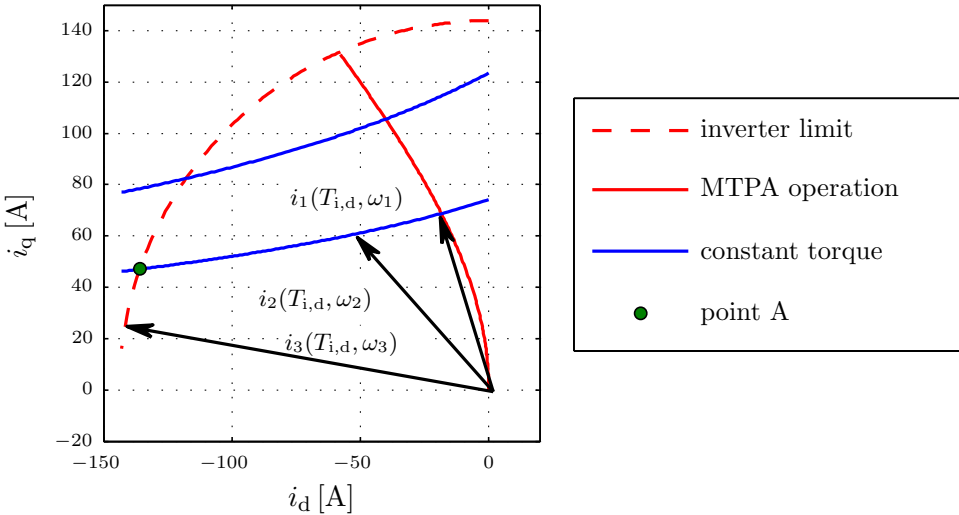


Figure 4.14: Reference currents for constant torque during field weakening

#### 4.2.4 Drag torque generation of a synchronous machine with interior magnets during electrical system faults

Synchronous machines have many benefits, which are crucial factors in their application to electric traction. Nevertheless, in the case of electric system faults, they generate an unintended drag torque. This drag torque cannot be controlled and is therefore a critical fault mode which needs to be investigated in detail. Depending on the operation of the inverter bridge, a distinction can be made between

- symmetric short circuit and
- passive rectifying.

When a machine fault is detected, the fail-safe mode must be reached as soon as possible. For both fault modes, the amount of the stationary drag torque is calculated, while alternating torques and the transient behavior to stationary conditions are omitted.

##### Symmetric short circuit

In the case of a properly operating inverter bridge, where the switching elements can be accessed as in the fault-free case, it is intended by the machine controller to operate the machine with a symmetric short circuit. This can be maintained by the switching elements of the inverter bridge (see Figure 4.7). The high side switches (S1, S2 and S3) or the low side switches (S4, S5 and S6) are closed. Using the results from [Böc11], the stationary drag torque can be calculated with the following assumptions:

- stationary conditions are present  $\left(\frac{di_d}{dt} = 0 \text{ and } \frac{di_q}{dt} = 0\right)$  and
- the voltage drops  $u_d$  and  $u_q$  are low enough to be omitted.

Inserting both assumptions into Equations (4.4) and (4.5) yields

$$0 = Ri_d - \omega_e L_q i_q \quad (4.31)$$

and

$$0 = Ri_q + \omega_e L_d i_d + \omega_e \Phi \quad (4.32)$$

These equations can be used to determine the currents  $i_d$  and  $i_q$ .

$$i_q = -\frac{\omega_e \Phi}{R + \frac{L_d L_q}{R} \omega_e^2}, \quad (4.33)$$

$$i_d = -\frac{L_q \omega_e^2 \Phi}{R^2 + L_d L_q \omega_e^2}. \quad (4.34)$$

Both currents are functions of the angular velocity  $\omega_e$ . Using the relations (4.6) and (4.7) the drag torque can be calculated as a function of the machine velocity and the wheel velocity. Figure 4.16 shows the results for the synchronous machine used for all further experiments.

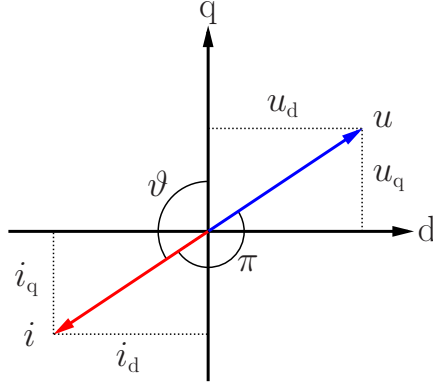


Figure 4.15: Phasor diagram of PMSM during uncontrolled generator mode operation

### Passive rectifying

Passive rectifying occurs when the proper operation of the inverter bridge is not guaranteed. Especially at higher speeds, this is negative for the vehicle motion. As stated in Section 4.2.3, the machine terminal voltage is limited by  $U_{dc}$ . If an inverter fault occurs, which causes its shutdown, the induced voltage is higher than  $U_{dc}$ . The result is that the free-wheeling diodes D1-D6 operate in their forward direction. The inverter behaves as an uncontrolled rectifier, and the machine behaves as an uncontrolled generator. Following the statements from [JC99], the generated drag can be calculated under the following assumptions:

- low ohmic resistance  $R$ ,
- stationary conditions  $\left(\frac{di_d}{dt} = 0 \text{ and } \frac{di_q}{dt} = 0\right)$  and
- the rectifier forces the resulting phase currents to be  $\pi$  out of phase compared to the voltage.

As in the case of the symmetric short circuit, the assumptions can be inserted into Equations (4.4) and (4.5), which results in

$$u_d = -\omega_e L_q i_q \quad (4.35)$$

and

$$u_q = \omega_e L_d i_d + \omega_e \Phi. \quad (4.36)$$

Since the main inductance  $L_d$  and the reluctance inductance  $L_q$  are not equal (see Section 4.2.2), the saliency ratio  $\xi$  is defined as

$$\xi = \frac{L_q}{L_d}. \quad (4.37)$$

For the machines chosen for VDC  $\xi > 2$  holds. Due to the stated assumptions, the phasor diagram looks as in Figure 4.15. The corresponding d-axis and q-axis components can be defined as

$$i_d = -i \sin(\vartheta), \quad (4.38)$$

$$i_q = i \cos(\vartheta), \quad (4.39)$$

$$u_d = u \sin(\vartheta), \quad (4.40)$$

$$u_q = -u \cos(\vartheta) \quad (4.41)$$

where

$$u = \frac{2}{\pi} U_{\text{dc}}. \quad (4.42)$$

If these results are substituted into Equation (4.35), the resulting current  $i$  is

$$i = -\frac{u \sin(\vartheta)}{\omega_e L_q \cos(\vartheta)}. \quad (4.43)$$

When the scaling factor  $\chi$  is defined as

$$\chi = \frac{\omega_e \Phi}{u}, \quad (4.44)$$

it follows for (4.44) and (4.36)-(4.38) that

$$\cos(\vartheta) = \frac{-\chi \xi + \sqrt{(\chi \xi)^2 - 4(\xi - 1)}}{2(\xi - 1)} \quad (4.45)$$

hence

$$\xi > 2 \quad (4.46)$$

and

$$\chi \geq \chi_P = \frac{2\sqrt{\xi - 1}}{\xi}. \quad (4.47)$$

The definition in (4.44) and the machine characteristic in Figure 4.6 indicate that  $\chi = 1$  if the machine is operated with  $n = n_n$ . Therefore,  $\chi$  corresponds to the ratio of back-EMF (electromotive force) voltage at a given speed. Using Equations (4.37) and (4.47), the real valued threshold  $\chi_P$  can be calculated. The currents  $i_d$  and  $i_q$  can be determined as

$$i_q = \begin{cases} i_q, & \text{if } \chi \geq \chi_P \\ 0, & \text{if } \chi < \chi_P \end{cases} \quad (4.48)$$

and

$$i_d = \begin{cases} i_d, & \text{if } \chi \geq \chi_P \\ 0, & \text{if } \chi < \chi_P \end{cases}, \quad (4.49)$$

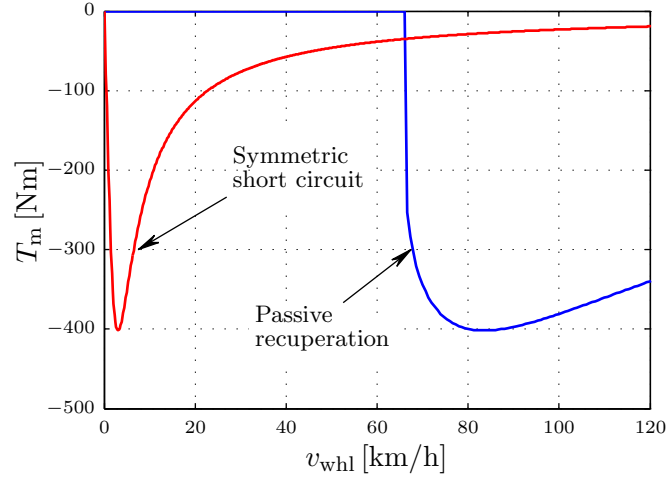


Figure 4.16: PMSM malfunction torques

while the generated drag torque is calculated using Equation (4.23). Figure 4.16 shows the resulting recuperation torque. When operating a machine at high speeds, the stated drag torque is established. If  $\chi$  falls beyond  $\chi_P$ , the torque immediately vanishes. The same happens if the inverter does not work properly and the machine accelerates (for example during driving downhill). As long as the machine is operated at lower speeds, no drag torque is generated. But when a critical velocity is reached, the drag torque shown in Figure 4.16 is rapidly generated.

#### 4.2.5 Machine approximation for wheel slip controller design

Machine control requires the mathematical model derived for the PMSM (see Section 4.2.2). Furthermore, the method for finding the reference current such that minimum energy losses occur is also needed (see Section 4.2.3). From the vehicle point of view, only the relation between the reference torque and the resulting machine torque is important, as the wheel slip controller only requires a propulsion torque. Therefore, a simpler relation for the design of the slip controller is required. To operate the traction machine with the field orientation control (see schematic diagram in Figure 4.10), two Proportional-Integral controllers (PI) are applied. One controls the field current  $i_d$  (4.17) and the other controls the torque current  $i_q$  (4.18). As these relations are only valid, if the decoupling network (see Figure 4.11) is applied, the overall machine controllers also include the decoupling terms  $K_1$  and  $K_2$  (Equations (4.15) and (4.16)). Equations (4.7) and (4.12) are used to generate the propulsion torque  $T_m$ .

Applying these controllers leads to the machine torque step response shown in Figure 4.17. As this dynamic behavior is valid for all step responses, the ratio  $T_m/T_{m,d}$  is shown instead of  $T_m$ . If the aforementioned control strategy is applied to the machine, it responds like a PT1 system. For the development of the wheel slip controller, it is

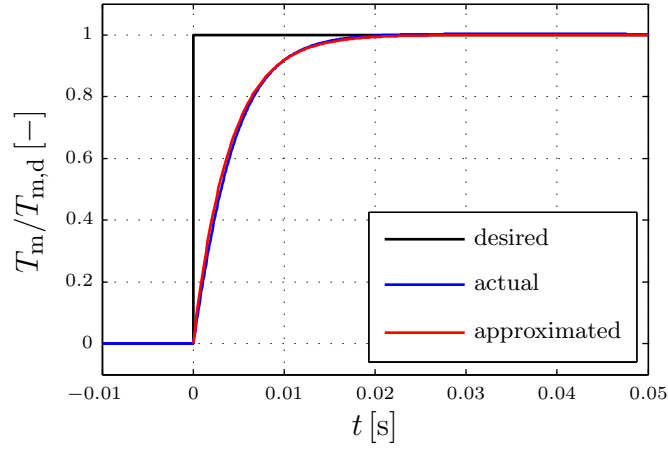


Figure 4.17: Traction machine response (PMSM)

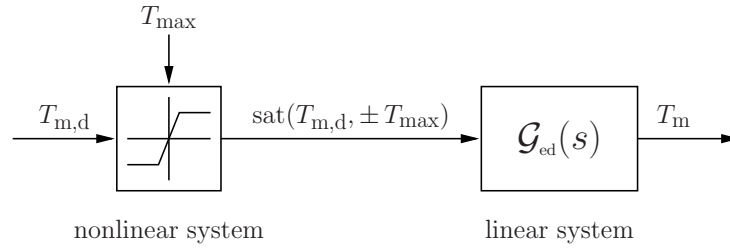


Figure 4.18: PMSM representation

therefore assumed that the machine can be regarded as a PT1 transfer function

$$\mathcal{G}_{ed}(s) = \frac{\mathcal{L}(T_m)}{\mathcal{L}(T_{m,d})} = \frac{1}{s \tau_{ed} + 1} \quad (4.50)$$

as long as it is operated in the linear range.

When the maximum machine torque  $T_{max}$  is lower than the desired machine torque  $T_{m,d}$ , the linear transfer function  $\mathcal{G}_{ed}(s)$  can be applied. Here again, the desired machine torque  $T_{m,d}$  is adapted according to  $T_{max}$  (see Figure 4.18).

# Chapter 5

## Combined actuator control

### 5.1 State-of-the-art wheel motion control

#### 5.1.1 Conventional vehicle

Today's vehicle dynamics control systems have been evolving for years. In that time, the structure of VDC algorithms has grown as a layer-based structure [Ras09, Trä05]. Figure 5.1 shows an example of the ESC torque path of a vehicle during deceleration.

Based on the driver's input, a brake torque  $T_{\text{brk,d}}$  is determined which leads to a brake pressure. As long as a desired wheel slip  $\lambda_d$  is not exceeded, no adaptation of  $T_{\text{brk,d}}$  is required. In the case that

$$|\lambda| > |\lambda_d| \tag{5.1}$$

a correction torque  $T_\lambda$  is used to keep the wheel slip within acceptable bounds and to achieve a desired wheel motion. Calculating  $T_\lambda$  is a task of the wheel slip controller (wheel dynamics controller), which is typically applied in a control loop, as shown in Figure 5.2. This control loop is an enhancement of the structure shown in Figure 2.2.

#### 5.1.2 Electric vehicle

The introducing of electric traction drives into vehicle drivetrains slightly alters the structure shown in Figure 5.1. In addition to the torque path of the ESC, a second torque path is used (see Figure 5.3). The vehicle "control" flow can now be divided into a safety-related torque path and an economy-related torque path. Typically, the safety-related torque path is located in the ESC-ECU, as in conventional vehicle applications. In contrast, the economy-related torque path is located in an additional ECU, usually called the Hybrid Control Unit (HCU) [Hof10]. The tasks of vehicle dynamics control and energy management belong to the top-level control functions (vehicle level), as they effect the whole vehicle. In order to achieve a desired vehicle motion, the ESC and HCU must exchange information. As long as the vehicle motion is non-critical from the safety perspective, the ESC only monitors the vehicle movement, while the EM controls the energy flow for the electric propulsion system.

During such situations, the driver's pedal input is measured, and the amount of intended propulsion torque  $T_{\text{d,d}}$  is calculated. Depending on the parameters of the electric

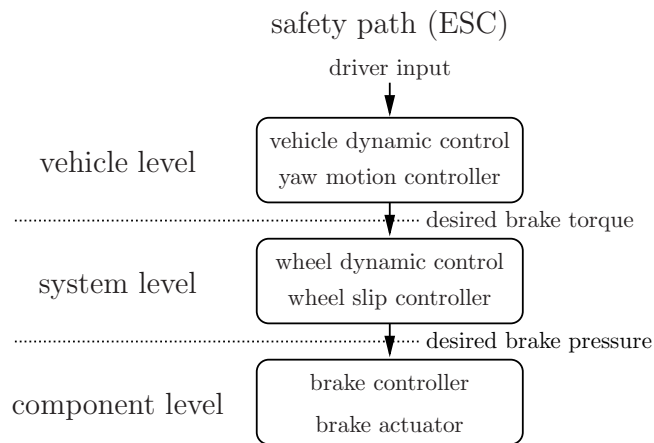


Figure 5.1: Vehicle dynamics control topology (ESC)

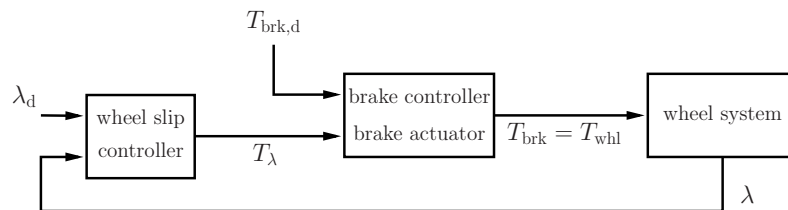


Figure 5.2: Wheel motion control loop

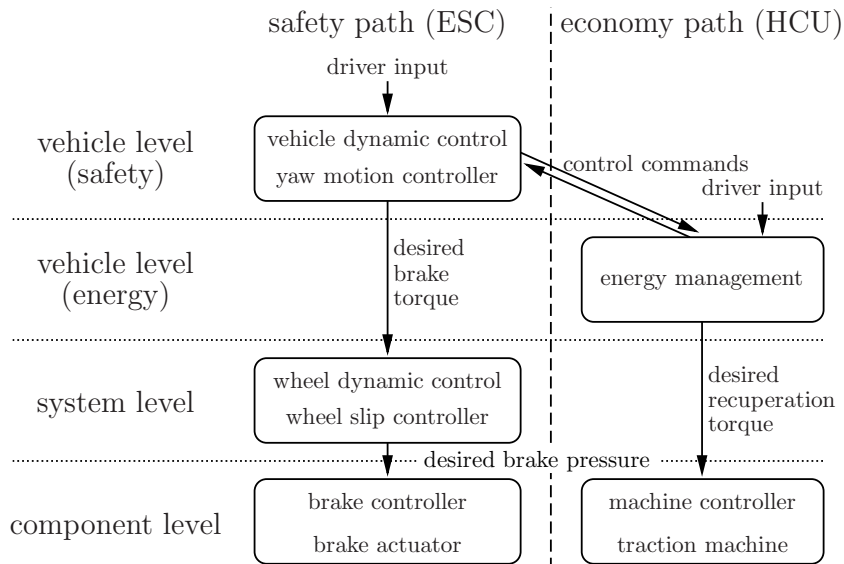


Figure 5.3: Conventional EV/HEV topology (ESC and EM)

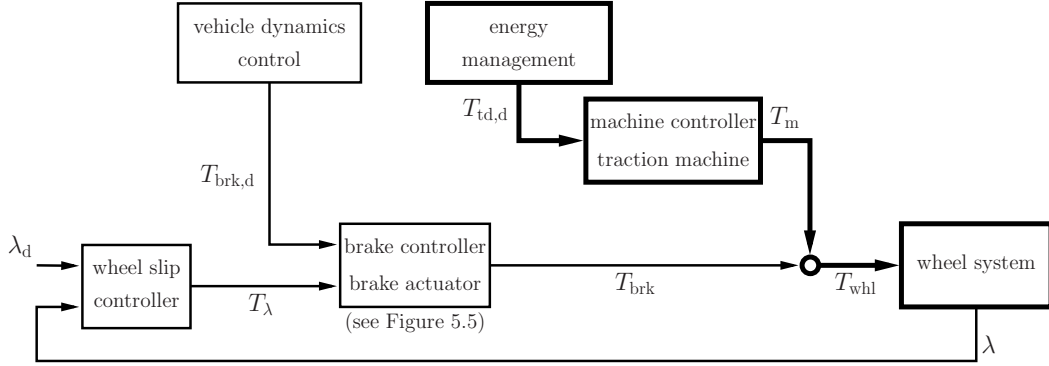


Figure 5.4: Wheel motion control loop (EV)

system (e.g. machine speed, State Of Charge (SOC) of the electric Energy Storage System (ESS)), it is possible to determine the amount of  $T_{d,d}$  which should be delivered as recuperation torque by the traction machine and which amount should be provided by the friction brake. If the schematic from Figure 5.3 is transferred to the control loop for wheel motion control, it yields the structure depicted in Figure 5.4. For all subsequent discussions, a positive  $T_{d,d}$  represents an acceleration torque, while a negative  $T_{d,d}$  characterizes a deceleration torque. As only forward driving ( $\omega > 0$ ) is considered

$$T_{d,d} \stackrel{!}{=} T_{td,d} - T_{brk,d}, \quad (5.2)$$

where  $T_{td,d}$  is the desired traction drive torque, the determination of  $T_{d,d}$ ,  $T_{td,d}$  and  $T_{brk,d}$  is not explained further.

For vehicle deceleration, the goal is to use the traction machine whenever possible to recuperate as much kinetic energy as possible. If the traction machine is applied alone, its reference value can be calculated by

$$T_{td,d} = T_{d,d} \quad (5.3)$$

and the wheel torque is

$$T_{whl} = T_m. \quad (5.4)$$

In such situations, only the bold printed path in Figure 5.4 is active. When the traction machine is unable to provide enough propulsion torque, the friction brake is used in addition. The wheel torque becomes

$$T_{whl} = T_m + T_{brk}. \quad (5.5)$$

For the following discussions, it is assumed that the “combined actuator control” refers to driving situations where both actuators are in action simultaneously.

If  $\lambda$  exceeds the desired value  $\lambda_d$ , the wheel tends to skid. In the worst case, the wheel locks. To avoid a locking wheel, the actuator torques have to be adapted according to the correction torque  $T_\lambda$ . During wheel slip control, the new reference value for  $T_{whl}$  is

$$T_{whl} \stackrel{!}{=} T_{d,d} + T_\lambda. \quad (5.6)$$

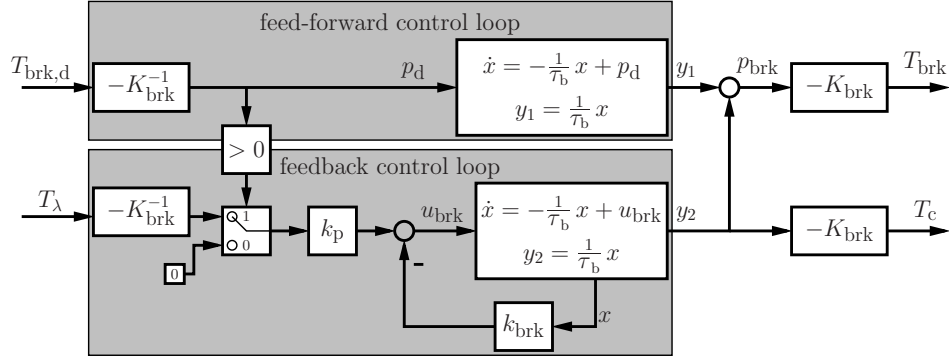


Figure 5.5: Brake control

In such driving situations, the vehicle dynamics controller takes control, as the wheel motion is more important than energy efficiency. The EM is forced to reduce the influence on the wheel motion, and in most cases the EM is completely shut down. As the traction drive is no longer used for vehicle deceleration, it follows that

$$T_m = 0. \quad (5.7)$$

The ESC corrects wheel and vehicle motion by applying the friction brakes only. This procedure is only performed for reasons of simplicity. The vehicle manufacturers trust in the effectiveness of the ESC and do not want to have an additional actuator setting up a wheel torque at this time. The control loop shown in Figure 5.4 changes to the control loop shown in Figure 5.2. Now it is possible to apply conventional ABS algorithms, as shown in Section 2.1. The braking performance achieved corresponds to the braking performance of vehicles without electric traction drives.

In order to improve the braking performance, a brake control concept where the brake torque can be adjusted continuously is used. Especially for an HAS, it is beneficial to use a control structure as shown in Figure 5.5.

This control concept consists of a feed-forward control and a feedback control part. The brake torque  $T_{\text{brk,d}}$  is the input for the feed-forward control. It is converted to a desired brake pressure  $p_d$ , which results in the brake pressure  $y_1$ . The relation between  $p_d$  and  $y_1$  can be described with a first order lag element (see Section 4.1). For the feedback control, it is proposed to use a state feedback controller with a proportional tracking gain and  $T_\lambda$  as reference input. Stabilization is achieved with the state feedback path, defined by  $k_{\text{brk}}$ , and the required tracking is achieved with the help of  $k_p$ . As explained in [Föl08], it is possible to calculate  $k_{\text{brk}}$  by selecting the strictly positive weighting parameters  $q_1$  and  $r_1$  and solving the *algebraic Riccati equation*. The tracking gain yields

$$k_p = -\frac{1}{\frac{1}{\tau_b} \left( -\frac{1}{\tau_b} - k_{\text{brk}} \right)^{-1}}. \quad (5.8)$$

The control law applied in the feedback control part results in

$$u_{\text{brk}} = -k_{\text{brk}} x - k_p K_{\text{brk}}^{-1} T_\lambda \quad (5.9)$$

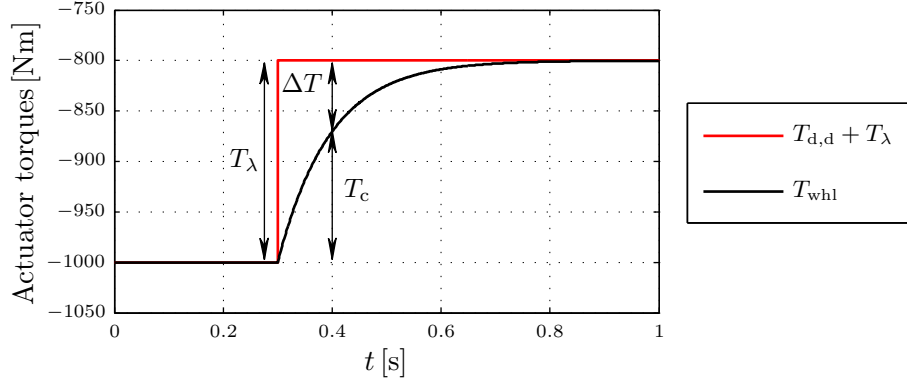


Figure 5.6: Torque response based to the friction brake

and leads to the brake pressure  $y_2$ . Together with the output of the feed-forward control, it yields the friction torque

$$T_{\text{brk}} = -K_{\text{brk}} (y_1 (T_{\text{brk,d}}) + y_2(T_{\lambda})). \quad (5.10)$$

In addition to the brake torque  $T_{\text{brk}}$ , the control structure also provides important information for combined control. The torque  $T_c$  represents the brake torque that results from the wheel slip controller torque  $T_{\lambda}$ . This value is calculated as

$$T_c = -K_{\text{brk}} y_2 \quad (5.11)$$

and can be used to determine the reference value for the traction machine.

Since the brake pressure can only achieve positive values, an activation of the slip control only makes sense if

$$p_d > 0. \quad (5.12)$$

### Simulation result:

To evaluate the performance of the friction brake controller, a simple experiment is carried out. Figure 5.6 shows a deceleration maneuver with a wheel slip controller intervention. It is assumed that the driver's input is interpreted such that  $T_{\text{d,d}} = -1000\text{Nm}$ , and the traction drive is already switched off. Since the vehicle decelerates exclusively by means of friction braking,  $T_{\text{brk,d}} = T_{\text{d,d}}$ . For the experiment, it is assumed that  $T_{\text{brk,d}}$  is constant during the maneuver and that the vehicle enters a slippery road section at time  $t = 0.3\text{s}$ . As (5.6) holds, the wheel slip controller calculates a correction torque which results in  $T_{\lambda} = 200\text{Nm}$ . In the example in Figure 5.6, the overall wheel torque has to increase to  $T_{\text{whl}} = -800\text{Nm}$  instantaneously. As the friction brake is relatively slow, it takes approximately 0.4s to achieve the new reference value.

It can be concluded that a desired wheel motion is achieved, but valuable kinetic energy is transformed into heat losses. The ESS remains uncharged, and the potential of using traction drives for wheel motion control is not exploited.

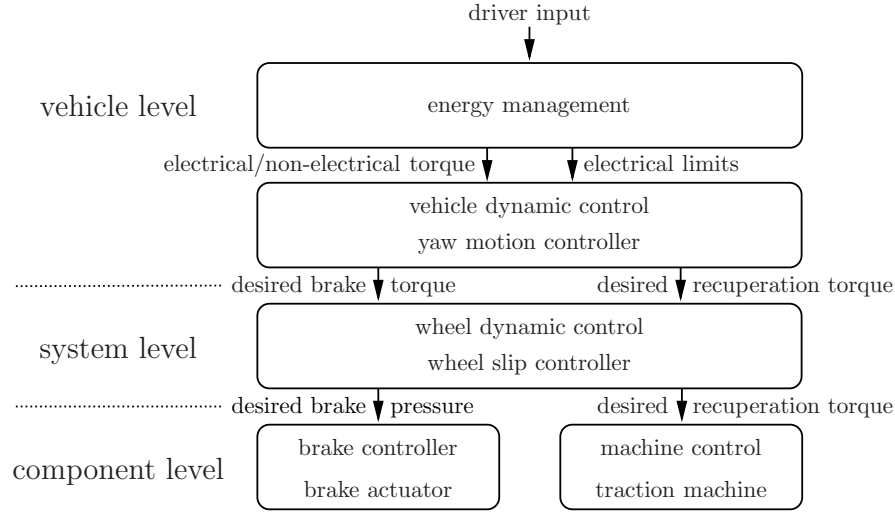


Figure 5.7: Combined EV/HEV topology (VDC and EM)

## 5.2 Wheel motion control for electric vehicles using combined actuator control

With the previously mentioned structure, relatively slow actuators are used to control the wheel slip. The possibility of controlling  $\lambda$  with faster, energy-efficient actuators is not taken into consideration. As the wheel slip controller in Figure 5.3 has no connection to the EM, it is not possible to incorporate the traction machine into wheel slip control. This can be seen as the major drawback of the concept described in Section 5.1.2. Based on the statements from literature (e.g. [SSWM11] and [STP11]), the dynamics of electric drives offer high potential to improve traction performance and driving efficiency.

Figure 5.7 shows a structure of the torque path that can be used to overcome the aforementioned drawback. Here, the EM defines the electrical and non-electrical propulsion torques. Furthermore, it calculates the electrical limits (i.e. the maximum recuperation torque) as constraints for the VDC. In the case of critical driving situations, set values from the EM are adapted by the VDC in order to achieve a desired vehicle motion. Otherwise, they remain unchanged. Based on the calculations of the VDC, the reference torques for the friction brake and the traction machine are determined. Due to interactions between the VDC and the EM, it is possible to access the friction brake and the traction machine concurrently for wheel slip control. Additionally, it is possible to implement VDC functionalities and EM functionalities within *one* ECU.

The next task is to define the interaction of the friction brake and the traction machine during wheel slip control. From the brake control concept introduced in Figure 5.5, it is clear that  $T_\lambda$  is the reference value for  $T_c$ . The results from Figure 5.6 show that the torque difference

$$\Delta T = T_\lambda - T_c \tag{5.13}$$

represents the control error which results from the slow brake system response.  $\Delta T$  remains

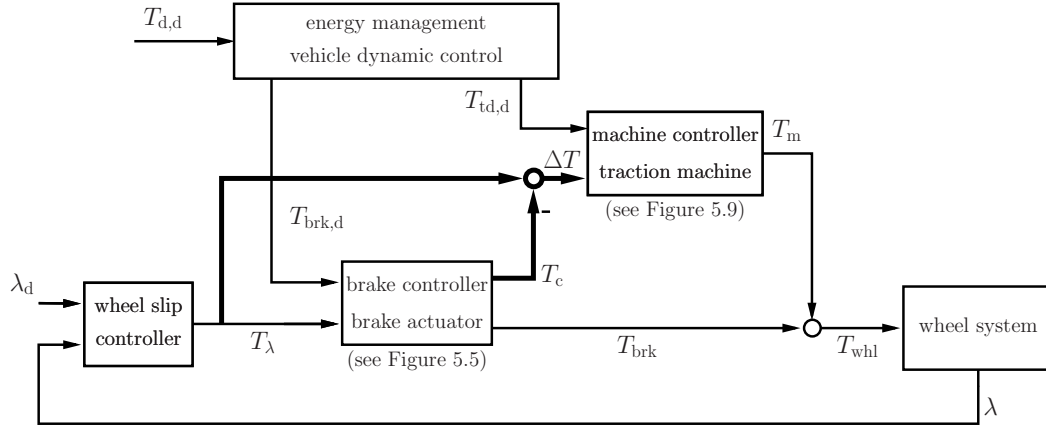


Figure 5.8: Wheel motion control loop (combined control)

zero if the desired wheel motion is present (i.e. no wheel slip control), but it achieves high values in the case of insufficient brake torque dynamics. The torque difference  $\Delta T$  must be reduced to zero as quickly as possible. Thus, extended sliding of the tires' rubber particles can be prevented, and the stable region of the tire force can be quickly regained. The step responses in Figures 4.3 and 4.17 show that the traction machine is faster than the brake system.

Thus, the idea is now to improve the torque response of the HAS by using the knowledge of  $\Delta T$  to adapt the traction machine torque accordingly. Transferring this idea into a control loop results in the structure shown in Figure 5.8. The interconnection of brake actuator control and traction machine control results in a so-called daisy chain structure. The two actuators are linked together in a serial connection. They support each other in achieving a desired wheel torque  $T_{whl}$  by using an additional information exchange. The friction brake operates as explained in Section 5.1.2, but due to the connections shown in bold in Figure 5.8, the traction machine adapts its recuperation torque according to  $T_\lambda$  as well. The actuator torques are adapted such that the fast torque transients are performed with the traction machine, while the slow torque transients are maintained with the friction brake. Instead of shutting the recuperation down during wheel slip control, the traction drive can maintain  $T_{td,d}$  most of the time. The traction machine only reduces recuperation for a short time when it becomes necessary to change the wheel torque with high slew rates. The two goals of attaining high energy recuperation and ensuring a desired wheel motion can thus be achieved concurrently.

To set up the recuperation torque  $T_m$ , it is proposed to use the concept shown in Figure 5.9, which consists of two main parts. The first part represents the feed-forward control, where the intended traction machine torque  $T_{td,d}$  is used as input. According to the results presented in Section 4.2, the EM-intended propulsion torque results in the machine torque  $y_3$ . The second part is the feedback control, where an integral state feedback controller is utilized. As reference input, the control error  $\Delta T$  is used. Stabilization is achieved with the state feedback path, defined by  $k_{td}$ , and asymptotic tracking is achieved

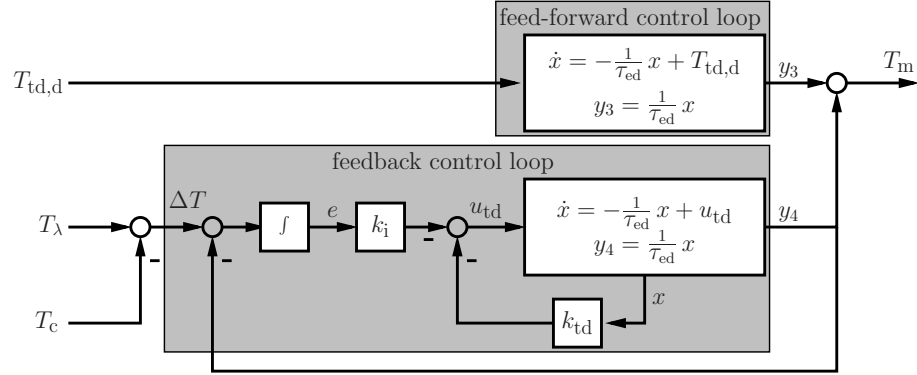


Figure 5.9: Traction machine control

with the help of the integral action and  $k_i$ . The control law results in

$$u_{td} = -k_{td} x - k_i \int_0^t (\Delta T - y_4) d\tau, \quad (5.14)$$

where  $y_4$  is the output torque of the feedback control loop. Applying this controller to the dynamic system derived in Section 4.2.5 leads to the augmented plant

$$\begin{bmatrix} \dot{x} \\ \dot{e} \end{bmatrix} = \begin{bmatrix} -\frac{1}{\tau_{ed}} - k_{td} & -k_i \\ -\frac{1}{\tau_{ed}} & 0 \end{bmatrix} \begin{bmatrix} x \\ e \end{bmatrix} + \begin{bmatrix} 0 \\ 1 \end{bmatrix} \Delta T = \tilde{\mathbf{A}} \begin{bmatrix} x \\ e \end{bmatrix} + \tilde{\mathbf{b}} \Delta T. \quad (5.15)$$

The parameters  $k_{td}$  and  $k_i$  have to be chosen such that the real parts of the eigenvalues of the augmented dynamic matrix  $\tilde{\mathbf{A}}$  are negative. In the case of the traction drive, the strictly positive weighting parameters  $q_2$ ,  $q_3$  and  $r_2$  define the influence of  $x$ ,  $e$  and  $u_{td}$  and on the cost function

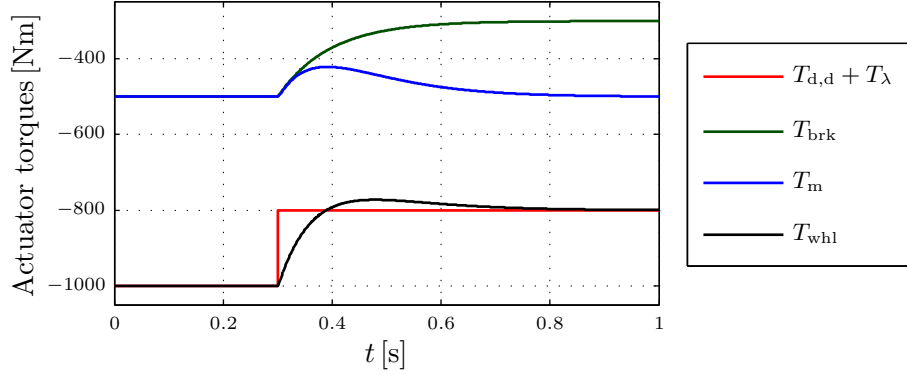
$$J(x, e, u_{td}) = \int_0^{\infty} (q_2 x^2 + q_3 e^2 + r_2 u_{td}^2) d\tau. \quad (5.16)$$

By solving the *algebraic Riccati equation*, the controller parameters  $k_{td}$  and  $k_i$  are calculated. The machine torque  $T_m$  resulting from the feed-forward control and the feedback control reads as

$$T_m = y_3(T_{td,d}) + y_4(\Delta T). \quad (5.17)$$

Beyond the advantage of attaining high energy recuperation, a further benefit arises. As  $T_m$  is a linear combination of  $y_3$  and  $y_4$ , it is not possible to overcharge the ESS in the case of wheel slip control. Due to the fact that  $T_\lambda$  always counteracts the intended recuperation torque  $T_{td,d}$ , the recuperation torque can only be decreased. An ESS overload is avoided as

$$|T_m(T_\lambda = 0)| > |T_m(T_\lambda > 0)|. \quad (5.18)$$


 Figure 5.10: Torque response with combined actuator control ( $\mathcal{P}_1$ )

Whenever  $T_\lambda$  reaches negative values, this is an indicator that no more wheel slip control is required. The feedback part can be switched off, and the output of the integrator in (5.14) must be forced to zero. Now, only the feed-forward control defines  $T_m$ .

#### Simulation results:

The same experiment as in Section 5.1.2 is performed, but now the friction brake and the traction machine are utilized in a concurrent manner. Figures 5.10 and 5.11 show the results. For  $t < 0.3s$ , it follows that

$$y_1 \neq 0; y_2 = 0; y_3 \neq 0; y_4 = 0, \quad (5.19)$$

as the actuator torques are defined by their feed-forward control, and no wheel slip controller intervention is required. Entering the slippery road section at  $t \geq 0.3s$  leads to

$$y_1 \neq 0; y_2 \neq 0; y_3 \neq 0; y_4 \neq 0, \quad (5.20)$$

as  $T_\lambda \neq 0$ . When the actuator controllers (5.9) and (5.14) are applied for combined HAS control, then the parameter set

$$\mathcal{P} = \{q_1, q_2, q_3, r_1, r_2\} \quad (5.21)$$

defines the dynamic response of  $T_{whl}$ . Depending on the selection of  $\mathcal{P}$ , different wheel torque responses are possible. For performance demonstration, the experiment is conducted for two different weighting parameter sets  $\mathcal{P}_1$  and  $\mathcal{P}_2$ . The set  $\mathcal{P}_1$  is chosen such that the resulting wheel torque reaches the desired value slowly. As shown in Figure 5.10, the traction machine adapted its torque  $T_m$  instantaneously, but only for the time period

$$0.3s < t < 0.7s. \quad (5.22)$$

As long as  $T_c$  is a low value, the output  $y_4$  is mainly influenced by  $T_\lambda$ . As  $T_c$  increases, the influence of  $T_\lambda$  on the traction machine decreases. If

$$\Delta T = 0 \quad (5.23)$$

the machine torque reaches

$$T_m = T_{td,d}, \quad (5.24)$$

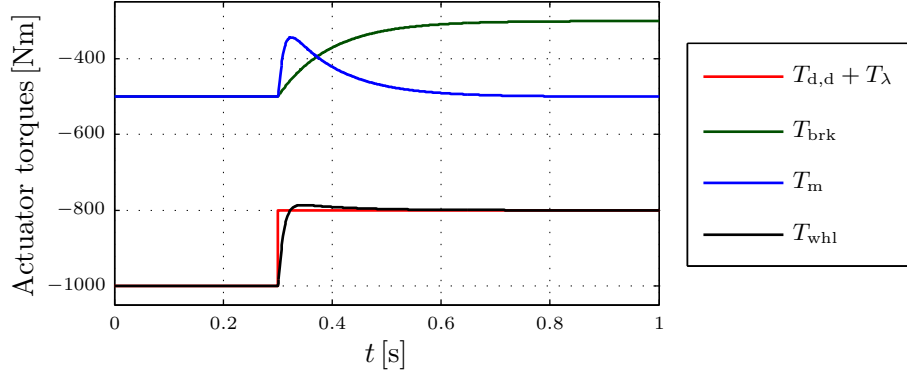


Figure 5.11: Torque response with combined actuator control ( $\mathcal{P}_2$ : fast response)

as intended by the EM. For the experiment, it follows that

$$T_m(t < 0.3s) = -500\text{Nm} \rightarrow T_m(t > 0.7s) = -500\text{Nm}. \quad (5.25)$$

The output torque for the brake actuator is defined as

$$T_{brk} \stackrel{!}{=} T_{brk,d} + T_{\lambda}. \quad (5.26)$$

It changes according to

$$T_{brk}(t < 0.3s) = -500\text{Nm} \rightarrow T_{brk}(t > 0.7s) = -300\text{Nm}. \quad (5.27)$$

Focusing on the transient response of  $T_{whl}$ , it can be seen that  $T_{whl}$  changes faster than with the application of the friction brake alone, but a slight overshoot appears. The introduction of  $T_{\lambda}$  effectively influences  $T_{brk}$ , but for the torque response, the electric traction drive is also in charge. Instead of shutting down energy recuperation for means of wheel slip control, the recuperation rate is now decreased only for performing high torque slew rates.

The dynamic response can be improved further by selecting the parameter set  $\mathcal{P}_2$ . Figure 5.11 shows the achieved results. This is beneficial for emergency braking situations, for example. With an appropriate choice of  $\mathcal{P}$ , it is possible to “tune” the response of the HAS. Furthermore, it is possible to store different sets  $\mathcal{P}_1, \mathcal{P}_2, \dots$  in the ECU to define the response behavior based on such factors as

- the driving situation
- the user-selected vehicle configuration
- the availability of the electric system

### 5.2.1 Fail-silent properties of combined actuator control

In the case of a driving situation where one actuator fails silent (no torque output of one actuator), the daisy chain causes a safe behavior as well. Due to the interlaced structure

(see Figure 5.8), it is safeguarded that the healthy actuator adapts its torque if the other actuator is inoperable.

If the traction machine fails silent during wheel slip control, the wheel slip controller torque  $T_\lambda$  is generated with the friction brake. Although the energy efficiency is unfortunately lost, a safe vehicle state can be achieved.

If the friction brake fails silent,  $T_c$  becomes

$$T_c = 0. \tag{5.28}$$

From that time onwards, the wheel slip control is utilized for recuperative braking only. The ESS might be overcharged, but again a safe vehicle deceleration is possible.

## Chapter 6

# Wheel slip control

The energy management algorithm has the task of providing the propulsion torque according to the driver's inputs. As shown in Figures 5.5-5.8,  $T_{td,d}$  and  $T_{brk,d}$  are only for feed-forward purposes. If the wheel is operated on a slippery road, the resulting wheel propulsion torque  $T_{whl}$  could cause an unintended high wheel slip

$$|\lambda| > |\lambda_d|. \quad (6.1)$$

When a critical wheel slip is exceeded, the longitudinal tire force behaves as

$$\frac{\partial F_x}{\partial \lambda} \leq 0, \quad (6.2)$$

as the tire's rubber particles skid on the road surface [Fac99, MM95]. Additionally, it is shown in [Jaz09] that the overall tire force potential is bounded according to *Kamm's* circle

$$F_x^2 + F_y^2 \leq \mu^2 F_z^2. \quad (6.3)$$

The more longitudinal tire force  $F_x$  generated, the less lateral tire force  $F_y$  is available. Both circumstances lead to the conclusion that high wheel slips must be avoided in order to establish a desired wheel motion. Additionally, a low wheel slip is required to establish high lateral tire forces  $F_y$ , in order to prevent the vehicle from unintended yaw motion. An additional mechanism that holds  $\lambda$  within reasonable bounds is required. This mechanism is introduced as the wheel slip controller.

### 6.1 Wheel slip controller design

The wheel motion can be described with the aid of the model introduced in Section 3.4. The application of the principle of angular momentum leads to Equation (3.33). Equations (3.33), (3.35) and (3.36) now define the relation between the wheel torque  $T_{whl}$ , the tire force  $F_x$  and the wheel slip  $\lambda$ . This yields

$$\dot{\lambda} = \frac{r}{v(J_y + J_{veh})} T_{whl} - \frac{r^2}{v(J_y + J_{veh})} F_x(\mu, \lambda). \quad (6.4)$$

Equation (6.4) represents a dynamic system with two inputs. The first input is the wheel torque  $T_{\text{whl}}$ , and the second input is the uncertain tire force  $F_x$ . For low values of  $\lambda$ , the longitudinal tire force can be estimated using Equation (3.1). As shown in Figure 3.6, it is possible to approximate the tire characteristic for high values of  $\lambda$  by applying a tanh-function and a polynomial of sufficiently high degree. Although these simplifications support the calculation of the tire force, the tire force also depends on the uncertain road surface friction coefficient  $\mu$  (see Figure 3.2). When the vehicle is driven on ice, the minimum surface friction coefficient results in  $\underline{\mu} \approx 0.1$ , while driving on dry asphalt causes a maximum surface friction coefficient of  $\bar{\mu} \approx 1$ . Following the results of [LEH11], the exact determination of  $\mu$  cannot be performed with reasonable efforts. Nevertheless, a rough estimation of  $\mu$  is still possible.

If the wheel torques of the front wheels are known, they can be used to classify  $\mu$  for the rear wheels. High wheel torques indicate that the road surface friction coefficient is high, while low wheel torques indicate low- $\mu$  conditions. Moreover, if the wheel propulsion torque  $T_{\text{whl}}$  is known,

$$\frac{\partial \omega}{\partial T_{\text{whl}}} \quad (6.5)$$

can also be used for a rough categorization of  $\mu$  [VZ05]. For high- $\mu$  conditions, the result of (6.5) is low, while for low- $\mu$  conditions, it is very high. Assuming that the road surface friction coefficient is

$$\mu = \hat{\mu} = \frac{\underline{\mu} + \bar{\mu}}{2}, \quad (6.6)$$

the second summand in Equation (6.4) can be calculated with the help of Equation (3.26). In Equation (6.6),  $\hat{\mu}$  denotes the nominal road surface friction coefficient. The required tire radius  $r$ , the moments of inertia  $J_y$  and  $J_{\text{veh}}$  are known within some bounds and the vehicle speed  $v$  can be estimated [Bre11]. If the calculation is performed for a vehicle velocity interval

$$\underline{v} \leq v \leq \bar{v} \quad (6.7)$$

and for a wheel slip interval

$$\underline{\lambda} \leq \lambda \leq \bar{\lambda}, \quad (6.8)$$

it leads to the surface shown in Figure 6.1. Figure 6.1 shows the results for vehicle deceleration (i.e. a negative  $\lambda$ ). The velocity bounds  $\underline{v}$  and  $\bar{v}$  are chosen such that the whole range of vehicle operation is covered. The bounds  $\underline{\lambda}$  and  $\bar{\lambda}$  of the wheel slip cover the stable region and parts of the unstable region of the tire force.

In Figure 6.1, it can be seen that the slew rate is nearly constant when higher negative wheel slips occur. Furthermore, it is evident that the absolute values of the slew rate increase as the vehicle velocities decrease.

In addition to the calculations for  $\hat{\mu}$ , the wheel slip slew rate can be calculated for  $\mu = \underline{\mu}$  and  $\mu = \bar{\mu}$ . The results can be depicted in Figure 6.1, as well. The differences between the surfaces represent the uncertainties which arise because the exact  $\mu$  is not known. It can be seen that, especially at lower speeds, a good estimate of  $\mu$  is required.

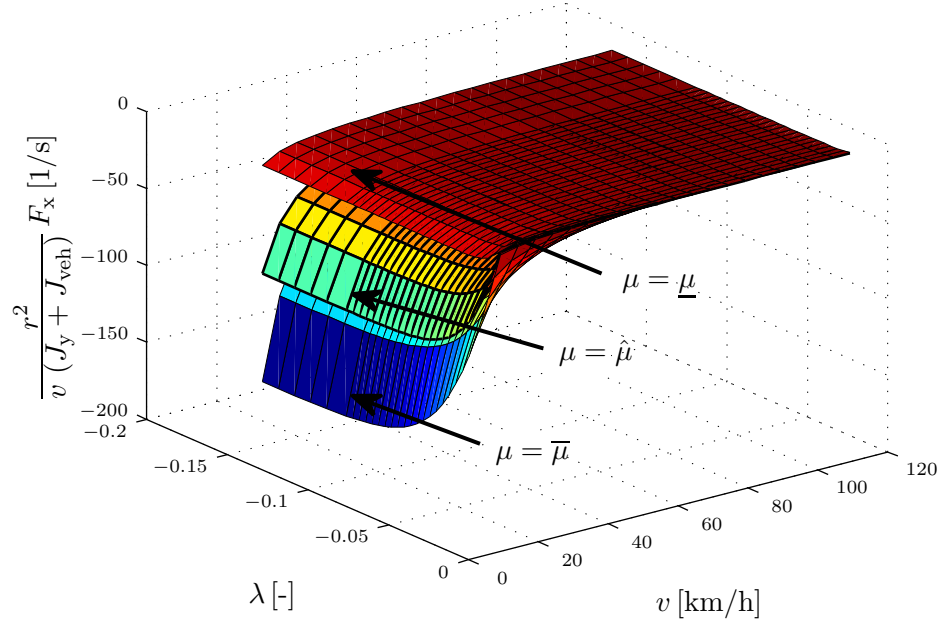


Figure 6.1: Model uncertainty

Furthermore, the uncertainty  $\Delta$  of the wheel torque varies with the wheel slip. Using Equation (3.26), the maximum value for the uncertainty can be calculated with

$$\Delta = \max \left( \left| r (F_x(\hat{\mu}, \lambda) - F_x(\underline{\mu}, \lambda)) \right|, \left| r (F_x(\hat{\mu}, \lambda) - F_x(\bar{\mu}, \lambda)) \right| \right). \quad (6.9)$$

The control input in (6.4) is the wheel torque  $T_{\text{whl}}$ . Following the results from Section 5, the wheel torque results in

$$T_{\text{whl}} = T_{\text{d,d}} + T_{\lambda}. \quad (6.10)$$

As  $T_{\text{d,d}}$  is defined by the driver, the remaining  $T_{\lambda}$  can be used to achieve a desired wheel motion. The task is to develop a wheel slip controller for stabilizing the wheel motion by means of  $T_{\lambda}$ .

In order to cope with the uncertain road surface friction coefficient, a robust control approach is required [UGS99, SL99]. As Sliding Mode (SM) approaches are well suited for controlling plants with uncertainties [HHR08, HR08], such an approach is applied to control the wheel slip [dCAF12, RH11]. Theoretical background information for the SM controller design is provided in Appendix A.

Comparing the dynamics of the drivetrain actuators with the wheel slip transfer function (3.37), it can be concluded that the actuators are fast enough to be omitted for the wheel slip controller design. The overall output torque of the SM wheel slip controller reads as

$$T_{\lambda} = \hat{T}_{\lambda} + T_{\lambda, \text{sw}}, \quad (6.11)$$

where  $\hat{T}_\lambda$  represents the equivalent control, and  $T_{\lambda,\text{sw}}$  is the discontinuous control. The wheel slip error  $\tilde{\lambda}$  is defined as

$$\tilde{\lambda} = \lambda - \lambda_d. \quad (6.12)$$

The sliding variable  $\sigma$  is chosen as

$$\sigma(\lambda, t) = \tilde{\lambda} + \gamma \int_0^t \tilde{\lambda} d\tau, \quad (6.13)$$

where

$$\gamma > 0 \quad (6.14)$$

is a tuning parameter to ensure that the control error  $\tilde{\lambda}$  converges to zero. The scalar equation  $\sigma(\lambda, t) = 0$  defines the sliding surface, which should be an invariant set, as shown in Appendix A. For reasons of readability, the expression  $\sigma(\lambda, t)$  is replaced by  $\sigma$  in the subsequent statements. It is the task of the wheel slip controller to drive

$$\sigma \stackrel{!}{=} 0. \quad (6.15)$$

Assuming that the reference wheel slip  $\lambda_d$  is constant and the vehicle is driving on  $\hat{\mu}$ , the torque  $\hat{T}_\lambda$  must be applied. This leads to

$$\dot{\sigma} = 0 = \frac{r}{v(J_y + J_{\text{veh}})} (T_{d,d} + \hat{T}_\lambda) - \frac{r^2}{v(J_y + J_{\text{veh}})} F_x(\hat{\mu}, \lambda) + \gamma(\lambda - \lambda_d) \quad (6.16)$$

and results in

$$\hat{T}_\lambda = r F_x(\hat{\mu}, \lambda) - \gamma \frac{v(J_y + J_{\text{veh}})}{r} (\lambda - \lambda_d) - T_{d,d}. \quad (6.17)$$

As previously stated,  $\mu$  is uncertain. Thus, an additional control input  $T_{\lambda,\text{sw}}$  is required. If a large enough parameter  $K_\lambda$  is chosen, meaning

$$K_\lambda > \Delta \quad (6.18)$$

and

$$T_{\lambda,\text{sw}} = -K_\lambda \text{sgn}(\sigma), \quad (6.19)$$

then  $\sigma$  is an invariant set. Control law (6.19) requires ideal switching, which is not present in practice. This results in undesirable high actuator workloads. Furthermore, the so-called ‘‘chattering’’ occurs. To achieve a trade-off between actuator workload and control accuracy, the control signal  $T_{\lambda,\text{sw}}$  has to be suitably smoothed. This can be achieved if (6.19) is substituted by

$$T_{\lambda,\text{sw}} = -K_\lambda \text{sat}\left(\frac{\sigma}{\phi}\right). \quad (6.20)$$

The strictly positive tuning parameter  $\phi$  characterizes the width of the so-called boundary layer (see Appendix A). At low speeds, a good control performance can be achieved when a wider boundary layer is applied. This is required, as the wheel slip slew rate reaches higher values at lower speeds, which could cause a skidding wheel (see Figure 6.1). In order to avoid vehicle instability at higher speeds the boundary layer width should be low to ensure a higher converging speed. Therefore, it is proposed that  $\phi$  should be adapted based on the vehicle speed. Furthermore, it is essential to get some information about how the wheel slip will vary, in order to counteract it quickly enough. The wheel acceleration  $\dot{\omega}$  is a good indicator for future slip values. For high slew rates, it is proposed to support the wheel slip controller [Web05], for example by introducing an additional feed-forward torque

$$T_p = T_p(\dot{\omega}). \quad (6.21)$$

The overall torque of the wheel slip controller now reads as

$$T_\lambda = r F_x(\hat{\mu}, \lambda) - \gamma \frac{v(J_y + J_{\text{veh}})}{r} (\lambda - \lambda_d) - T_{d,d} - K_\lambda \text{sat}\left(\frac{\sigma}{\phi}\right) + T_p. \quad (6.22)$$

Additionally, simulations have shown [RH11] that the weighting parameter  $\gamma$  should be chosen as

$$\gamma = \gamma(|\lambda - \lambda_d|). \quad (6.23)$$

This improves the convergence speed, especially when the road surface coefficient changes.

Applying electric traction machines for wheel slip control requires that the slip controller and the machine controller run on the same ECU. For the practical realization, the wheel slip controller is implemented on a hardware platform that also includes the machine power inverter (see Figure 4.7). The slip controller operates with a frequency of 500Hz, which is typical for torque control applications in the automotive industry. In order to compute the SM algorithms on the power inverter, the control of the friction brake and the traction machine must take place on the same ECU as well. The control unit including all three controllers can be seen as a “smart” actuator unit.

Having the wheel slip controller and actuator controller on the same platform yields additional further advantages (e.g. the shared use of sensor information). State-of-the-art wheel slip controllers use the signals from wheel speed sensors to calculate the wheel slip. From [Rei07], it is known that conventional wheel speed sensors have limitations (e.g. in terms of sample rate or in their range of operation). In contrast to wheel slip control applications, machine control applications require the angular positioning of the machine rotor with a high accuracy [Kri01]. When the wheel slip controller is implemented on a machine power inverter, it is beneficial to compute the wheel speed with the help of the rotor position sensor. The wheel speed sensor can be used for fail-safe strategies or can be completely removed.

The following section describes the performance of the derived SM controller.

## 6.2 Simulation results

### 6.2.1 Comparison between ABS and HAS

To verify the performance of the wheel slip controller, a braking maneuver under high- $\mu$  and under low- $\mu$  conditions is performed. The conditions for high- $\mu$  relate to  $\mu = 1$ , whereas the low- $\mu$  conditions relate to  $\mu = 0.2$ . As stated in Chapter 2, the performance of the conventional ABS is compared to the performance of an ABS supported by an HAS.

The subsequent figures only show the signals relevant for the rear axle wheels. An intervention of the yaw motion controller, which adapts the left-hand side and the right-hand side accordingly, is not required. Therefore, the signals of both wheels are assumed to be the same. The results for the front axle are omitted as well, as in both configurations the front axle is equipped with a friction brake only. For purposes of better comparability, the torque  $T_m$  is mirrored on the abscissa.

Figures 6.2 and 6.3 show the deceleration maneuver applying ABS without HAS support. As only the friction brake is used, the recuperation torque  $T_m$  is forced to be zero. The brake pressure changes according to the sequence introduced in Chapter 2.

Figures 6.4 and 6.5 depict the performance of the ABS utilizing HAS control. It is expected that only the traction machine torque limits the maximum possible recuperation torque. The SOC is low enough to recharge the ESS using full machine power. This is an interesting scenario, as the maximum recuperation torque varies during the maneuver. When the vehicle starts to decelerate, both actuators are accessed due to the limited recuperation torque  $T_{\max}$ . When the resulting wheel slip  $\lambda$  exceeds the maximum allowed wheel slip  $\lambda_d$ , a wheel slip controller intervention is required. In the case of both high- $\mu$  and low- $\mu$ , the torque

$$T_{\text{whl}} = T_m - K_{\text{brk}} p_{\text{brk}} \quad (6.24)$$

is adapted such that the reference wheel slip  $\lambda_d$  is achieved.

In the high- $\mu$  scenario, the friction brake and the traction machine are applied simultaneously. Therefore, this tests how the controller behaves when the traction machine is not able to provide sufficient deceleration torque. The torque characteristic of the traction machine is clearly visible in Figure 6.4. As soon as the electrical system can provide a sufficiently high propulsion torque, the friction brake is disengaged.

In the low- $\mu$  scenario, the hydraulic system is only accessed to overcome the venting backlash of the friction brake and to support the traction machine during the first moments of braking. Subsequently, the traction machine provides enough recuperation torque to achieve the reference slip  $\lambda_d$ . The friction brake is no longer used.

The potential of the fast actuator is used, and kinetic energy can be restored. Even though the wheel slip controller has no knowledge of the exact  $\mu$  value,  $\lambda_d$  can be reached very well in both cases.

In simulations, it is possible to observe the longitudinal tire forces. Figure 6.6 shows the forces  $F_x$  that result from all four maneuvers (ABS braking/HAS braking under low- $\mu$ /high- $\mu$  conditions). It is clearly visible that the HAS can reach the wheel slip  $\lambda_d$  effectively, even though the unstable tire force region is entered. This is beneficial for the braking distance. Table 6.1 summarizes the achieved results.

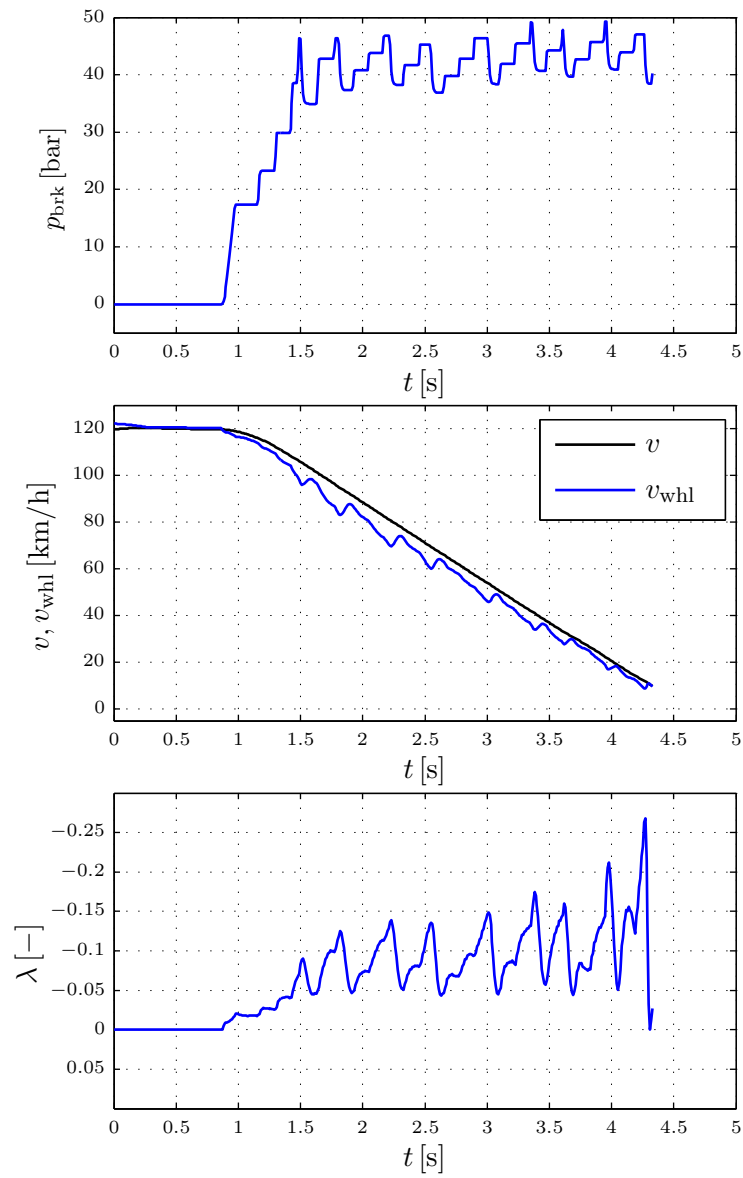


Figure 6.2: ABS braking under high- $\mu$  conditions

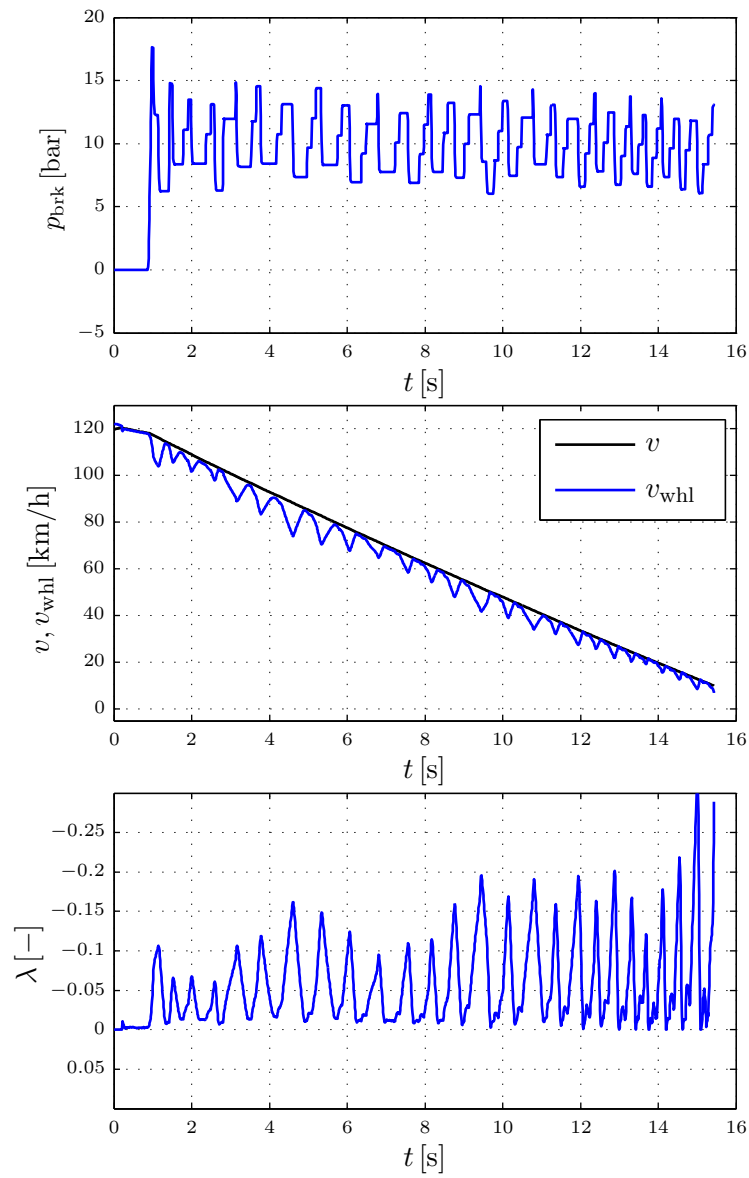


Figure 6.3: ABS braking under low- $\mu$  conditions

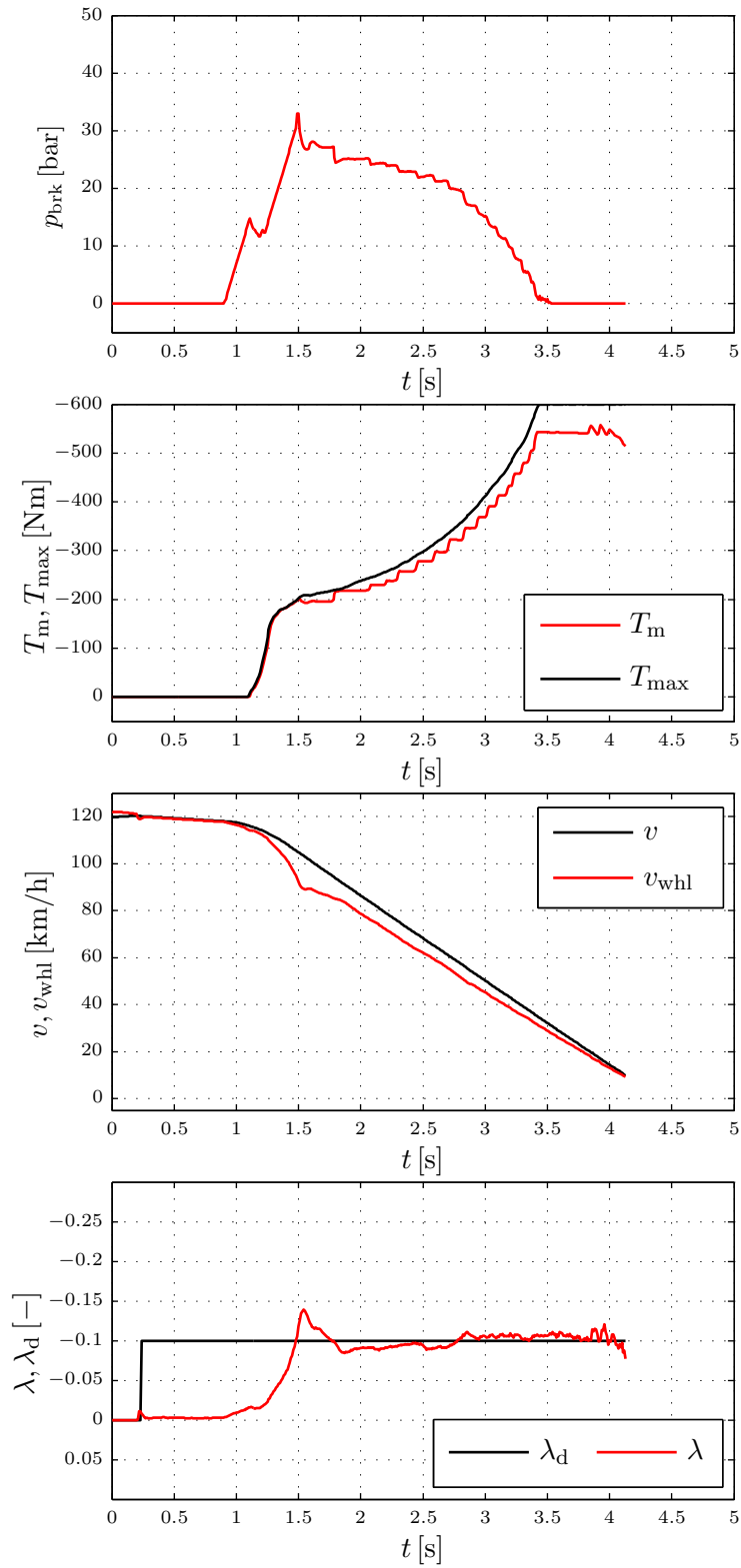


Figure 6.4: HAS braking under high- $\mu$  conditions

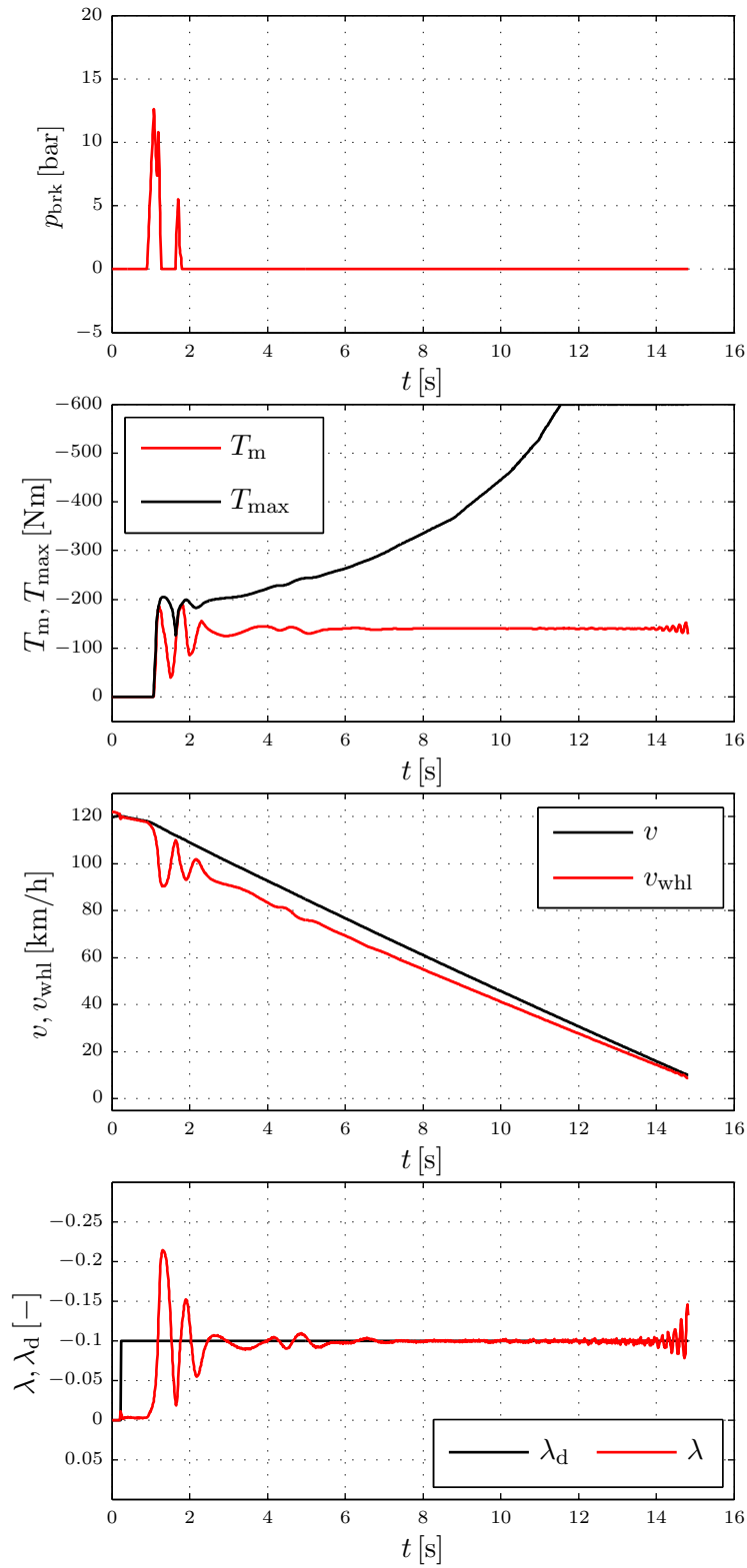


Figure 6.5: HAS braking under low- $\mu$  conditions

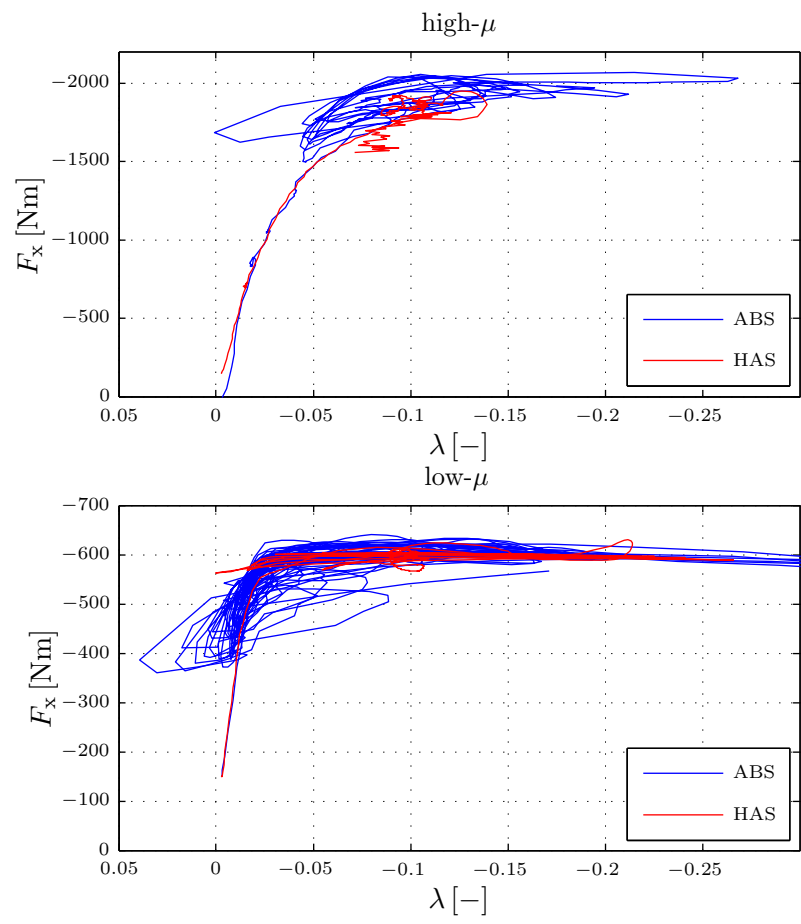


Figure 6.6: Longitudinal tire forces during ABS and HAS braking

<i>Maneuver</i>	<i>Brake distance</i>	<i>Improvement</i>	<i>Figure</i>
ABS braking under high- $\mu$ conditions	65.3m	-	6.2
HAS braking under high- $\mu$ conditions	61.8m	3.5m	6.4
ABS braking under low- $\mu$ conditions	253.5m	-	6.3
HAS braking under low- $\mu$ conditions	245.2m	8.3m	6.5

Table 6.1: Simulation results for ABS/HAS braking

### 6.2.2 Robustness tests

To evaluate the performance of the wheel slip controller, a braking maneuver starting from  $v = 80\text{km/h}$  is conducted. This maneuver is used to focus on the performance of the wheel slip controller in the case of a braking maneuver on country roads. In order to test the robustness against varying  $\mu$  conditions, the maneuver is conducted for five different road surface friction coefficients  $\mu \in \{1, 0.8, 0.5, 0.35, 0.2\}$ .

Three different configurations are tested:

- ABS: The deceleration performance of a vehicle equipped with a conventional ABS is the benchmark for the HAS.
- HAS (recuperation): In this configuration, it is assumed that a high performance traction machine can cover the wheel torque on its own. The friction brake is not accessed.
- HAS (combined): This configuration utilizes the friction brake and the traction machine concurrently.

Table 6.2 summarizes the results. Both HAS configurations perform better than the conventional ABS.

## 6.3 Test bench results

The performance of the wheel slip controller using the HAS is tested on an ABS test bench, as well (Appendix B provides further details about the test bench itself).

To evaluate the performance of the HAS, four different configurations are tested:

- Wheel slip control using the conventional ABS (benchmark, see Figure 6.7)
- HAS wheel slip control using the friction brake (see Figure 6.8)
- HAS wheel slip control using energy recuperation (see Figure 6.9)
- HAS wheel slip control using energy recuperation and friction brake concurrently (see Figure 6.10)

<i>Road condition</i>	<i>System</i>	<i>Brake distance</i>	<i>Improvement</i>
$\mu = 1$	ABS	29.6m	-
	HAS (recuperation)	28m	1.6m
	HAS (combined)	28.3m	1.3m
$\mu = 0.8$	ABS	33.8m	-
	HAS (recuperation)	32.6m	1.2m
	HAS (combined)	32.9m	0.9m
$\mu = 0.5$	ABS	49.6m	-
	HAS (recuperation)	48.1m	1.5m
	HAS (combined)	48.5m	1.1m
$\mu = 0.35$	ABS	69.9m	-
	HAS (recuperation)	66.6m	3.3m
	HAS (combined)	66.7m	3.2m
$\mu = 0.2$	ABS	118.2m	-
	HAS (recuperation)	116.2m	2m
	HAS (combined)	114.1m	4.1m

Table 6.2: Simulation results for ABS/HAS braking (robustness)

### 6.3.1 Test procedure

The vehicle is accelerated to its maximum speed and then decelerated as quickly as possible. This immediate braking maneuver is intended to provoke an intervention of the wheel slip controller. The braking maneuvers are performed automatically in order to make the experiments reproducible. Therefore, the actuation valve V (see Figure B.2) is used to emulate the driver's input and to generate a supply pressure within the main brake cylinder. All maneuvers are carried out with a very low tire load force. This corresponds to low- $\mu$  conditions ( $\mu \approx 0.2$ ), where the controller shows high activity. The wheel slip control action is maintained until the velocity  $v$  of the vehicle is less than 4km/h.

Figure 6.7 depicts the braking performance for the ABS control. The braking maneuver is initiated by actuating valve V. This valve is only accessed to trigger the braking maneuver. For brake pressure control, the valves shown in Figure B.4 are used (see Section B.3 for detailed information about the brake actuation).

In the case of the HAS friction brake control, the actuation valve V is used to initiate the braking maneuver, as well. During the slip controller intervention, the valve V is controlled such that the intended brake torque  $T_{\text{brk}}$  is established. The ABS valves, which are not accessed, remain in the position shown in Figure B.4.

### 6.3.2 Test results

Figures 6.7-6.10 show the results for the different configurations.

**Wheel slip control using the conventional ABS (benchmark):** The benchmark system shows that the desired value  $\lambda_d$  cannot be achieved (see Figure 6.7). The resulting wheel slip oscillates with a low frequency and a high amplitude around the desired value. This is due to the fact that the ABS valves V1 and V2 can only be operated in their positions “completely open” or “completely closed”. As shown in relation (3.37), it is clear that the dynamics of the wheel slip change with the vehicle speed. This is also evident from Figure 6.7. The lower the vehicle velocity, the higher the oscillation amplitudes. The traction machine is not applied, so the recuperation torque  $T_m$  remains at zero.

**HAS wheel slip control using the friction brake:** During HAS braking, the SM wheel slip controller determines the required friction brake torque. The ABS valves are not accessed. The actuation valve V is utilized to achieve the desired brake pressure. After the first overshoot of the wheel slip, the desired wheel slip can be achieved quickly (see Figure 6.8). Nevertheless, disturbances and oscillations are noticeable. The disturbances are also evident during combined control, but not in the benchmark configuration. The results described in Section B.4 confirm the assumption that stick-slip effects are present within the actuation cylinder and the main brake cylinder. As the phenomenon of high-frequently oscillations is also identifiable for other drivetrain configurations, further investigations are carried out (see Appendix B). The observed oscillations are not caused by the wheel slip controller, but rather result from load force variations, as shown in Section B.5. Due to the high frequency of these oscillations, the proposed controller is not able to suppress them completely. Here again, the traction machine is not applied, so the recuperation torque  $T_m$  remains at zero.

**HAS wheel slip control using energy recuperation:** When the electrical system is able to provide a sufficiently large torque  $T_m$ , the performance shown in Figure 6.9 can be achieved. Due to the fast response of the traction machine, the desired wheel slip is reached quickly. Nevertheless, high-frequently oscillations caused from variations of the load force are present. Since the traction machine is faster than the friction brake, it intends to counteract the load force variations. This is done by rapidly adapting the recuperation torque. In the case of recuperative braking, the friction brake is not accessed. As shown in Figure 6.6, the wheel enters the unstable region of the tire force only for a short period of time. This prevents the rubber particles of the tire from extended skidding, which is beneficial for the braking distance. Applying the traction machine only results in the shortest braking distance.

**HAS wheel slip control using energy recuperation and friction brake:** The ideal case for energy recuperation and short braking distances is provided when the deceleration is performed with the traction machine only. This requires high recuperation torques and the possibility to charge the ESS with a high current. If one of the requirements is not fulfilled, then the combined control must be used. In this experiment, the traction machine is limited in its maximum accessible torque by means of software (here:  $|T_m| \leq 5\text{Nm}$ ). A reduction of the machine torque takes place when the wheel slips are too high and the friction brake is too slow (see Figure 6.10). In contrast to HAS braking with the friction brake, the traction machine is used here to increase the response of the requested wheel torque. Especially at lower speeds, the braking performance can be im-

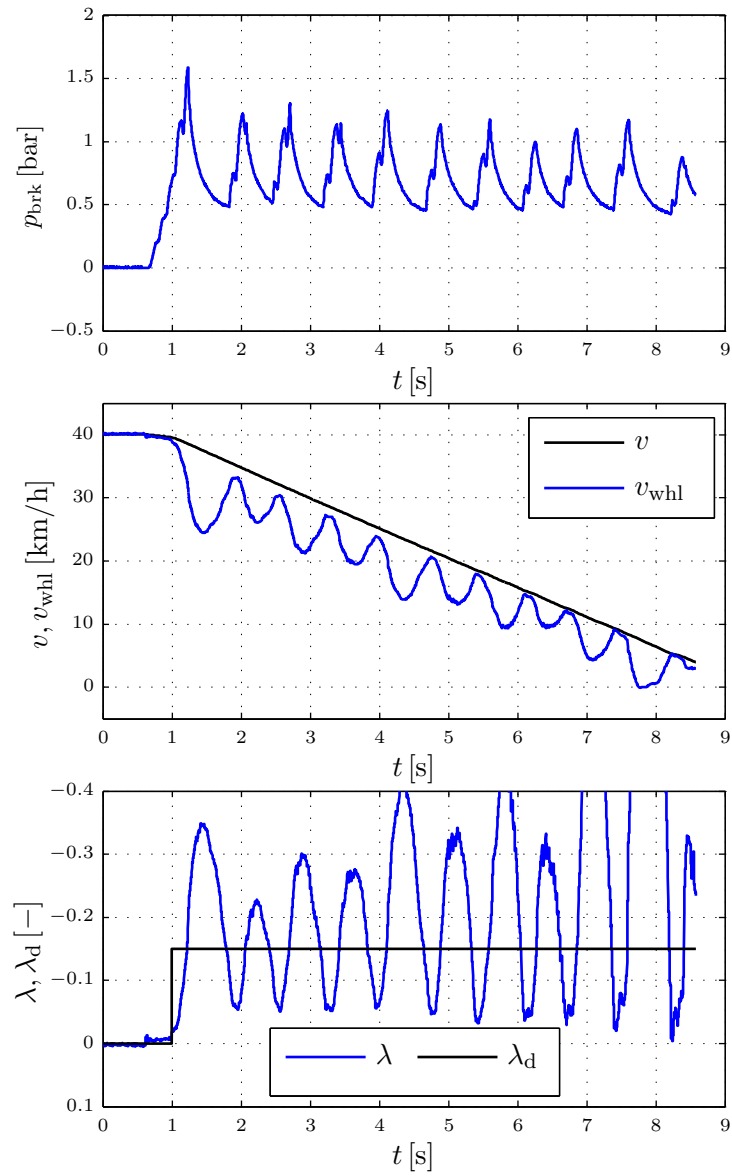


Figure 6.7: Wheel slip control using the conventional ABS (test bench)

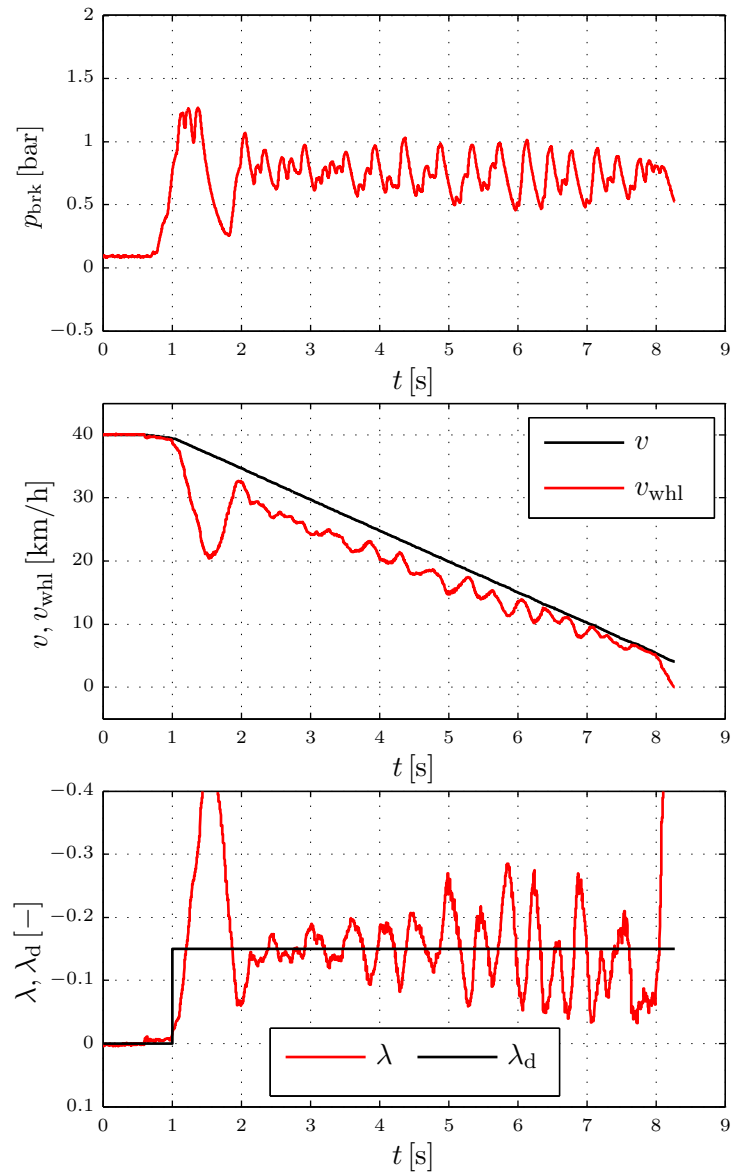


Figure 6.8: HAS wheel slip control using the friction brake (test bench)

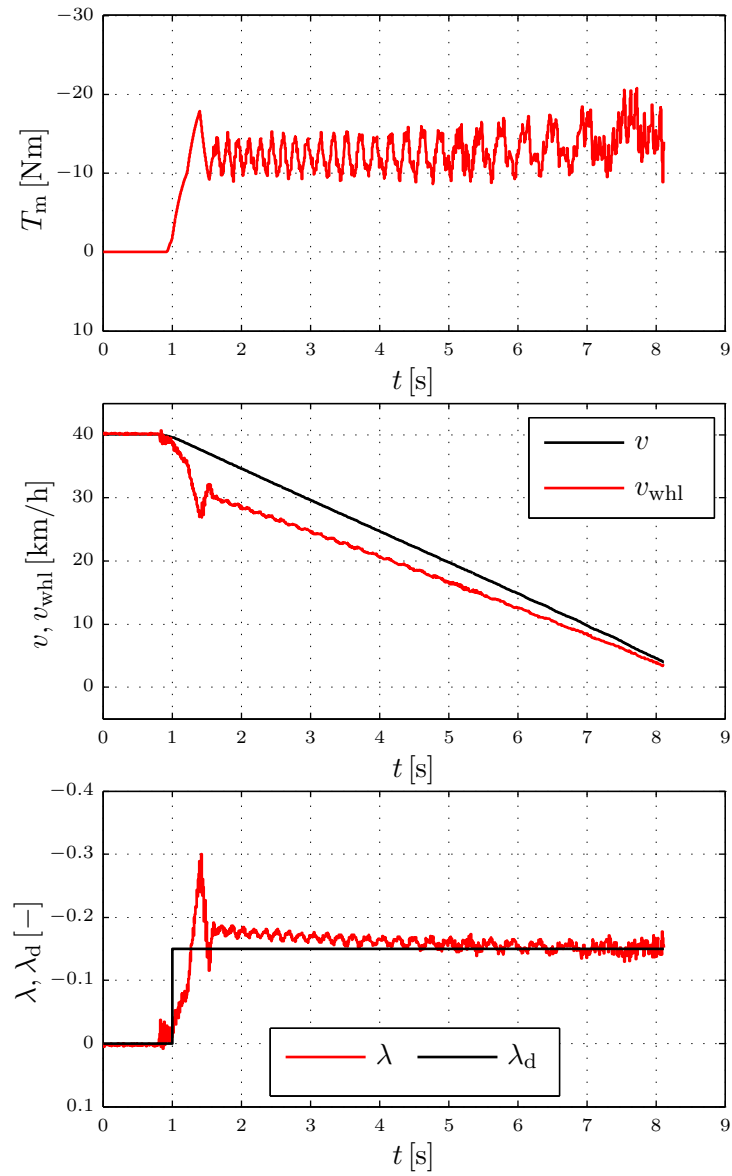


Figure 6.9: HAS wheel slip control using energy recuperation (test bench)

<i>Maneuver</i>	<i>Brake distance</i>	<i>Improvement</i>	<i>Figure</i>
Wheel slip control using the conventional ABS	45.4m	-	6.7
HAS wheel slip control using the friction brake	44m	1.4m	6.8
energy recuperation	43.4m	2m	6.9
energy recuperation and friction brake	43.6m	1.8m	6.10

Table 6.3: Test bench results for ABS and HAS braking

proved. Nevertheless, this configuration requires an exchange of information between the inverter and the ECU. As the communication performance is a specific property of this test bench, it limits the overall system performance. Unfortunately, it limits the ability to validate the real performance of the combined HAS control. For vehicle applications, this communication delay is reduced significantly. Computing the controllers on only one ECU (e.g. on the inverter ECU) would completely avoid this communication effort.

**Summary:** From Table 6.3, it can be concluded that the SM wheel slip controller offers benefits over the standard ABS in terms of braking performance. All configurations applying the SM wheel slip controller require shorter braking distances to stop the vehicle than the conventional ABS. Especially at lower speeds, the proposed wheel slip controller performs better.

Comparing the configurations, it can be seen that the configuration with the fastest actuator performs best. This is clear, as the recuperation torque can be adapted very quickly. Applying the SM controller for combined braking leads to a short braking distance as well, but the wheel slip deviations cannot be suppressed perfectly. As explained in Appendices B.1 and B.2, the overall control software has been divided into two parts, due to resource limitations on the power inverter ECU. The slip controller and the machine control are hosted by the power inverter ECU, while the brake control is located within a second ECU. This requires a high communication effort between the two systems.

The resulting dead time is very high compared to the response time of the traction machine. Therefore, the performance of the traction machine cannot be exploited completely. Nevertheless, the braking distance is less than only using the conventional friction brake. Furthermore, the traction machine can be used for energy harvesting purposes.

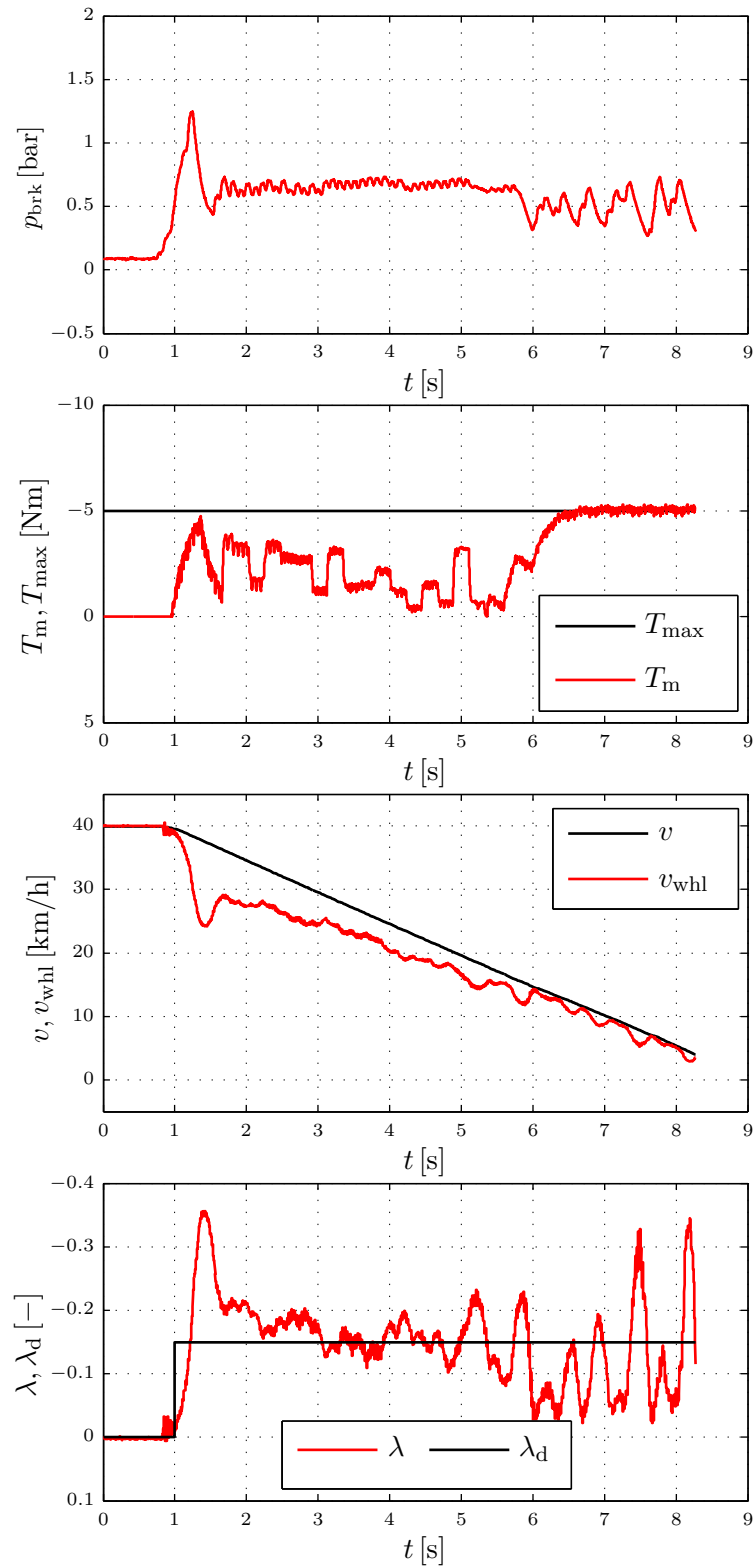


Figure 6.10: HAS wheel slip control using energy recuperation and friction brake (test bench)

# Chapter 7

## Lateral vehicle dynamics control

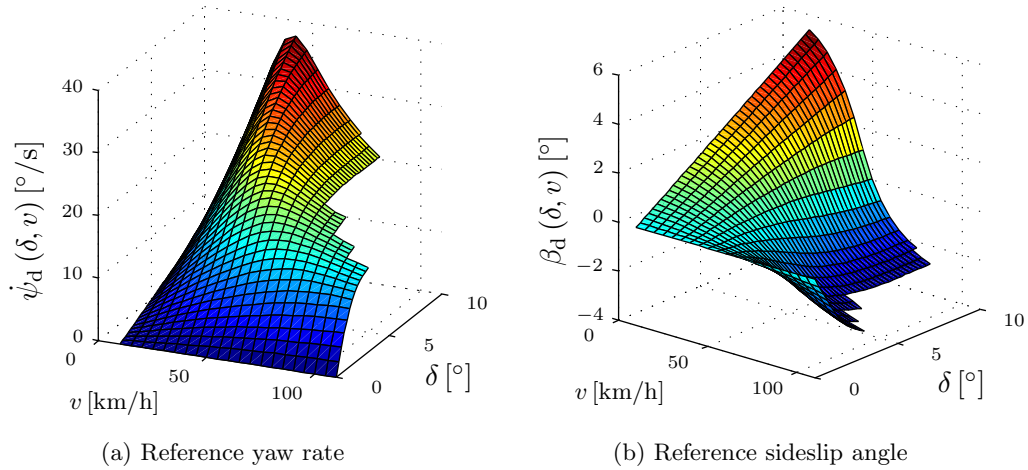
### 7.1 Reference value computation for yaw motion control

One of the tasks of the driver is to plan the trajectory the vehicle is intended to follow. In order to keep the vehicle on the planned trajectory, the driver chooses an appropriate steering wheel angle  $\delta$  [Amm97]. Based on this input, a yaw motion is generated. As long as the actual yaw motion corresponds to the steering input, no additional control action is required. The driver's steering input can thus be interpreted as a reference for the yaw rate  $\dot{\psi}_d$  and the sideslip angle  $\beta_d$ . The following discussions are based on the assumption that the vehicle is driving forward on a left curve.

The relevant literature describes, different approaches for computing the reference values for the yaw rate  $\dot{\psi}_d$  and the sideslip angle  $\beta_d$  based on the single-track model or the two-track model (e.g. [Ise06], [Ram05], [LS08]). Here, the reference values for stationary conditions are calculated. In order to keep the calculation of the reference values straightforward, the reference values in this thesis are derived from a nonlinear two-track model (3.52) at a steady-state cornering maneuver, which is simulated in Dyna4<sup>TM</sup>. The vehicle performs a cornering maneuver, whereby the steering input is kept constant. The vehicle velocity changes very slowly, so it can be assumed that  $\ddot{\psi} = 0$  and  $\dot{\beta} = 0$ . This corresponds to the method for calculating the equilibrium point of a system with the state variables  $\dot{\psi}$  and  $\beta$  [Föl93]. This yields the yaw rate  $\dot{\psi}_d(\delta, v)$  and the sideslip angle  $\beta_d(\delta, v)$ , as shown in Figure 7.1.

When the vehicle at low- $\mu$  turns according to the reference values calculated for high- $\mu$ , high sideslip angles occur. Most drivers cannot handle such angles, as they are typically familiar with sideslip angles of  $|\beta| < 4^\circ$ . When the sideslip angle moves towards higher values, an additional correction of the yaw rate is necessary. First, the reference values for the yaw rate are adapted based on the road surface conditions. Typically, different parameter sets are used to perform such adaptations. As the road surface conditions cannot be measured with a reasonable effort, it is not possible in this case to apply different parameter sets as a function of different  $\mu$ . Therefore, a different strategy for adapting the values for the reference yaw rate is required. At steady state conditions, the time-derivative of the sideslip angle  $\beta$  is zero. From Equation (3.46), it follows that

$$\dot{\psi}_d(a_y, v) = \frac{a_y}{v}. \quad (7.1)$$

Figure 7.1: Yaw motion reference values for high- $\mu$ 

Assuming that the complete tire force potential is used, the desired yaw rate can be estimated with

$$\dot{\psi}_{e,d} = \min \left( \dot{\psi}_d(\delta, v), \dot{\psi}_d(a_y, v) \right). \quad (7.2)$$

Figure 7.1 shows the yaw rate  $\dot{\psi}_{e,d}$  for high- $\mu$  conditions and the reference value for the sideslip angle. Since the lateral acceleration reaches high values, the results from (7.1) have no influence on (7.2). When the vehicle is driving at low- $\mu$ ,  $a_y$  is low as well. The value of  $\dot{\psi}_{e,d}$  is limited by the result from Equation (7.1).

Although the reference yaw rate is adapted to low- $\mu$  and high- $\mu$  conditions, high sideslip angles may still occur. This is the case when the yaw rates are low and the vehicle starts to drift. In such a driving situation the strict tracking of the reference yaw rate is of minor importance, since most drivers feel uncomfortable when high sideslip angles occur. In a second step, the vehicle motion must be adapted such that the sideslip angle is bounded. It is necessary to limit the reference sideslip angle to a maximum feasible value which is denoted as  $\beta_{lim}$ . The reference value for the sideslip angle is bounded by

$$\beta_d = \min (|\beta_d(\delta, v)|, \beta_{lim}) \operatorname{sgn} (\beta_d(\delta, v)). \quad (7.3)$$

As the threshold of the sideslip angle for which drivers feel uncomfortable vary (e.g. depending on their level of driving experience), most Original Equipment Manufacturers (OEMs) provide the possibility to choose the  $\beta_{lim}$  from predefined values (e.g. sport mode, comfort mode, etc.).

Section 7.2 describes the design of a yaw motion controller, that supports drivers in the fulfillment of their driving tasks.

## 7.2 Yaw motion control

The design of the yaw motion controller is based on the bicycle model (3.47), which is then extended by an additional input torque  $T_z$ . The state space model results in

$$\begin{bmatrix} \ddot{\psi} \\ \dot{\beta} \end{bmatrix} = \begin{bmatrix} -\frac{c_{\alpha,R} l_R^2 + c_{\alpha,F} l_F^2}{J_z v} & \frac{c_{\alpha,R} l_R - c_{\alpha,F} l_F}{J_z} \\ \frac{c_{\alpha,R} l_R - c_{\alpha,F} l_F}{m v^2} - 1 & -\frac{c_{\alpha,F} + c_{\alpha,R}}{m v} \end{bmatrix} \cdot \begin{bmatrix} \dot{\psi} \\ \beta \end{bmatrix} + \begin{bmatrix} \frac{c_{\alpha,F} l_F}{J_z} \\ \frac{c_{\alpha,F}}{m v} \end{bmatrix} \delta + \begin{bmatrix} \frac{1}{J_z} \\ 0 \end{bmatrix} T_z. \quad (7.4)$$

The yaw torque  $T_z$  is generated with the help of the HAS. It directly influences  $\dot{\psi}$ , while the sideslip angle  $\beta$  is indirectly affected via  $\dot{\psi}$ . As discussed in Section 7.1, the driver assumes that the vehicle responds based on the steering wheel input. Thus a cascaded control structure is applied, whereby the yaw rate control loop is the inner control loop. As already stated in Chapter 3, uncertainties in terms of vehicle parameters (e.g.  $l_F$ ,  $l_R$ ,  $m$ ) are present. Additionally, it is very expensive to measure the sideslip angle  $\beta$ . Therefore, the use of optical sensors, for example, is only possible for prototype vehicles. In order to deal with these uncertainties, an SM controller is applied (see Appendix A).

### 7.2.1 Sliding mode yaw rate control

From (7.4) the differential equation for the yaw rate control reads as

$$\ddot{\psi} = -\frac{c_{\alpha,R} l_R^2 + c_{\alpha,F} l_F^2}{J_z v} \dot{\psi} + \frac{c_{\alpha,R} l_R - c_{\alpha,F} l_F}{J_z} \beta + \frac{c_{\alpha,F} l_F}{J_z} \delta + \frac{1}{J_z} T_z. \quad (7.5)$$

The yaw rate control error  $\tilde{\psi}$  is defined as

$$\tilde{\psi} = \dot{\psi} - \dot{\psi}_d, \quad (7.6)$$

and the sliding variable is defined by

$$\sigma(\dot{\psi}, t) = \tilde{\psi} + \gamma \int_0^t \tilde{\psi} d\tau. \quad (7.7)$$

As in the case of wheel slip control,  $\gamma$  is a strictly positive tuning parameter (see Appendix A), and the expression  $\sigma(\dot{\psi}, t)$  is replaced by  $\sigma$  for reasons of readability. If the vehicle yaw rate is forced to a constant value  $\dot{\psi}_d$ , this leads to

$$\begin{aligned} \dot{\sigma} \stackrel{!}{=} 0 = & -\frac{c_{\alpha,R} l_R^2 + c_{\alpha,F} l_F^2}{J_z v} \dot{\psi} + \frac{c_{\alpha,R} l_R - c_{\alpha,F} l_F}{J_z} \beta + \frac{c_{\alpha,F} l_F}{J_z} \delta + \\ & + \frac{1}{J_z} \hat{T}_z + \gamma (\dot{\psi} - \dot{\psi}_d). \end{aligned} \quad (7.8)$$

For nominal parameter values, the equivalent control torque  $\hat{T}_z$  results in

$$\hat{T}_z = \left( \frac{c_{\alpha,R} l_R^2 + c_{\alpha,F} l_F^2}{v} - \gamma J_z \right) \dot{\psi} + (c_{\alpha,F} l_F - c_{\alpha,R} l_R) \beta - c_{\alpha,F} l_F \delta + \gamma J_z \dot{\psi}_d. \quad (7.9)$$

An additional control input

$$T_{z,\text{sw}} = -K_z \text{sat} \left( \frac{\sigma}{\phi} \right) \quad (7.10)$$

is required to influence the dynamics of  $\sigma$  and to cope with plant uncertainties (see Appendix A). The sliding surface is rendered invariant if  $K_z$  is chosen as

$$K_z > |(c_{\alpha,\text{R}} l_{\text{R}} - c_{\alpha,\text{F}} l_{\text{F}}) \beta_{\text{max}}|, \quad (7.11)$$

where  $\beta_{\text{max}}$  defines the maximum achievable sideslip angle. Using (7.9) and (7.10) leads to the yaw rate controller

$$\begin{aligned} T_z &= \hat{T}_z + T_{z,\text{sw}} = \left( \frac{c_{\alpha,\text{R}} l_{\text{R}}^2 + c_{\alpha,\text{F}} l_{\text{F}}^2}{v} - \gamma J_z \right) \dot{\psi} + (c_{\alpha,\text{F}} l_{\text{F}} - c_{\alpha,\text{R}} l_{\text{R}}) \beta - \\ &- c_{\alpha,\text{F}} l_{\text{F}} \delta + \gamma J_z \dot{\psi}_{\text{d}} - K_z \text{sat} \left( \frac{\sigma}{\phi} \right). \end{aligned} \quad (7.12)$$

As long as

$$|\tilde{\psi}| < \Delta\tilde{\psi}, \quad (7.13)$$

the yaw rate controller is in its “monitoring mode”, where  $T_z = 0$ .  $\Delta\tilde{\psi}$  defines the yaw rate error threshold to avoid unnecessary controller interventions. In order to make the switch-off of the controller less recognizable for the passengers, the slew rate of the yaw torque  $T_z$  is limited. In addition, the output of the integrator in (7.7) is forced to zero when the controller remains in the monitoring mode.

The identifiers  $\sigma$ ,  $\gamma$  and  $\phi$  are labeled the same as in Chapter 6 as they are common for SM controller design. However, from the relation to their control purpose, it is clear that they have different meanings compared to the ones used in Chapter 6. The same holds true for the  $\sigma$ ,  $\gamma$  and  $\phi$  used for sideslip angle control.

## 7.2.2 Torque coordination

Figure 7.2 depicts the yaw rate control loop when the SM controller (7.12) is applied. Considering the output torque  $T_z$  of the yaw rate controller and the input torques  $T_{\text{td,d}}$  and  $T_{\text{brk,d}}$  of the HAS, it is clear that  $T_z$  must be converted into appropriate actuator torques. Thus, the reference values  $T'_{\text{td,d}}$  and  $T'_{\text{brk,d}}$  determined by the energy management have to be adapted such that  $T_z$  is established. For this purpose, a torque coordinator is utilized. In addition, the tires yaw potentials must be analyzed, which is done in the vehicle state estimator shown in Figure 7.2.

### Vehicle state estimation / Yaw potential analysis

The tire forces influence the yaw motion, as shown in Section 3.5.2. The tire forces change depending on such factors as the tire load force  $F_z$ , the wheel slideslip angle  $\alpha$  and the wheel slip  $\lambda$  (see Section 3.1). By applying the structure shown in Figure 7.3, the tire forces and their influence on the yaw motion can be calculated. With the help of the measured

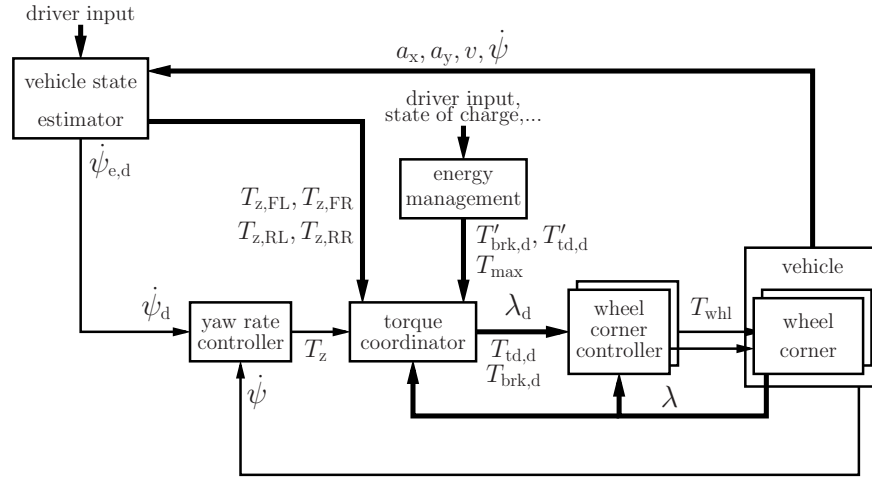


Figure 7.2: VDC yaw rate control loop

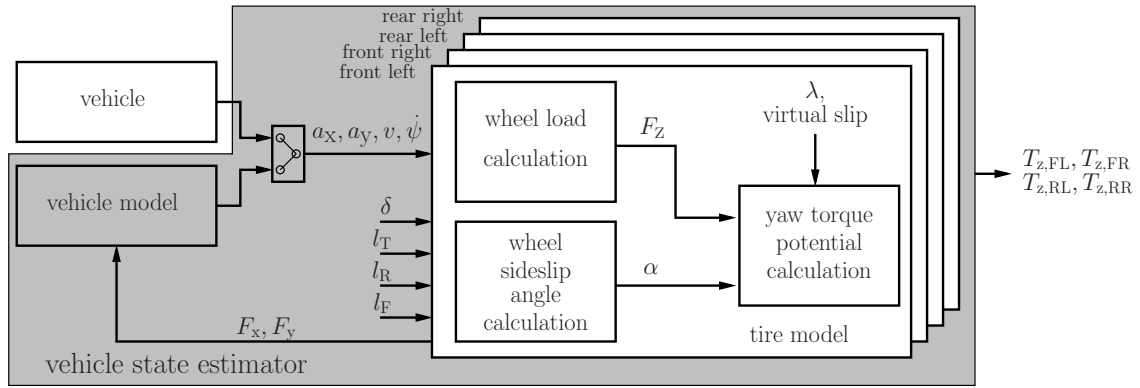


Figure 7.3: Estimation of yaw torque potential

vehicle signals or a two-track vehicle model and a tire model it is possible to estimate the tire forces  $F_x$  and  $F_y$ . Once these values are known, the yaw torque generated by the wheels can be calculated, for example by applying (3.52). The achievable yaw torques are denoted as yaw torque potentials  $T_{z,FL}$ ,  $T_{z,FR}$ ,  $T_{z,RL}$  and  $T_{z,RR}$  (see Figure 7.2).

To provide an example, Figure 7.4 shows the yaw torque potentials of the wheels for dry road conditions during a steering wheel step driving maneuver. The vehicle is moving along a straight line, and at  $t = 1$ s a steering step (left curve) is performed. If it is assumed that the vehicle is driving at constant speed and the wheel slip  $\lambda = 0$ . The yaw torque is only established by the lateral tire forces  $F_y$ . Each wheel generates a positive yaw torque while the vehicle is turning (see bold lines in Figure 7.4). As the conventions established in [Deu94] are used, a positive yaw torque means that the vehicle is forced to turn counter-clock wise.

Instead of solely concentrating on the tire forces  $F_y$ , the tire’s yaw potential can be estimated for different wheel slips as well. Now, the tire force  $F_x$  can be used for yaw torque generation, too. As an example, Figure 7.4 shows the yaw torques when applying

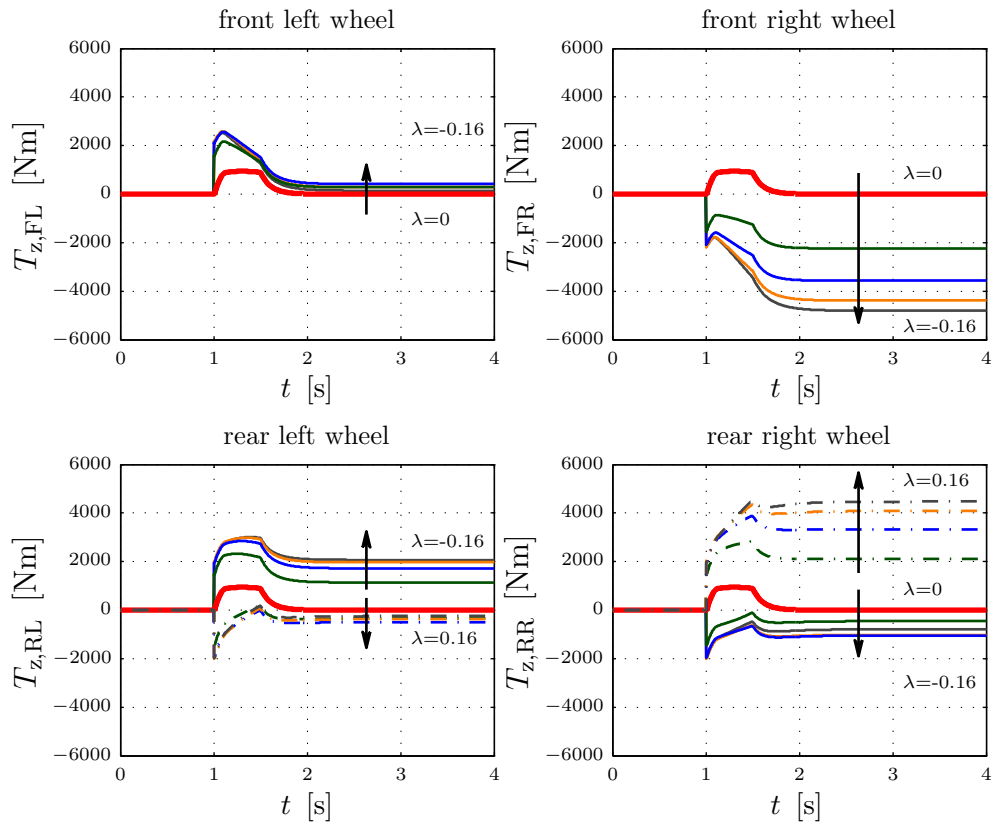


Figure 7.4: Yaw torque potential

different wheel slips.

For the wheels of the front axle, only the results for negative wheel slips are shown. This is reasonable, as the front axle is only equipped with friction brakes. As a consequence, positive wheel slips cannot be achieved. Braking the front left wheel causes a low positive yaw torque. This means that braking this wheel helps the vehicle to increase its yaw motion. On the other hand, braking the front right wheel generates a high negative yaw torque. The brake interventions on the front right wheel can be applied to reduce vehicle oversteering. This damps the yaw dynamics and therefore counteracts the yaw motion generated by the left wheel.

Figure 7.4 shows the results for negative and positive wheel slips for the rear axle wheels, as the HAS enables acceleration or deceleration of the wheel. It is evident that each wheel might generate positive and negative torques to influence the vehicle's yaw motion.

Instead of applying the wheel slip in the real vehicle, it is possible to apply “virtual wheel slips” to the tire model in Figure 7.3 as well. The resulting yaw torque potentials can be calculated without influencing the vehicle motion. This makes it possible to estimate the vehicle reaction in advance of controller intervention. These estimates can be utilized to select the wheels where the propulsion torques should be adapted. Furthermore, the desired wheel slips  $\lambda_d$  can be calculated such that the vehicle turns in a desired manner.

The yaw torque analysis explained above can be used in any driving situation. In [Wag06], this estimation method is applied for other control systems. When the vehicle is performing a maneuver, the wheel potential can be calculated online. Although the tire's yaw potentials greatly depend on  $\mu$ , the tendency is still the same.

### Torque coordinator / actuator selection

As with the combined actuator control (see Chapter 5), the actuator selection here is based on a daisy chain approach [Wil02]. Within each ECU execution cycle, the steps shown in the flow chart in Figure 7.5 are computed.

When no yaw motion control action is required ( $T_z = 0$ ), the intended HAS actuator torques are calculated via

$$T_{td,d} = \frac{T'_{td,d}}{2} \quad \text{and} \quad T_{brk,d} = \frac{T'_{brk,d}}{2}. \quad (7.14)$$

The energy management reference values  $T'_{td,d}$  and  $T'_{brk,d}$  are equal for the rear axle wheel corners. Using both HAS in the same manner ensures that no unintended yaw torques occur and that the two HAS are deployed equally. Only “Action 1” in Figure 7.5 is performed.

When yaw torques  $T_z$  have to be introduced by the HAS, the wheel torques need to be adapted. Based on Figure 3.10, it follows for the rear axle that

$$T_z = (F_{x,RR} - F_{x,RL}) \frac{l_T}{2} - (F_{y,RL} + F_{y,RR}) l_R. \quad (7.15)$$

To establish  $F_{x,RL}$ ,  $F_{y,RL}$  and  $F_{x,RR}$ ,  $F_{y,RR}$ , each HAS controller receives its dedicated feed-forward control torques  $T_{td,d}$ ,  $T_{brk,d}$  and its desired wheel slip  $\lambda_d$ . A further breakdown

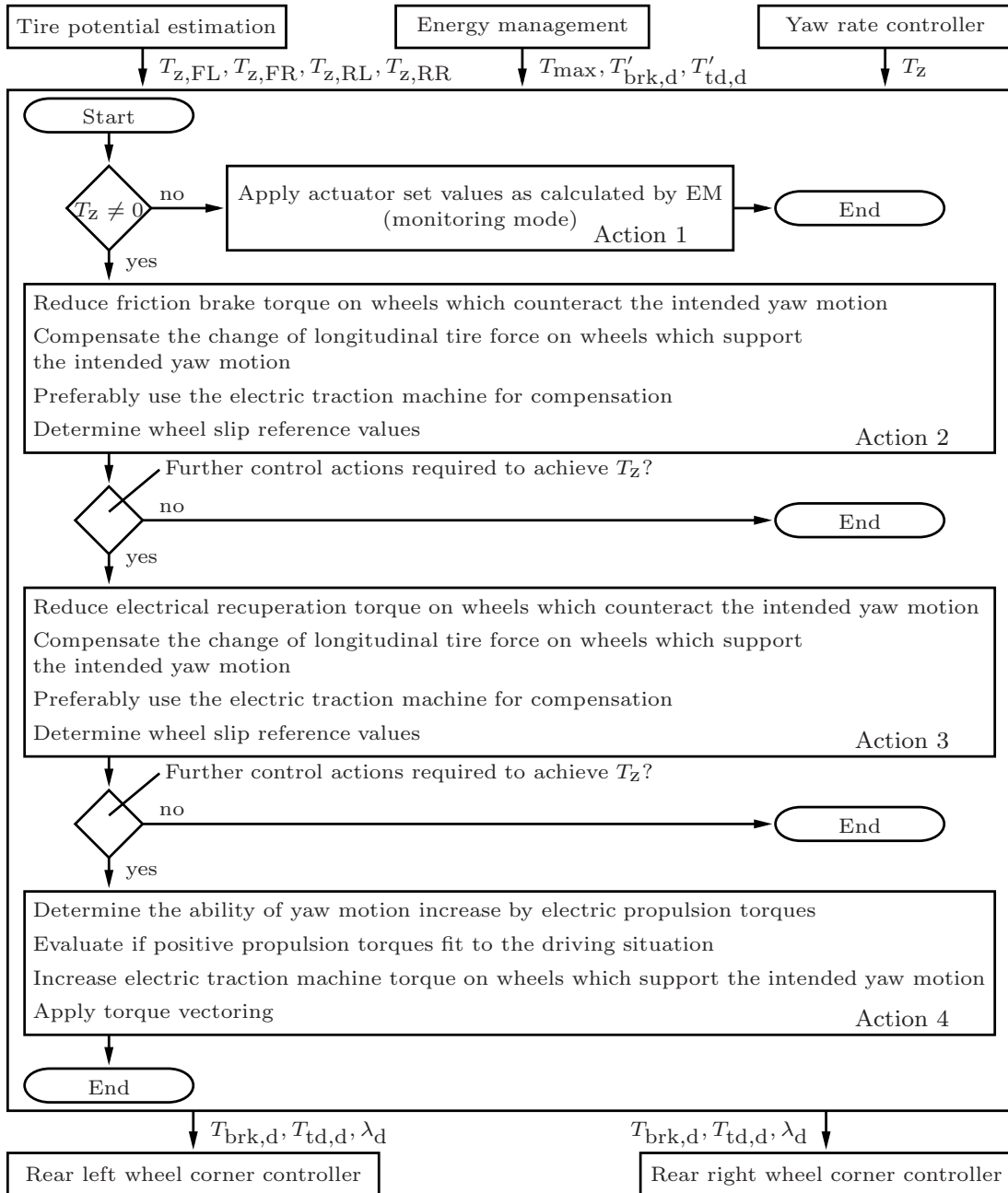


Figure 7.5: Torque coordinator

into signals for each wheel corner is omitted in order to ensure better readability.

Calculating the corresponding actuator torques  $T_{td,d}$  and  $T_{brk,d}$  leads to the challenge of solving a non-unique problem, which is often done by means of optimization [Ore06]. Instead of solving an optimization problem, a practical approach is applied here. The determination of the actuator torques is based on the potentials  $T_{z,ij}$  calculated for the previously mentioned “virtual wheel slips”. The HAS actuators are clustered according to their effects on the vehicle motion, such as

- “support intended yaw motion”
- “counteract intended yaw motion”.

Furthermore, the actuators that can be applied for yaw motion control are classified based to their functions, such as

- “decelerate wheel by means of friction brake”
- “decelerate wheel by means of recuperation”
- “accelerate wheel”.

This clustering creates different sets of possibilities for control interventions. The task of the torque coordinator then is to select the most effective and least energy-consuming actuators to achieve the desired yaw motion.

Depending on the actual wheel slip  $\lambda$  and the maximum machine torque  $T_{max}$ , one or more of the previously clustered HAS actuators can be selected. As shown in “Action 2” in Figure 7.5, the wheel torques that counteract the intended yaw motion are adapted first. For maximum efficiency, this is accomplished by reducing the friction brake torques. Preferably, changes in the longitudinal tire forces are compensated for by the electric traction machines (i.e. increase recuperation). This compensation takes place on the wheels which support the establishment of the intended yaw motion.

If the desired yaw motion cannot be achieved via the activities summarized in “Action 2”, the activities combined in “Action 3” are required. The recuperation torques on the wheels which counteract the intended yaw motion have to be reduced. If possible, the reduction of recuperation torque is compensated for by an increase of recuperation torque at the other wheels. Otherwise, the friction brake may be used. The previously established classification provides important information about the possible means of compensation.

When applying an HAS, it is also possible to generate yaw torques by accelerating a single wheel. As stated in “Action 4”, this option can be used when the driving situation allows for an increase of the wheel torque. In conventional vehicles, this is typically known as *torque vectoring* or *active torque distribution* [HS09, YTS<sup>+</sup>10, Zeh07] and results in a more sporty driving behavior. The relevant literature describes many torque vectoring concepts that are based on mechanical solutions, such as [Bic04]. The torque vectoring shown in this thesis is based on electronically controlled actuators where the two sides of the vehicle are completely mechanically decoupled. This enables an energy-efficient cornering. Recuperated energy from one HAS can be transferred directly to the HAS on the other side of the vehicle. Especially in emergency cases (e.g. when a high positive yaw torque is required), both sides can be used to generate high torques.

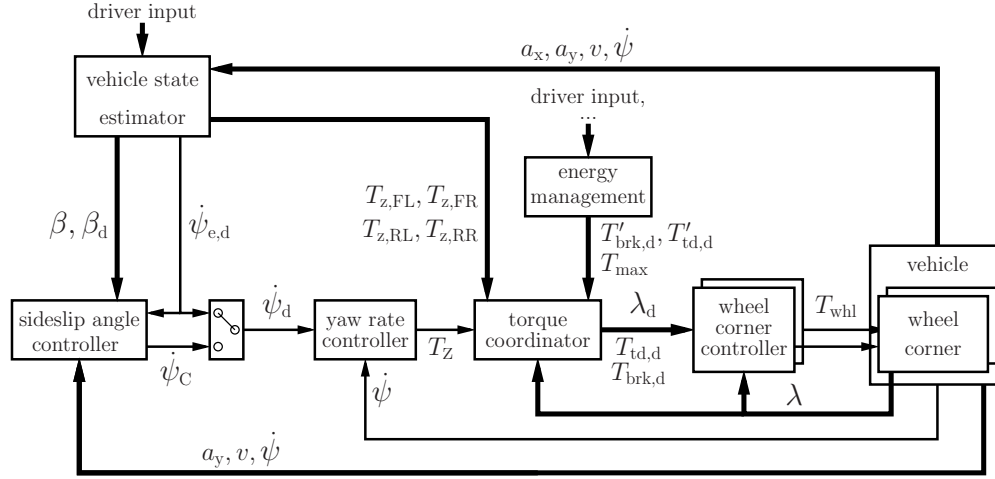


Figure 7.6: VDC sideslip angle control loop

Depending on the application of “Actions 1-4”, the actuator torques (7.14) are modified such that

$$T_{td,d} = T_{td,d} (T'_{td,d}, T_z, T_{max}, T_{z,ij}, \lambda) \quad \forall i \in \{F,R\}, j \in \{L,R\} \quad (7.16)$$

and

$$T_{brk,d} = T_{brk,d} (T'_{brk,d}, T_z, T_{z,ij}, \lambda) \quad \forall i \in \{F,R\}, j \in \{L,R\}. \quad (7.17)$$

### 7.2.3 Sliding mode vehicle sideslip angle control

The previous sections explained the calculation of the yaw torque  $T_z$  and its relation to the wheel torques. As previously mentioned, it is sometimes necessary to adapt the reference yaw rate due to sideslip angle limitations. This can be achieved with the help of a sideslip angle controller, as depicted in Figure 7.6.

For sideslip angle control, the error  $\tilde{\beta}$  is defined as

$$\tilde{\beta} = \beta - \beta_d, \quad (7.18)$$

and the differential equation

$$\dot{\beta} = \left( \frac{c_{\alpha,R} l_R - c_{\alpha,F} l_F}{m v^2} - 1 \right) \dot{\psi} - \frac{c_{\alpha,F} + c_{\alpha,R}}{m v} \beta + \frac{c_{\alpha,F}}{m v} \delta \quad (7.19)$$

is used as a model for the sideslip angle (see Equation (3.47)). In this equation, the steering angle  $\delta$  which results from the input from the driver, while  $\dot{\psi}$  represents the actuating signal for sideslip angle control. As the plant is uncertain as well, the control of the sideslip angle is realized by means of sliding mode control. The sliding variable is defined as

$$\sigma = \tilde{\beta} + \gamma \int_0^t \tilde{\beta} d\tau. \quad (7.20)$$

The weighting parameter  $\gamma$  is strictly positive, and the desired sideslip angle  $\beta_d$  is assumed to be constant. As the sideslip angle typically changes more slowly than the yaw rate, the inner control loop for the yaw rate control is assumed to be ideal.

For nominal plant parameters, the equivalent yaw rate

$$\hat{\psi} = \frac{((c_{\alpha,F} + c_{\alpha,R})\beta - c_{\alpha,F}\delta - \gamma(\beta - \beta_d)mv)v}{c_{\alpha,R}l_R - c_{\alpha,F}l_F - mv^2} \quad (7.21)$$

keeps  $\sigma$  at a constant value. In order to steer  $\sigma$  to zero, the yaw rate  $\dot{\psi}_C$  is a linear combination of the equivalent yaw rate and a discontinuous part  $\dot{\psi}_{sw}$ , that is:

$$\dot{\psi}_C = \hat{\psi} + \dot{\psi}_{sw}. \quad (7.22)$$

For practical application reasons (i.e. to keep the workload for the actuators within reasonable bounds), the sign-function in the discontinuous part is approximated by a saturation-function, which yields

$$\dot{\psi}_{sw} = -K_\beta \text{sat}\left(\frac{\sigma}{\phi}\right). \quad (7.23)$$

From (7.19), the model uncertainties resulting from the sideslip angle can be estimated and result in

$$K_\beta > \left| \frac{c_{\alpha,F} + c_{\alpha,R}}{c_{\alpha,R}l_R - c_{\alpha,F}l_F - mv^2} v \beta_{\max} \right|. \quad (7.24)$$

The maximum achievable sideslip angle is denoted by  $\beta_{\max}$ .

A strictly positive  $\Delta\beta$  is introduced in order to avoid the immediate activation of the sideslip angle controller in the case of low control errors. Sideslip angle control is entered if

$$|\beta| \geq |\beta_d| + \Delta\beta. \quad (7.25)$$

During the control of the sideslip angle, the target yaw rate  $\dot{\psi}_{e,d}$  is replaced by the output  $\dot{\psi}_C$  of the sideslip angle controller:

$$\dot{\psi}_d = \begin{cases} \dot{\psi}_{e,d}, & \text{during yaw rate control} \\ \dot{\psi}_C, & \text{during sideslip angle control} \end{cases} \quad (7.26)$$

The transition from yaw rate control to sideslip angle control can be achieved by switching from  $\dot{\psi}_d = \dot{\psi}_{e,d}$  to  $\dot{\psi}_d = \dot{\psi}_C$ . The reverse action requires a modification of (7.25). In order to realize a seamless transition from sideslip angle control to yaw rate control, the logical relation

$$\left( (|\beta| < |\beta_d|) \wedge \left( (|\dot{\psi}| - |\dot{\psi}_{e,d}|) < \Delta\dot{\psi} \right) \right) = 1 \quad (7.27)$$

is used.  $\Delta\dot{\psi}$  is a tuning parameter, that defines the maximum yaw rate step that is allowed to occur when the yaw motion controller switches from the sideslip angle control to the yaw rate control. As long as (7.27) is not valid, the control of the sideslip angle remains active. A switch to the yaw rate control is performed when (7.27) is fulfilled. During yaw rate control, the integration of  $\tilde{\beta}$  is stopped, and the integrator output value (7.20) and  $\sigma$  are forced to be zero.

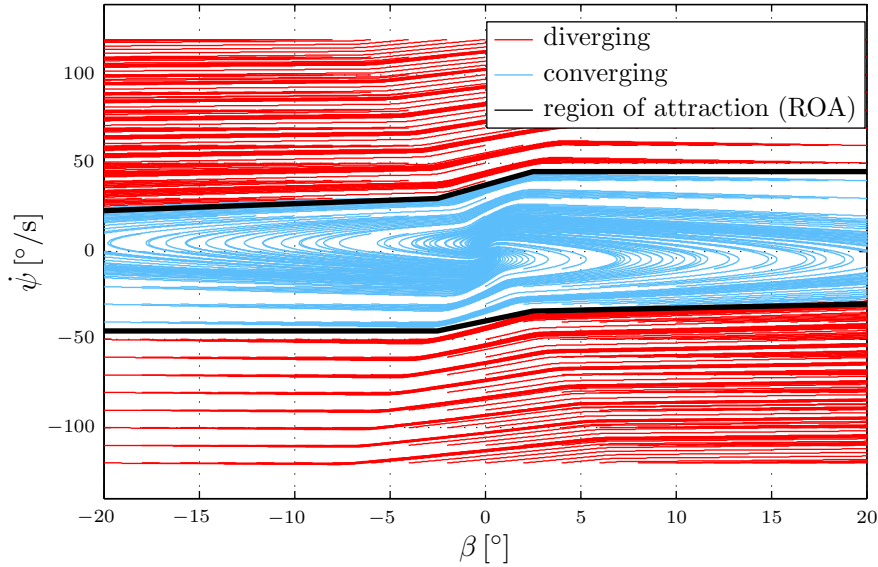


Figure 7.7: Vehicle yaw motion phase plane (uncontrolled vehicle)

### 7.3 Performance analysis of the vehicle yaw motion controller

The relevant literature [SL99] states that the behavior of systems of 1<sup>st</sup> or 2<sup>nd</sup> order can be analyzed by means of phase portraits. The intention of this graphical study is to determine the stability behavior of equilibrium points of differential equations. In the case of asymptotically stable equilibrium points, it is also possible to display their regions of attraction (ROA). Starting from a set of initial conditions, the phase plane trajectories represent the solution of the differential equations.

The performance of the proposed vehicle motion controller is tested by means of the nonlinear two-track vehicle model described in Section 3.5.2. The desired equilibrium point is the origin of the  $\psi - \beta$ -phase plane, which represents the straight run of a vehicle.

Figure 7.7 shows the phase portrait of an uncontrolled vehicle at constant speed. In contrast to the approaches in [IKYK94, Sma00] the driving maneuver is carried out at low- $\mu$  conditions. Especially at such conditions, the yaw motion control interactions are of great interest for the driver. To eliminate the influence of the driver, it is assumed that the wheel steering angle  $\delta$  is zero. The converging or diverging behavior is shown for different initial points. Depending on the initial conditions chosen, it is possible that the vehicle stabilizes itself to a straight run drive. The region of attraction is highlighted in Figure 7.7. This region shrinks when the vehicle is driven at higher speeds. For the driver, it becomes more and more challenging to stabilize the vehicle. As a consequence, an effective control system is required.

In order to emphasize the enlargement of the region of attraction, the proposed VDC is utilized with the same maneuver. Figure 7.8 shows the simulation results. For a better comparison, the ROA of the uncontrolled vehicle is displayed as well. Additionally, the

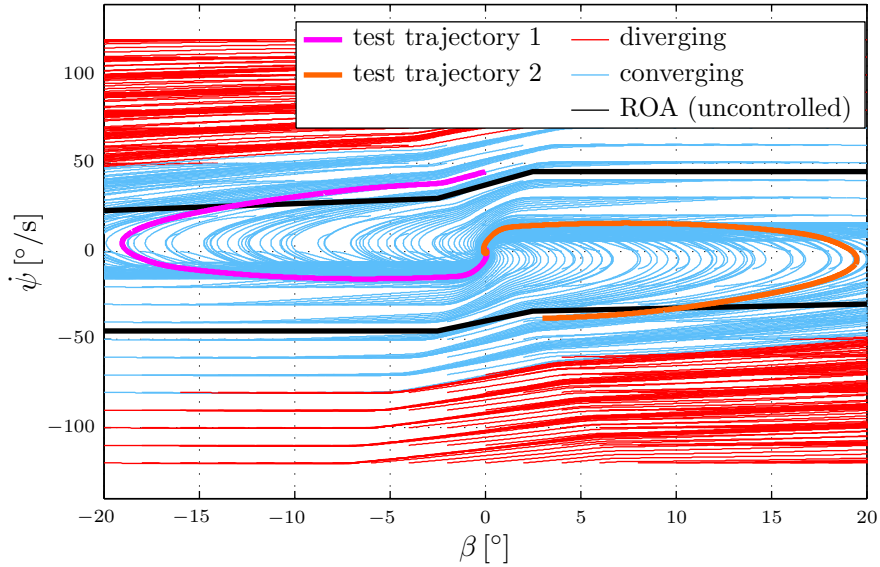


Figure 7.8: Vehicle yaw motion phase plane (controlled vehicle)

trajectories for two more arbitrarily chosen initial points are highlighted.

In contrast to the state feedback controller shown in [VHG10], the proposed yaw motion controller shows integrating behavior, which is used to drive the control error to zero. The application of the SM controllers introduces two additional state variables. As a 4-dimensional plot of the system trajectories would not be diagnostically conclusive, only  $\dot{\psi}$  and  $\beta$  are shown. The equilibrium point is reached when all four state variables end at the origin. Solely displaying the state variables  $\dot{\psi}$  and  $\beta$  could therefore be misleading (e.g. if the plotted variables converge while the remaining variables do not). In order to verify the attractiveness of the equilibrium point, Figure 7.9 shows all four state variables for the test trajectories. It can be seen that they converge at the origin. This happens for all trajectories which are highlighted as converging in Figure 7.8. When Equations (7.13) and (7.27) are invalid, the sideslip angle control is active. As soon as (7.27) is valid, the sideslip angle control is switched off, and the yaw rate controller influences the vehicle motion. When both are valid, the yaw rate controller is switched off, too. The trajectory is close enough to the equilibrium point that the vehicle finally enters the equilibrium point without VDC control action.

The proposed control concept enlarges the region of attraction (see Figure 7.8). This implies that the VDC supports the driver in stabilizing the vehicle.

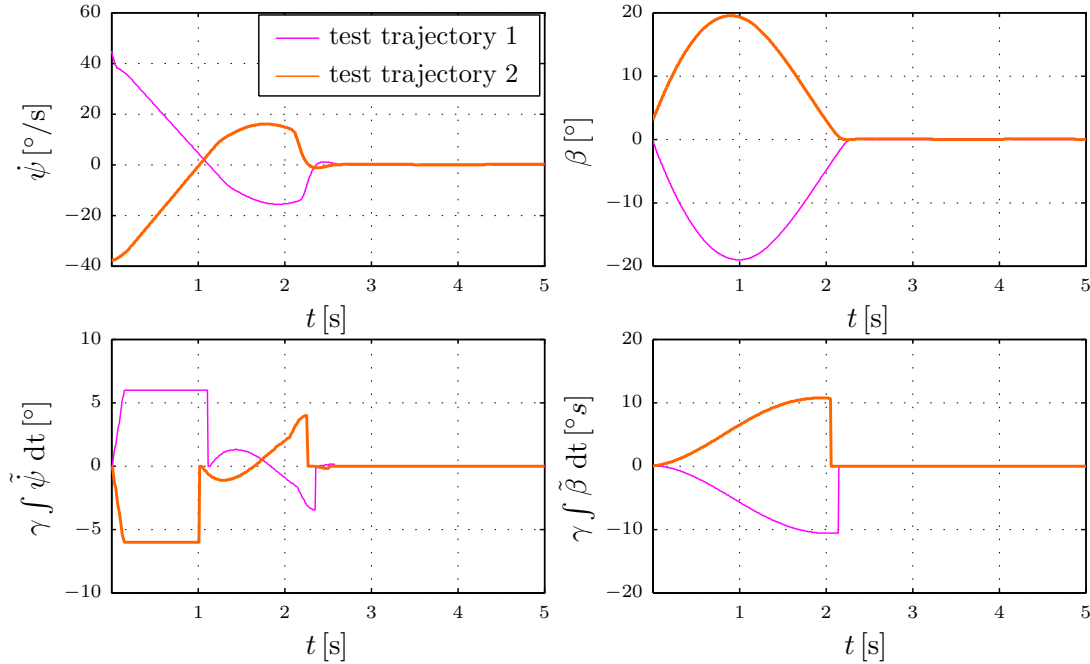


Figure 7.9: VDC system states during yaw motion control for different initial states

## 7.4 Vehicle motion control during standardized test maneuvers

In Section 7.3, the potential of the yaw motion controller is analyzed by means of phase planes where the region of attraction can be approximated. Since the phase plane representation does not consider the link to the required time for vehicle stabilization, the next task is to test the controller with the aid of standardized driving maneuvers.

This section provides an overview of how vehicle dynamics can be improved when the proposed VDC is applied. The performance of a vehicle equipped with ESC using friction brakes is compared to an EV utilizing the proposed VDC with HAS control.

To minimize the driver's influence, most maneuvers are performed open loop. Only the emergency braking under split- $\mu$  conditions and the VDA lane change maneuver are tested closed loop. High- $\mu$  refers to  $\mu=1$ , while low- $\mu$  refers to  $\mu=0.2$ .

### 7.4.1 Emergency braking

Chapter 6 showed the performance of the wheel slip controller. The braking maneuvers are performed without VDC interventions. In contrast to the simulations in Section 6.2, the interventions of the yaw motion controller are now required. Table 7.1 summarizes the performance criteria achieved for emergency braking. Figure 7.10 displays the control performance of the VDC while braking under low- $\mu$  conditions. At the beginning of the deceleration maneuver, it is not possible for the electrical system to provide the requested wheel torques. A combined control of traction machines and friction brakes is required. Both actuators are controlled such that the resulting wheel slips are limited to the desired

reference values.

As can be seen from Figure 7.10, an unintended yaw motion acts on the vehicle. To fulfill the driver's intention (i.e. to keep the vehicle on a straight run), a torque  $T_z$  must be generated. Due to the arising yaw motion, the straight run can be ensured without reducing recuperation. The yaw motion can be corrected by only reducing the rear left brake pressure and keeping the machine torque almost constant. The rear right actuators remain unchanged to keep the deceleration performance on a high level. After correcting the yaw motion, the combined control is continued. At lower speeds, the deceleration can be completely achieved with the traction machines. This leads to a brake distance reduction of approximately 2% compared to the ESC.

In contrast to the low- $\mu$  emergency braking, no yaw motion control intervention is required for the high- $\mu$  emergency braking. Therefore, the simulation results are not shown. Table 7.1 summarizes the results achieved. In terms of braking distance, it can be concluded that a decrease of approximately 5% is possible.

Another interesting maneuver is emergency braking under split- $\mu$  conditions. Figure 7.11 shows the simulation results. At the beginning of the maneuver, the HAS signals have nearly the same characteristic as in the low- $\mu$  case. A combined HAS control is required as well. On the right-hand side of the vehicle, a higher traction force potential is available than on the left-hand side. On the left-hand side of the vehicle (low- $\mu$  side), it is necessary to limit the propulsion torques, as the desired wheel slip is exceeded. The friction torque and the recuperation torque on the right-hand side are established with a certain slew rate [Web05]. When the traction force difference reaches a certain level, a yaw motion control action is required. During this driving maneuver, the yaw rate and the sideslip angle rise very quickly. To correct the yaw motion, a positive yaw torque  $T_z$  is needed. The propulsion torques on the high- $\mu$  side are reduced such that the vehicle motion is stabilized, while the low- $\mu$  side of the vehicle always maintains the highest possible deceleration. On average, the braking distance can be reduced by about 3%.

#### 7.4.2 Steering wheel step maneuver

A very interesting benchmark maneuver for yaw motion control applications is the steering wheel step maneuver. The steering step is performed according to [Deu89]. The velocity of the steering wheel angle is defined as  $\dot{\delta}_D = 300^\circ/s$ , and the steering wheel amplitude is fixed to  $\delta_D = 90^\circ$ . For both high- $\mu$  and low- $\mu$  conditions, the vehicle responses of ESC and VDC are approximately the same (see Figure 7.12). In addition, for the the low- $\mu$  conditions two variants of VDC control are shown. The VDC which uses  $a_y$  for the reference value calculation can achieve a secure driving. The VDC without considering  $a_y$  results in a spinning vehicle (see Section 7.1).

Figure 7.13 shows the yaw motion signals originating from a steering step under low- $\mu$  conditions in detail. As recommended in [Deu89], the response of the yaw rate and the sideslip angle are analyzed. With reference to Table 7.2, it can be confirmed that the response times are nearly the same for both configurations. The response times listed in Table 7.2 are defined as the time difference between the moment where  $\delta_D$  reaches 50% of its maximum value and the moment where the yaw signals reach 90% or 100%, respectively, of their maximum value. Comparing the response times of the sideslip angle

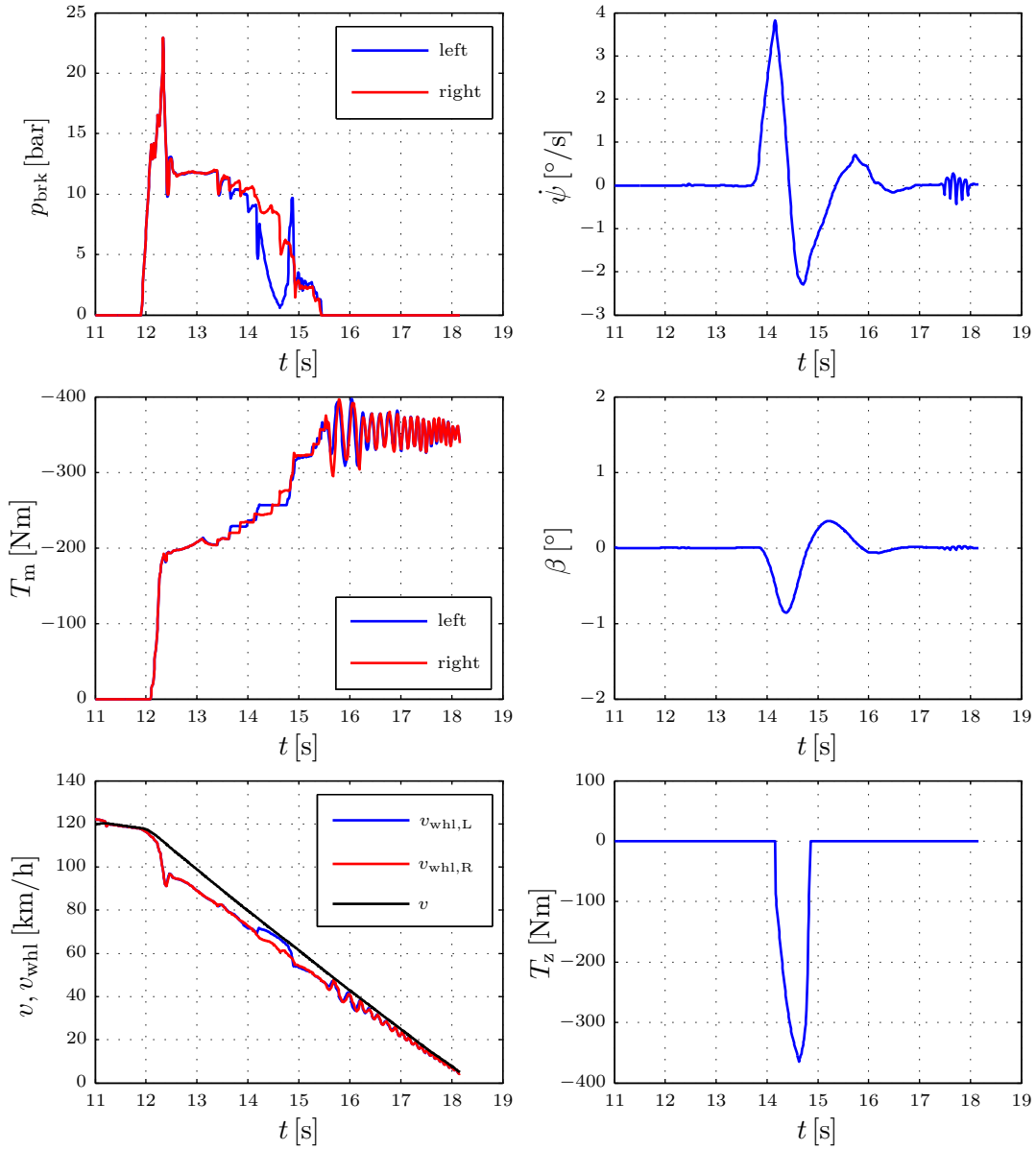


Figure 7.10: VDC braking under low- $\mu$  conditions. Both HAS actuators are utilized for vehicle deceleration as the traction machine cannot provide sufficient propulsion torque. The friction brake torque is reduced as soon as the recuperation torque increases. When the vehicle shows an unintended yaw motion, the friction brake torque on the left-hand side is reduced such that  $T_z \neq 0$ . The vehicle yaw motion is corrected without reducing recuperation.

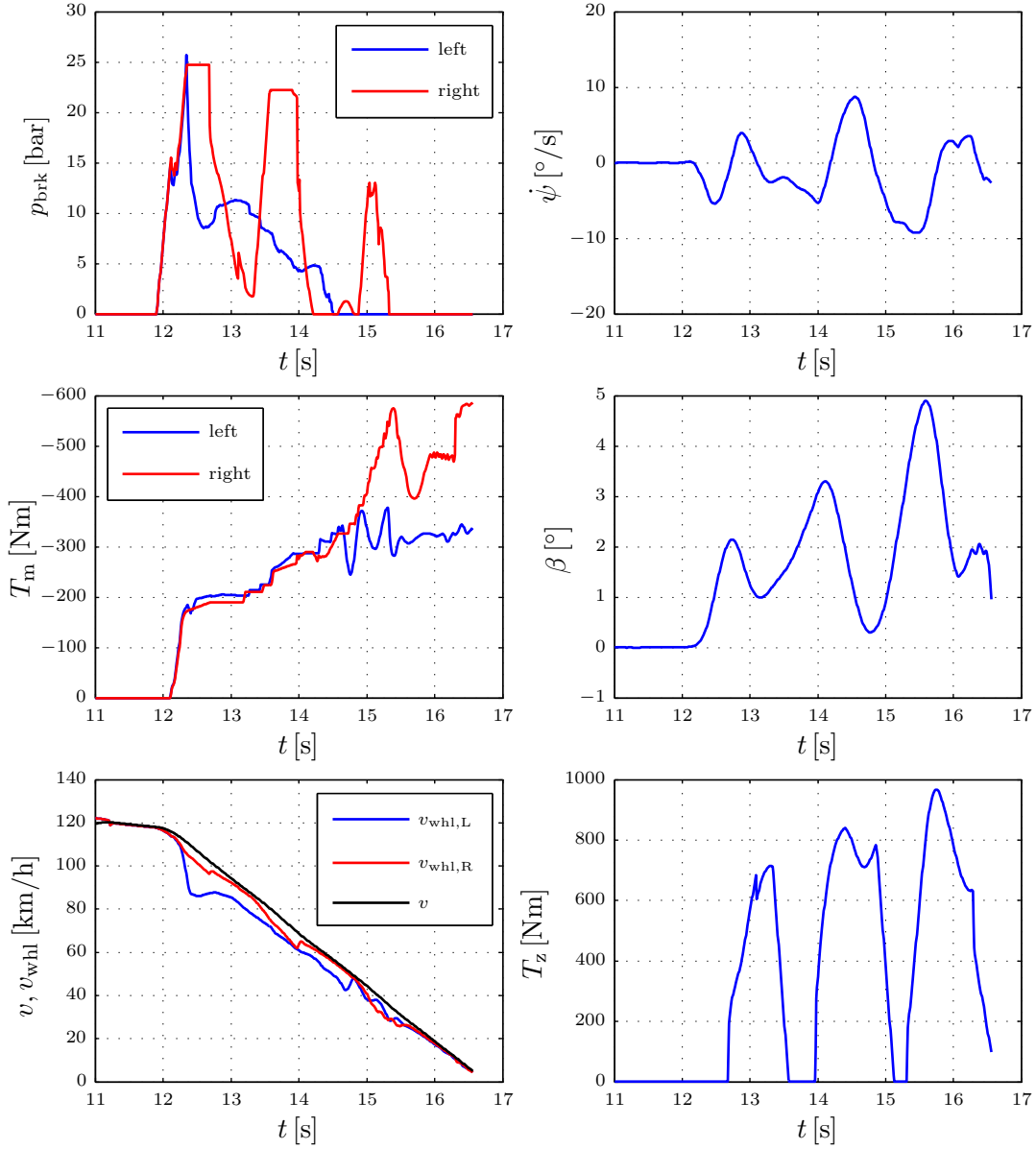


Figure 7.11: VDC braking under split- $\mu$  conditions. As the right-hand side of the vehicle is at high- $\mu$ , the wheel torque can achieve higher absolute values than the left-hand side. This causes an introduction of unintended yaw motion. To keep the vehicle on a straight run, the friction brake torque is reduced based on  $T_z$ . Yaw motion control and a good braking performance can be achieved, as well as energy recuperation.

<i>Evaluation criterion</i>	<i>ESC</i>	<i>VDC</i>
low- $\mu$ emergency braking		
braking distance	108.5m	106.4m
maximum lateral displacement	0.4m	0.5m
maximum yaw rate amplitude	1.9°/s	3.9°/s
maximum sideslip angle amplitude	0.3°	0.9°
high- $\mu$ emergency braking		
braking distance	65m	61.5m
maximum lateral displacement	0.2m	0.4m
maximum yaw rate amplitude	1.3°/s	2.6°/s
maximum sideslip angle amplitude	0.3°	0.4°
split- $\mu$ emergency braking		
braking distance	84.6m	82.1m
maximum lateral displacement	0.2m	0.4m
maximum yaw rate amplitude	3.3°/s	9.3°/s
maximum sideslip angle amplitude	2.3°	4.9°

Table 7.1: Simulation results for emergency braking

may suggest that the VDC supports the fast setup of a sideslip angle. However, this is not correct, as the maximum value of the sideslip angle with VDC is lower than the maximum value achieved with the ESC.

When the steering wheel angle step is performed, the VDC yaw motion controller enters the yaw rate control, followed by the control of the sideslip angle. As can be seen from Figure 7.13, the controller calculates a negative yaw torque  $T_z$ . This means that the VDC actively damps the excitation of excessively high yaw dynamics. Based on to the determined correction torque, the traction machine torques are adapted individually. To establish a negative yaw torque  $T_z$ , the propulsion torque on the rear left wheel is higher than on the rear right wheel. The friction brakes are not accessed. By applying  $T_z$ , it is possible to control the yaw rate and the vehicle's sideslip angle. As outlined in [FLH13], the handling behavior of the vehicle can be improved, and the application of friction brake interventions can be reduced.

### 7.4.3 Power lift-off

The third test maneuver investigated the effects of a sudden initiation of a power-off condition during a turn. To do so, the vehicle is accelerated on a track with a constant radius of 100m. As specified in [Int06], the vehicle is accelerated until a lateral acceleration of  $a_y = 6.5\text{m/s}^2$  is achieved. This is performed closed loop. From  $t = 19.5\text{s}$  onwards, the steering angle is kept constant, and the accelerator pedal is released immediately. When the pedal is released, the existing values for  $a_y$ ,  $\dot{\psi}$  and  $\beta$  are noted as comparative values. They are also displayed in Figure 7.14 for analyzing purposes. Due to the load shift from the rear axle to the front axle, the vehicle tends to decrease its turning radius instead of following the target trajectory. With the help of the traction machines, it is possible to

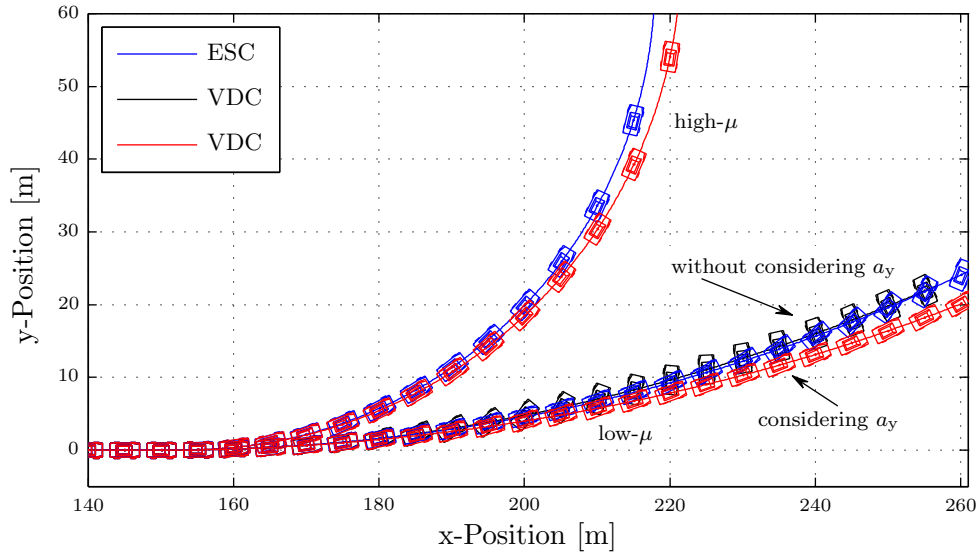


Figure 7.12: Steering wheel step (bird's-eye view). For high- $\mu$ , nearly the same cornering performance for ESC and VDC is observable. At low- $\mu$ , the determination of  $\dot{\psi}_d$  requires the consideration of  $a_y$  in order to prevent the vehicle from spinning. Although the VDC reduces sideslip angle, it causes a slightly increased cornering radius.

<i>Evaluation criterion</i>	<i>ESC</i>	<i>VDC</i>
maximum yaw rate	14.6°/s	13°/s
minimum sideslip angle	-3.4°	-2°
yaw rate response time (90%)	0.15s	0.13s
yaw rate response time (100%)	0.26s	0.23s
yaw rate overshoot	74%	57%
sideslip angle response (90%)	0.71s	0.47s
sideslip angle response (100%)	1.03s	0.63s
sideslip angle overshoot	124%	34%

Table 7.2: Simulation results for steering wheel step

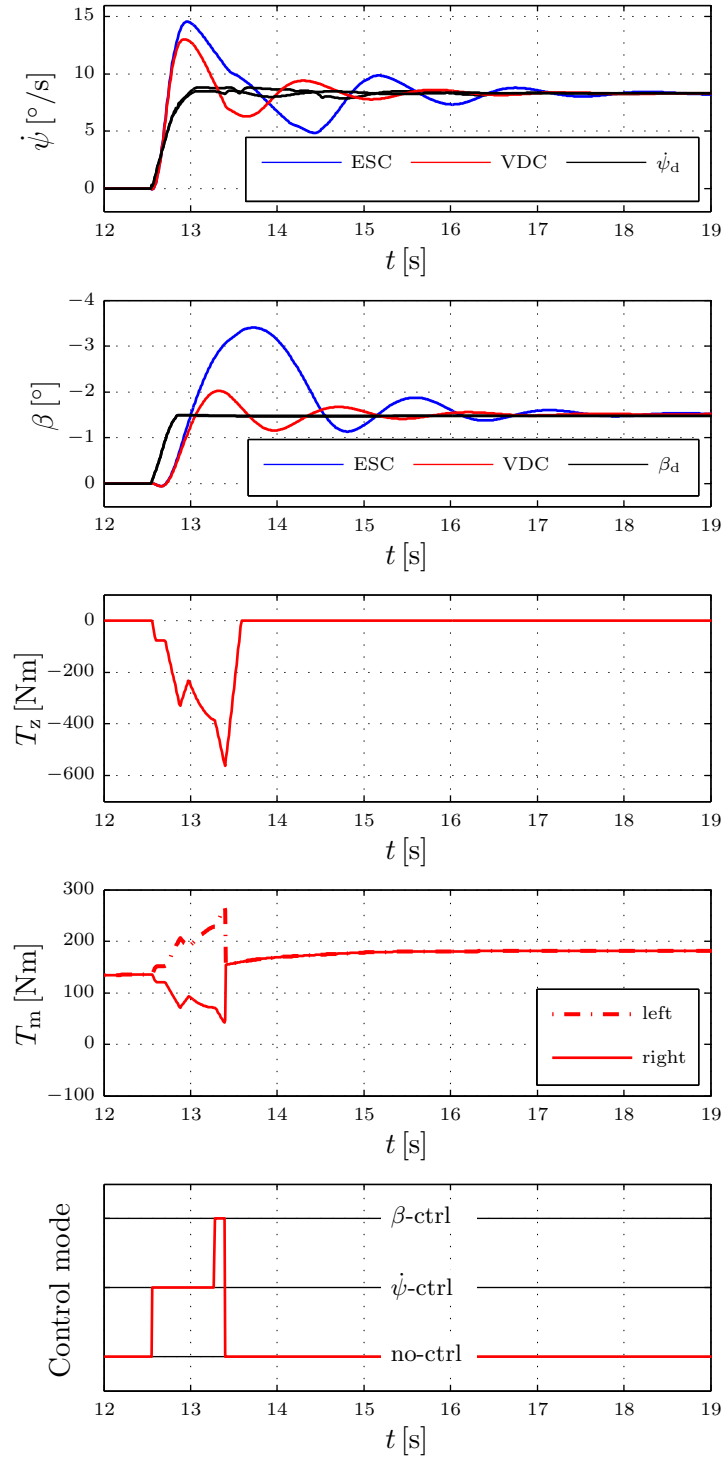


Figure 7.13: Steering wheel step. VDC applications can achieve less yaw rate overshoot and less sideslip angle overshoot. The correction torque is calculated when the yaw rate control and sideslip angle control are active.  $T_z$  results from different propulsion torques of the rear axle HAS.

<i>Evaluation criterion</i>	<i>ESC</i>	<i>VDC</i>
maximum yaw rate	19.8°/s	18.5°/s
minimum sideslip angle	-3.2°	-2.6°
maximum lateral acceleration	7.7m/s <sup>2</sup>	7.2m/s <sup>2</sup>
path deviation (2s after start lift-off)	1.4m	0.5m

Table 7.3: Simulation results for power lift-off

damp the introduced yaw motion. The path deviation for the vehicle with VDC can be kept lower than for the vehicle with ESC (see Figure 7.15). Table 7.3 summarizes the simulation results of ESC and VDC.

#### 7.4.4 Sine with dwell

According to [Nat07] and [Tod11], it is mandatory for all new homologated vehicles in the US and Europe to be equipped with a yaw motion control system. In order to test the effectiveness of controller interventions during oversteering, the *sine with dwell* maneuver was developed. This is an open-loop maneuver performed at  $v = 80\text{km/h}$ . An oversteering vehicle reaction is provoked with the steering wheel input  $\delta_D$  shown in Figure 7.16. Such a steering input is typically performed by drivers during emergency obstacle avoidance. The maneuver is valid if the lateral displacement criterion

$$\text{y-Position}(t_{\text{start}} + 1.07\text{s}) \geq 1.83\text{m} \quad (7.28)$$

is fulfilled. As this is the case for both vehicles (see Table 7.4), the results in Figure 7.17 can be evaluated based on the lateral stability criterion defined in [Nat07]. The yaw rate has to fulfill the condition

$$|\dot{\psi}| = \begin{cases} < 0.35 |\dot{\psi}_{\text{max}}| & \text{if } t_0 + 1\text{s} < t < t_0 + 1.75\text{s}, \\ < 0.2 |\dot{\psi}_{\text{max}}| & \text{if } t \geq t_0 + 1.75\text{s}, \end{cases} \quad (7.29)$$

to pass the test. This corridor is shown in Figure 7.17. The National Highway Traffic Safety Administration anticipates that a vehicle stability control system meeting these lateral stability criteria would have at least a 95% probability of preventing a spinout. Figure 7.17 shows that both systems pass the test, as the yaw rates achieved with both systems are within the specified corridor. In contrast to the intervention shown in Section 7.4.2, the rear left propulsion torque is positive for a brief time, while the rear right propulsion torque is negative. The rear right side commences recuperation to compensate for the acceleration torque and to support the establishment of a sufficiently high yaw torque. With the traction machine intervention, it is also possible to force the yaw rate to zero earlier than with the ESC. This is only possible because the electric torque vectoring functionality is applied. As the VDC also controls the sideslip angle, its magnitude can be reduced to a level where the vehicle is also easier to handle.

When the vehicle motion is observed from the bird's-eye view, the improvements are impressive (see Figure 7.18).

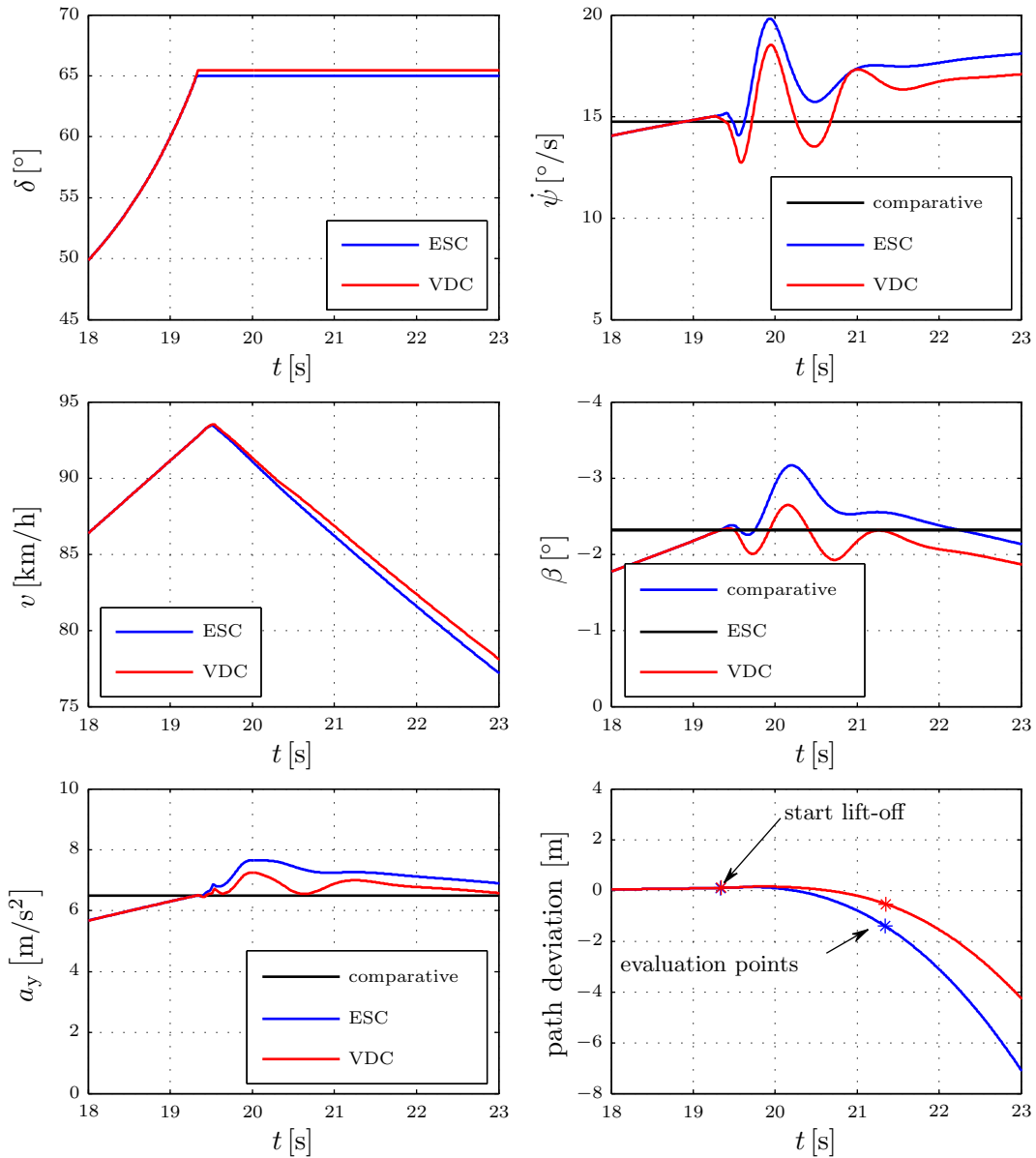


Figure 7.14: Power lift-off. The application of VDC results in less deviation from the comparative signal values and a reduced path deviation. The induced reaction of the VDC-equipped vehicle is less marked compared to the vehicle equipped with ESC.

<i>Evaluation criterion</i>	<i>ESC</i>	<i>VDC</i>
maximum yaw rate amplitude	29.2°/s	26°/s
maximum sideslip angle	9.6°	4.4°
maximum lateral displacement	3m	2.4m
lateral displacement @ $t = t_{\text{start}} + 1.07\text{s}$	2.1m	1.9m

Table 7.4: Simulation results for sine with dwell

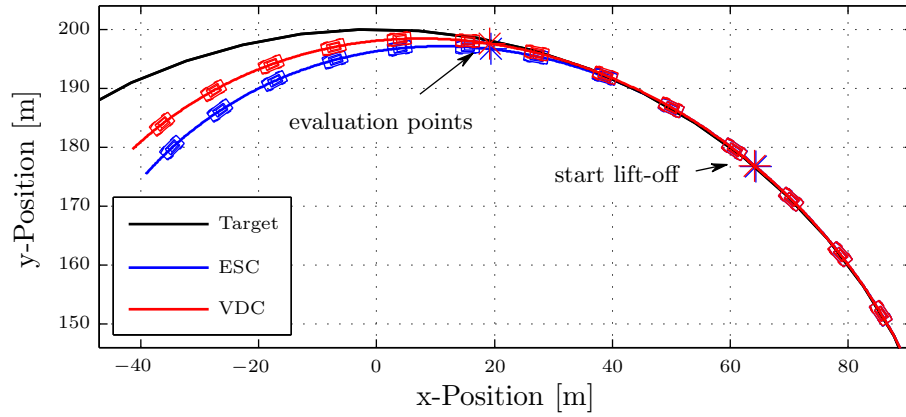


Figure 7.15: Power lift-off (bird's-eye view). Due to the faster vehicle response, the vehicle applying VDC shows a better oversteering suppression performance.

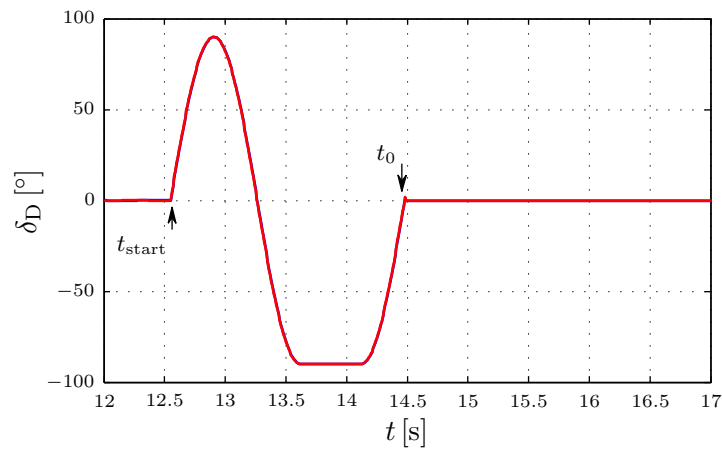


Figure 7.16: Steering wheel input for the sine with dwell maneuver

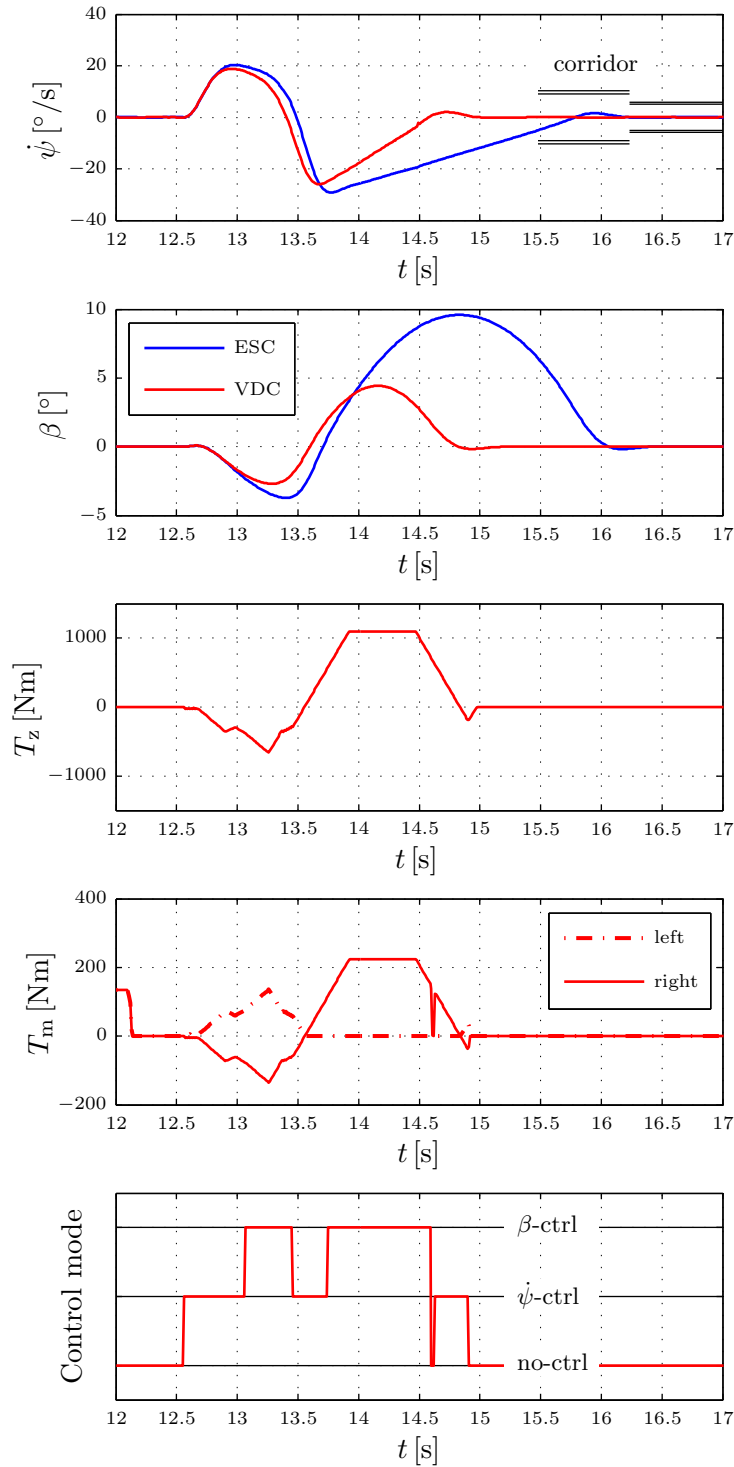


Figure 7.17: Sine with dwell. Electric torque vectoring improves the stabilization performance of the vehicle (reduced sideslip angle and higher yaw rate convergence speed). It requires control mode changes where recuperated energy is transferred from the right wheel corner to the left wheel corner, or where the left wheel corner is switched off.

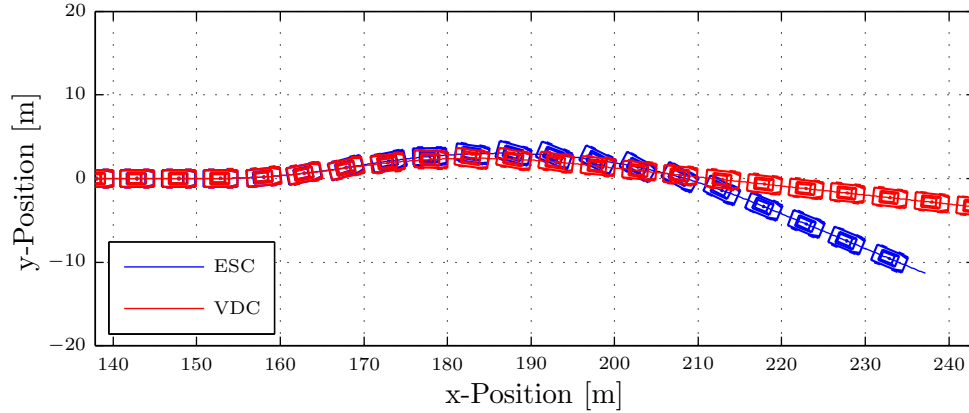


Figure 7.18: Sine with dwell (bird's-eyes view)

<i>Evaluation criterion</i>	<i>ESC</i>	<i>VDC</i>
maximum yaw rate	37.6°/s	37.3°/s
minimum yaw rate	-52.4°/s	-47.8°/s
maximum sideslip angle	6.5°	4.7°
minimum sideslip angle	-4°	-3.2°
average velocity	54.2km/h	55.7km/h

Table 7.5: Simulation results for the VDA lane change

#### 7.4.5 Double lane change

The second representative maneuver for testing the performance of obstacle avoidance is the double lane change maneuver. In contrast to the *sine with dwell*, this maneuver is a closed-loop maneuver. This thesis uses the definition found in [Int11c]. The vehicle's velocity is defined as high as possible, with the condition that the cones that indicate the lanes must not be touched (see Figure 7.20). As in the previous tests, it is possible to slightly decrease the sideslip angle when the VDC is applied (see Figure 7.19 and 7.21 and Table 7.5). Performing this maneuver with a conventional car does not allow for torque vectoring. When the VDC is used in combination with HAS control, an additional yaw torque can be set up. Since "Action 4" (see Section 7.2.2) is applied, the vehicle is more agile compared to a standard vehicle. Since the increased yaw dynamics can be used to mitigate oversteering, the vehicle motion is stabilized faster. Furthermore, the additional acceleration torque leads to a higher longitudinal velocity.

Although it is stated in [Int11c] that the vehicle's velocity is not a basis for a vehicle benchmark, for vehicle manufacturers a high longitudinal velocity is a prestige factor. By utilizing the VDC, it is possible to increase the velocity between position A and position B (see Figure 7.20) by approximately 1.5km/h when the entrance velocity at position A is about 70km/h.

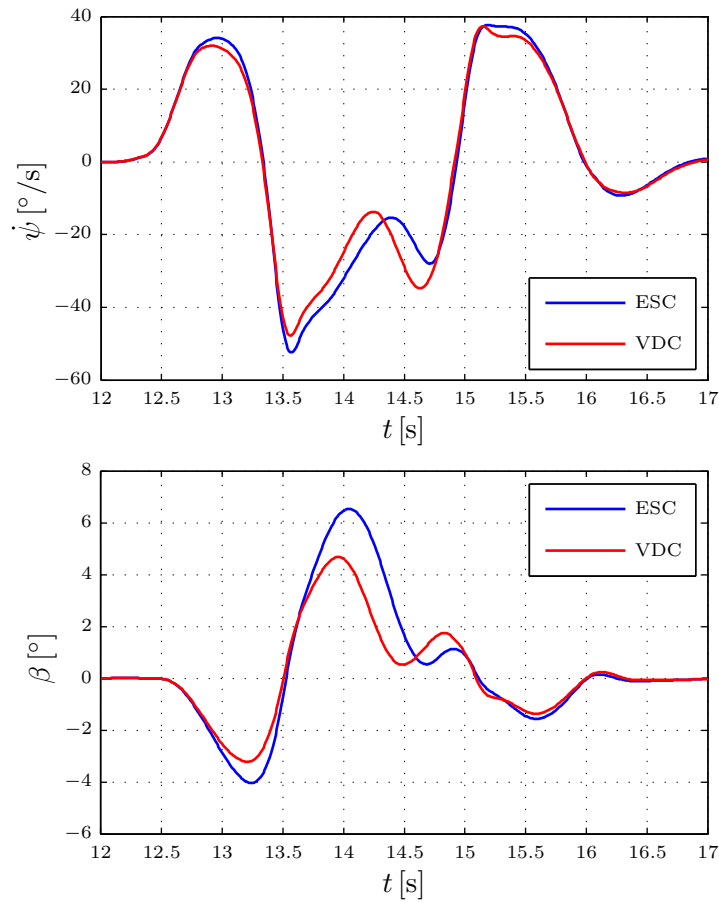


Figure 7.19: VDA lane change. Applying the VDC leads to a reduced sideslip angle. Additionally, the vehicle velocity can be increased due to torque vectoring functionality.

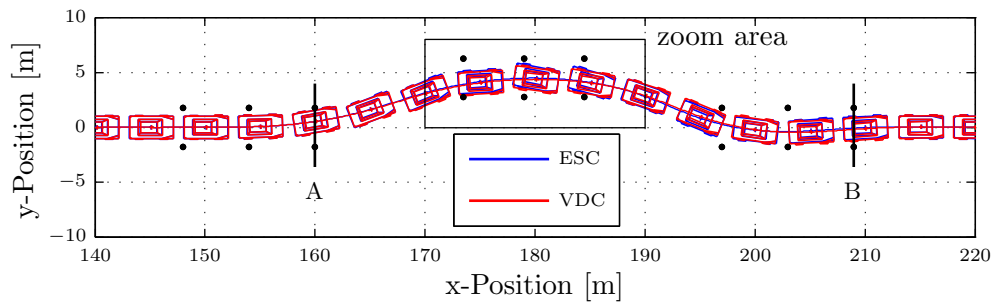


Figure 7.20: VDA lane change (bird's-eye view)

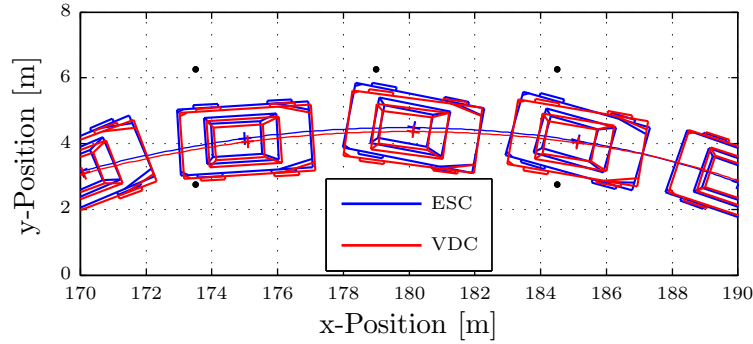


Figure 7.21: VDA lane change (bird’s-eye view zoomed). The reduced vehicle oversteering leads to a slightly different trajectory. This enables the increase of the longitudinal velocity.

### 7.4.6 Summary

From the previous simulation results, it can be concluded that the VDC is able to stabilize the vehicle in a very effective manner. By utilizing of electric traction machines and friction brakes, it is possible to improve the effectiveness of the yaw motion control system. Table 7.6 summarizes the overall benefits of applying the VDC in combination with a HAS.

<i>Test maneuver</i>	<i>Advantages of VDC</i>
emergency braking at different $\mu$ conditions	reduction of braking distance
steering wheel step	reduction of - yawrate overshoot - sideslip angle overshoot
power lift off	reduction of lateral path deviation
sine with dwell	reduction of - yawrate overshoot - sideslip angle overshoot
double lane change	reduced stabilization time reduction of - yawrate overshoot - sideslip angle overshoot increase of longitudinal velocity

Table 7.6: Summary of simulation results

## Chapter 8

# Vehicle dynamics control during electrical faults

Combining the capability of electrical traction machines with conventional friction brakes leads to an improvement of the overall performance of traction and yaw motion control. Besides the functional benefits of applying an HAS, it is essential to comply with the *ISO standard 26262:2012: Road vehicles-Functional safety* [Int12b]. The safety integrity level of a motion control system for vehicles must also be determined according to the ISO standard [Int12a]. All possible fault conditions must be evaluated in terms of their influence on the vehicle's safety and the passengers' safety.

This chapter investigates, the impact of electrical system faults and the ability of the yaw motion controller to stabilize the vehicle in the event of such faults. The electrical system faults explained in Section 4.2.4 are applied to the vehicle during three typical driving maneuvers (braking, straight ahead driving and cornering).

### 8.1 Electrical system faults during braking

#### 8.1.1 Braking under low- $\mu$ conditions

Section 7.4.1 described the performance of the VDC for the fault-free case. The performance during machine short circuit and passive recuperation can be seen in Figure 8.1 and Figure 8.2. It is assumed that the driver does not change the steering wheel position during the maneuver.

When the brake action starts at  $t = 12\text{s}$ , only the traction machines are utilized for deceleration. As the deceleration is performed under low- $\mu$  conditions, it causes the wheel slips  $\lambda$  to exceed the desired slip  $\lambda_d$  on both wheels. A wheel slip control (as explained in Chapter 6) is required. Shortly after limiting the wheel torque, a short circuit in the rear right traction machine occurs (see Figure 8.1).  $t_F$  denotes the time at which the fault occurs. In the event of a machine short circuit, the machine torque is reduced immediately. Instead of utilizing the traction machine, the friction brake must intervene. As the traction machine torque changes according to the wheel speed (see Section 4.2.4), it is not possible to actively influence its recuperation torque by means of controller interventions. When the wheel speed is reduced, the short circuit torque increases, as shown in Figure 4.16. The brake pressure is adapted to achieve a desired wheel motion. At very low speeds, the

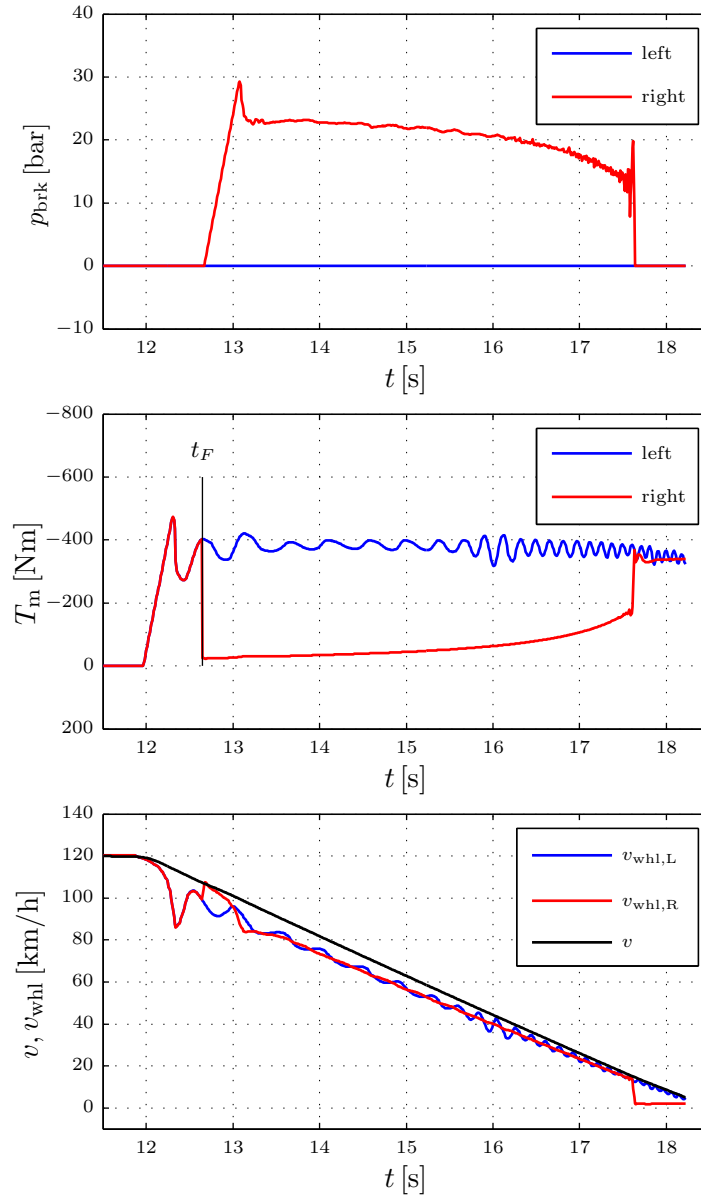


Figure 8.1: HAS braking under low- $\mu$  conditions and machine short circuit on the right-hand side. When the short circuit appears, the recuperation torque on the right-hand side changes immediately. The friction brake increases brake pressure in order to compensate for the missing wheel torque. At lower speeds, the brake pressure is reduced as the recuperation torque increases.

<i>Scenario</i>	<i>Brake distance</i>	<i>Maximum lateral displacement</i>	<i>Maximum yaw rate amplitude</i>	<i>maximum sideslip angle amplitude</i>
no fault (see Section 7.4.1)	106.4m	0.5m	3.9°/s	0.9°
machine short circuit	109.9m	0.6m	1.6°/s	0.5°
passive recuperation	109.2m	0.2m	1.9°/s	0.5°

Table 8.1: Simulation results for low- $\mu$  braking

machine torque is so high that the brake pressure has to be reduced immediately. As a further wheel torque reduction is not possible, the wheel is on the threshold of locking for a short time. Due to the torque shift from the traction machine to the friction brake, the deceleration maneuver can be performed without risks for the passengers (fail silent behavior). As stated in Table 8.1, even an intervention by the yaw motion controller is unnecessary. Only the braking distance increases, as the increase of the brake pressure is limited by a certain slew rate. In addition to the braking distance and the yaw motion signals, Table 8.1 shows the maximum lateral displacement. The displacement is the difference between the vehicle trajectory and the desired trajectory in the vehicle y-direction.

A different behavior occurs when the machine needs to be operated in passive recuperation mode. Typically, the activation of the switching elements (see Figure 4.7) is terminated immediately, and the inverter behaves like a passive rectifier. It is furthermore assumed that the inverter ECU is equipped with a fault-detection mechanism. If the error flag is set, the energy management prohibits a speed increase. If the fault cannot be diagnosed, the yaw motion controller prevents the vehicle from entering critical driving situations by adapting the propulsion torques, as well.

Figure 8.2 shows the deceleration maneuver with passive recuperation. If the fault occurs at  $t_F = 12.5\text{s}$ , the machine torque changes according to the explanations in Section 4.2.4. The wheel of the rear right corner decelerates until it reaches an equilibrium point between the traction machine torque and the load torque caused by the tire force. From  $t = 14\text{s}$  onwards, the wheel speed is lower than the critical recuperation speed. The recuperation torque is zero, and the brake system fulfills the task of wheel slip control. If the wheel speed exceeds this critical speed again, the phenomenon of passive recuperation would immediately re-appear. In this case, this is prohibited by the EM.

A blocking wheel, as in the case of the short circuit experiment, does not occur. In addition, since the influence of the traction machine is low enough in this case, no intervention of the yaw motion controller is required. Table 8.1 summarizes the braking distance achieved and the maximum values of yaw signals that occurred.

### 8.1.2 Braking under high- $\mu$ conditions

When the braking maneuver is performed under high- $\mu$  conditions, the yaw torque in the case of faults is higher than in the low- $\mu$  case. This is due to the yaw potential difference of the left and the right wheel torques. Figure 8.3 shows the braking performance for the short circuit at high- $\mu$ , and Figure 8.4 shows the results for the passive recuperation at

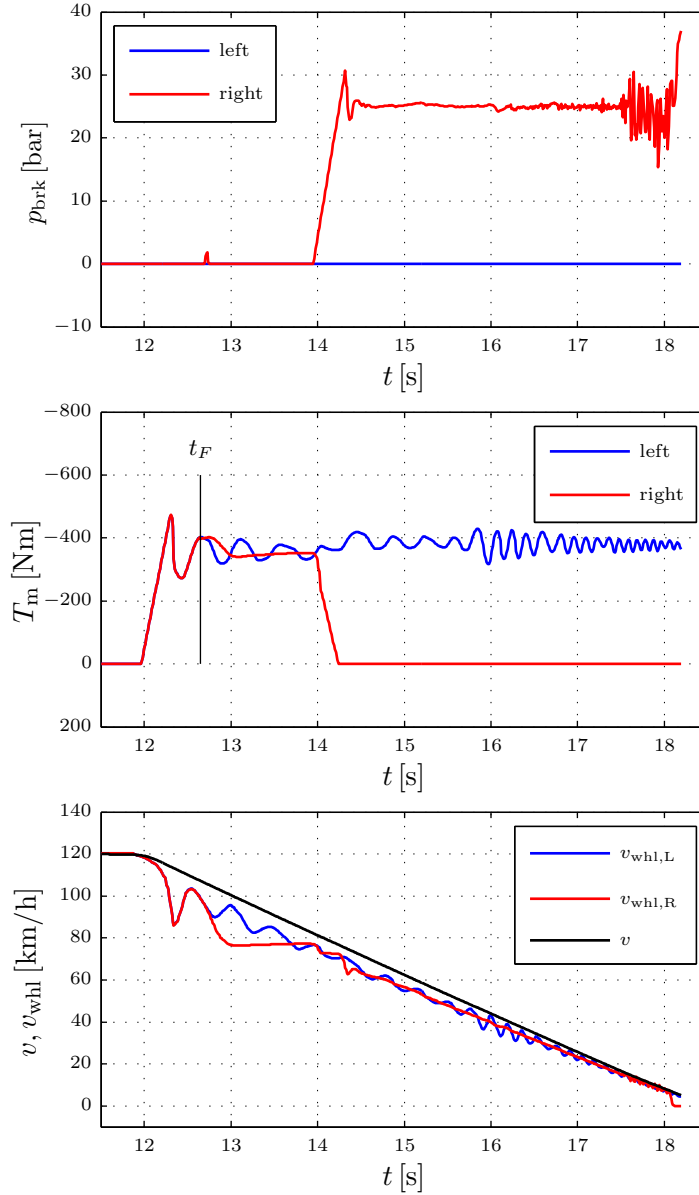


Figure 8.2: HAS braking under low- $\mu$  conditions and passive recuperation on the right-hand side. When the fault occurs, the wheel speed on the right-hand side changes immediately, and the recuperation torque is nearly constant for a second. A friction brake intervention is required when the recuperation is zero. From that time onwards, the friction brake maintains the wheel motion control.

<i>Scenario</i>	<i>Brake distance</i>	<i>Maximum lateral displacement</i>	<i>Maximum yaw rate amplitude</i>	<i>maximum sideslip angle amplitude</i>
no fault (see Section 7.4.1)	61.5m	0.4m	2.6°/s	0.4°
machine short circuit	64.6m	1.2m	3.7°/s	0.8°
passive recuperation	63.6m	0.3m	1.9°/s	0.4°

Table 8.2: Simulation results for high- $\mu$  braking

high- $\mu$ . In principle, the procedure is the same as in the low- $\mu$  case. In both cases, the friction brake is able to compensate for the lack of recuperation torque. An overbraked wheel, as in the case of the low- $\mu$  braking, is not observable. As in the low- $\mu$  cases, a brake distance increase is noticeable (see Table 8.2), which results from the torque handover between the HAS actuators. From Table 8.2, it is furthermore observable that the yaw rate and the vehicle sideslip angle remain at a low level. An intervention of the yaw motion controller is not required. As no lane-keeping system is utilized, the lateral displacement increases when the short circuit occurs. Driving safety is guaranteed throughout the entire maneuver.

### 8.1.3 Braking under split- $\mu$ conditions

The situation changes slightly when the vehicle is decelerated under split- $\mu$  conditions. Depending on the system fault and on the vehicle side, different vehicle reactions arise. Thus, the following cases were investigated

- (a) fault-free
- (b) machine short circuit under low- $\mu$  conditions
- (c) machine short circuit under high- $\mu$  conditions
- (d) passive recuperation under low- $\mu$  conditions
- (e) passive recuperation under high- $\mu$  conditions.

For further considerations, it is assumed, that the left vehicle side is at low- $\mu$ , and the right vehicle side is at high- $\mu$ .

Due to the different road conditions, an intervention of the yaw motion controller is required in all cases. Table 8.3 shows, a comparison between the brake distance, lateral displacement, yaw rate and sideslip angle, while Figure 8.5 shows the resulting yaw motion signals.

**Case a:** The results have already been shown in Section 7.4.1.

**Case b & d:** Although the vehicle stabilization is limited to the right wheel corner and the faultless friction brake of the left wheel corner, a desired vehicle motion can be achieved.

**Case c:** The impact resulting from the short circuit is too small to introduce a high yaw torque. In addition, this case is not safety critical, as the friction brake can provide enough torque.

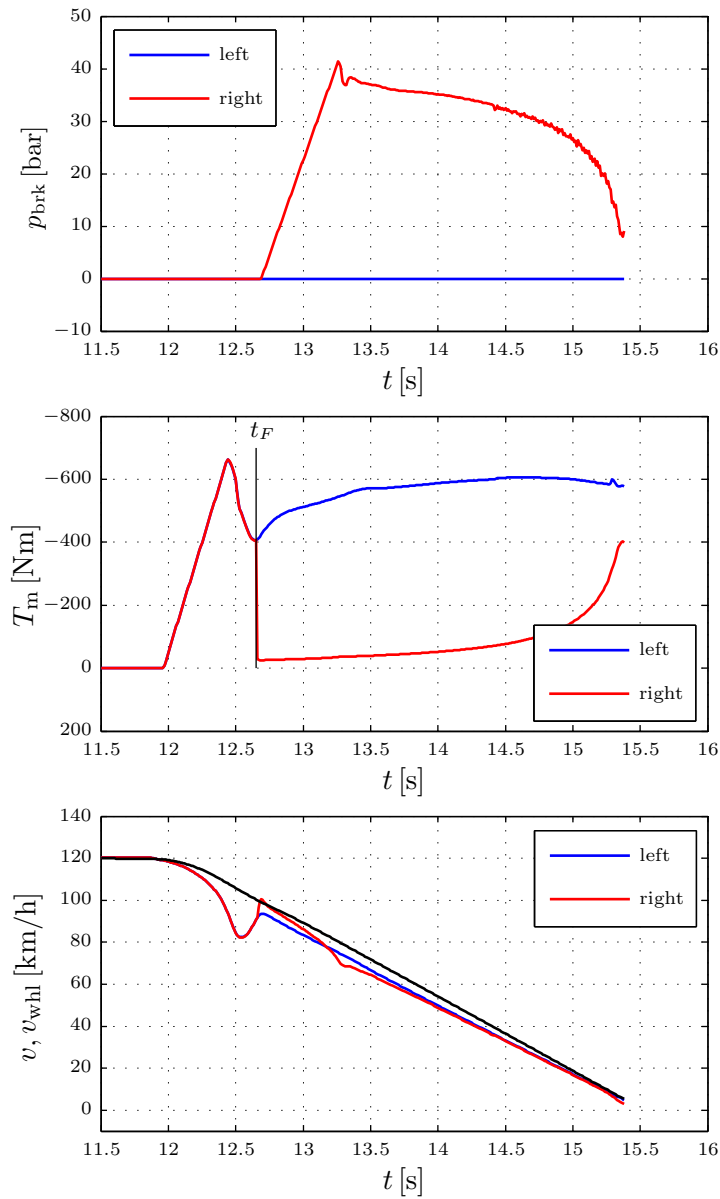


Figure 8.3: HAS braking under high- $\mu$  conditions and machine short circuit on the right-hand side. As soon as the recuperation torque reaches low values due to the machine short circuit, the friction brake increases brake pressure. The tire force potential is sufficiently high to maintain a desired wheel motion.

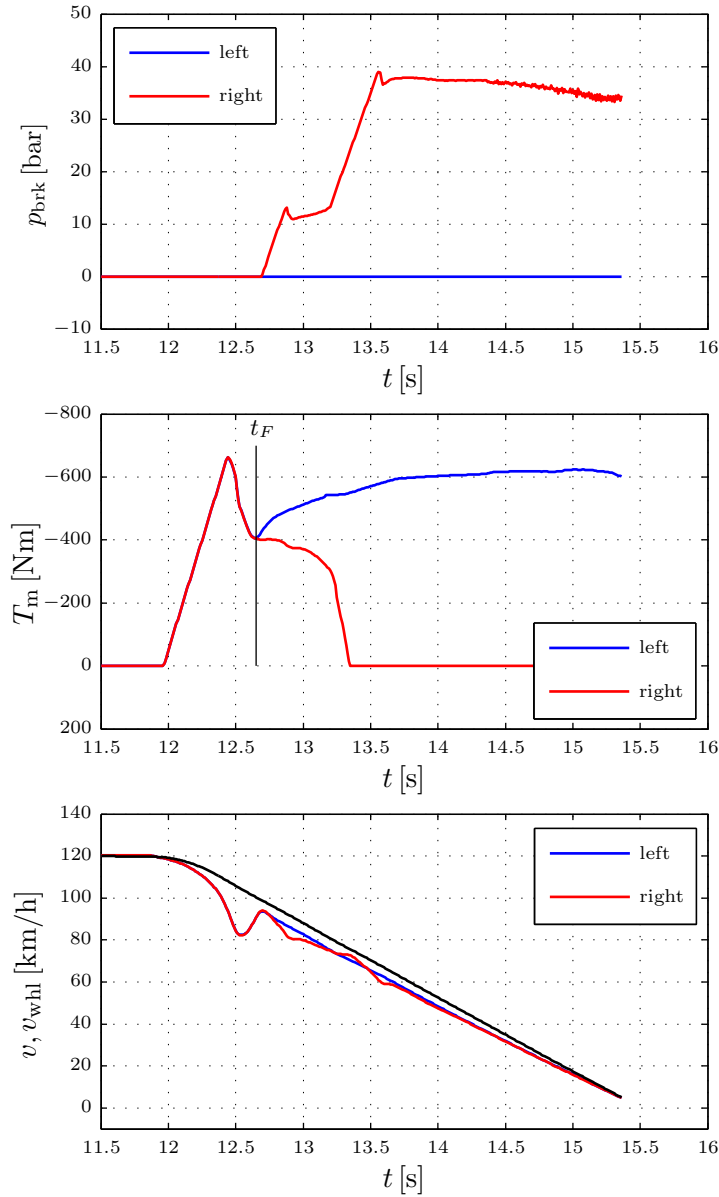


Figure 8.4: HAS braking under high- $\mu$  conditions and passive recuperation on the right-hand side. When the fault appears, the friction brake increases brake pressure. The brake pressure is adapted to achieve a desired wheel motion. When the recuperation torque reaches zero, the friction brake controls the right wheel motion, while the traction machine controls the wheel motion on the left-hand side.

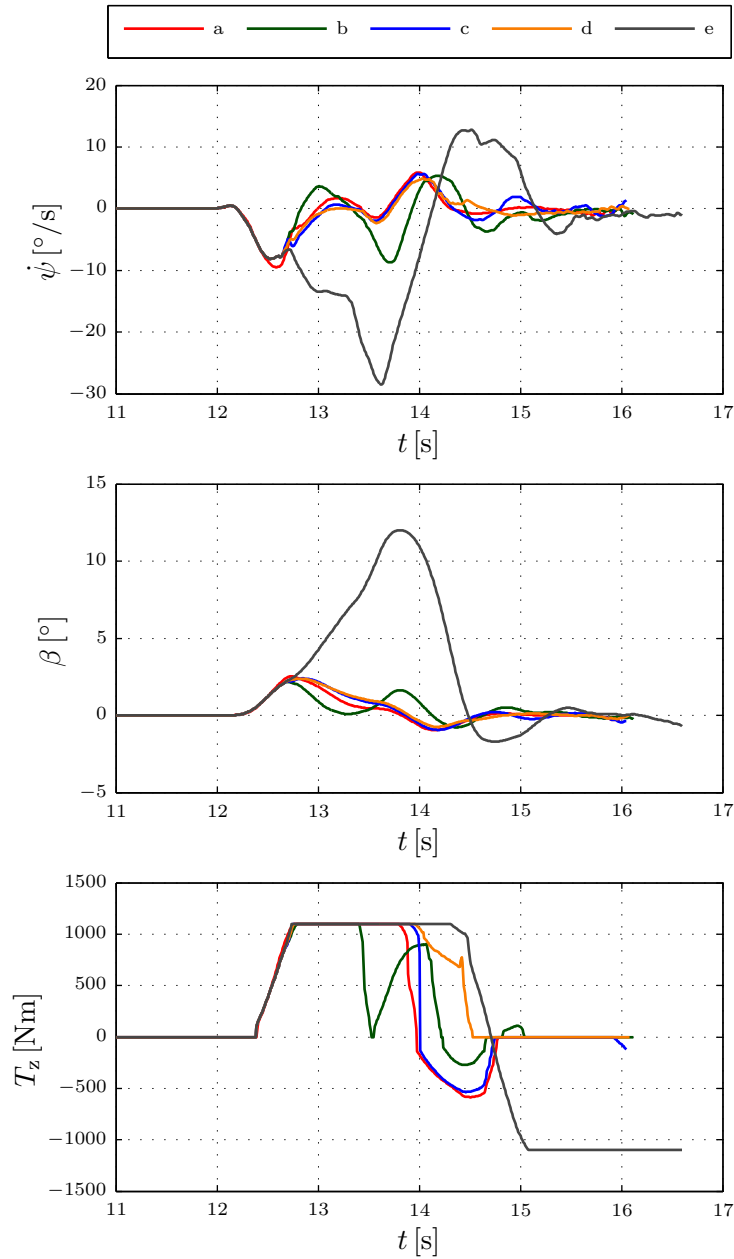


Figure 8.5: Comparison of different system faults during split- $\mu$  braking (yaw control performance). It is possible to maintain safe vehicle motion for all driving situations except for case e. Although the yaw motion controller tries to correct the vehicle motion, large values in the yaw rate and in the sideslip angle arise.

<i>Scenario</i>	<i>Brake distance</i>	<i>Maximum lateral displacement</i>	<i>Maximum yaw rate amplitude</i>	<i>maximum sideslip angle amplitude</i>
no fault (see Section 7.4.1)	82.1m	0.4m	9.3°/s	4.9°
machine short circuit at low- $\mu$	82.9m	2.8m	8.7°/s	2.2°
machine short circuit at high- $\mu$	80.8m	2.5m	8.2°/s	2.4°
passive recuperation at low- $\mu$	81.8m	2.5m	8.2°/s	2.4°
passive recuperation at high- $\mu$	85.5m	(11.9m)	28.6°/s	12.1°

Table 8.3: Simulation results for split- $\mu$  braking

**Case e:** Only in the case of passive recuperation at high- $\mu$  is the yaw torque caused by the fault torques so dominant that a stabilization of the vehicle is not possible. The resulting yaw torque causes a high yaw rate and a high sideslip angle, which requires good driving skills. Although the yaw motion controller exerts a yaw torque against the arising yaw motion, it is not possible to counteract this effect such that the sideslip angle remains low. The difference is particularly evident when observed from the bird’s-eye view (see Figure 8.6). Since such a vehicle motion should be prevented all the times, it is necessary to limit the wheel torque with the help of additional electrical or mechanical actions. For example, the possibility of disconnecting the traction machine from the wheel has to be taken into consideration.

## 8.2 Electric system faults during straight-ahead driving

The previous section analyzed the vehicle motion when the vehicle is decelerated. In most cases, the wheel slip controller was active when the faults occurred. This section examines what transpires when the faults appear while the vehicle is moving at a constant speed (without any wheel slip control action).

Since simulations showed that a machine short circuit has little influence on the vehicle yaw motion, the yaw motion is not explicitly shown here. Only in the case of passive recuperation is the impact high enough to be discussed. The fault is applied to the rear right wheel corner.

From Figure 8.7, it can be seen that the fault appears at  $t_F = 14.2$ s. At that point, the machine torques are positive. The right machine torque immediately changes to a recuperation torque, as described in Section 4.2. When the vehicle velocity is lower than the critical velocity, the recuperation torque is immediately reduced to zero. The propulsion torque of the remaining left machine is immediately ramped down to zero. This is an additional action which prevents the vehicle from building up an unintended yaw motion. Operating the vehicle with an electric system fault is not allowed. Nevertheless, a “limp-home” functionality is included which ensures that driving can be continued at a low speed. To show that such a situation can also be handled by unexperienced drivers, Figure 8.7 shows the required steering wheel angle as well.

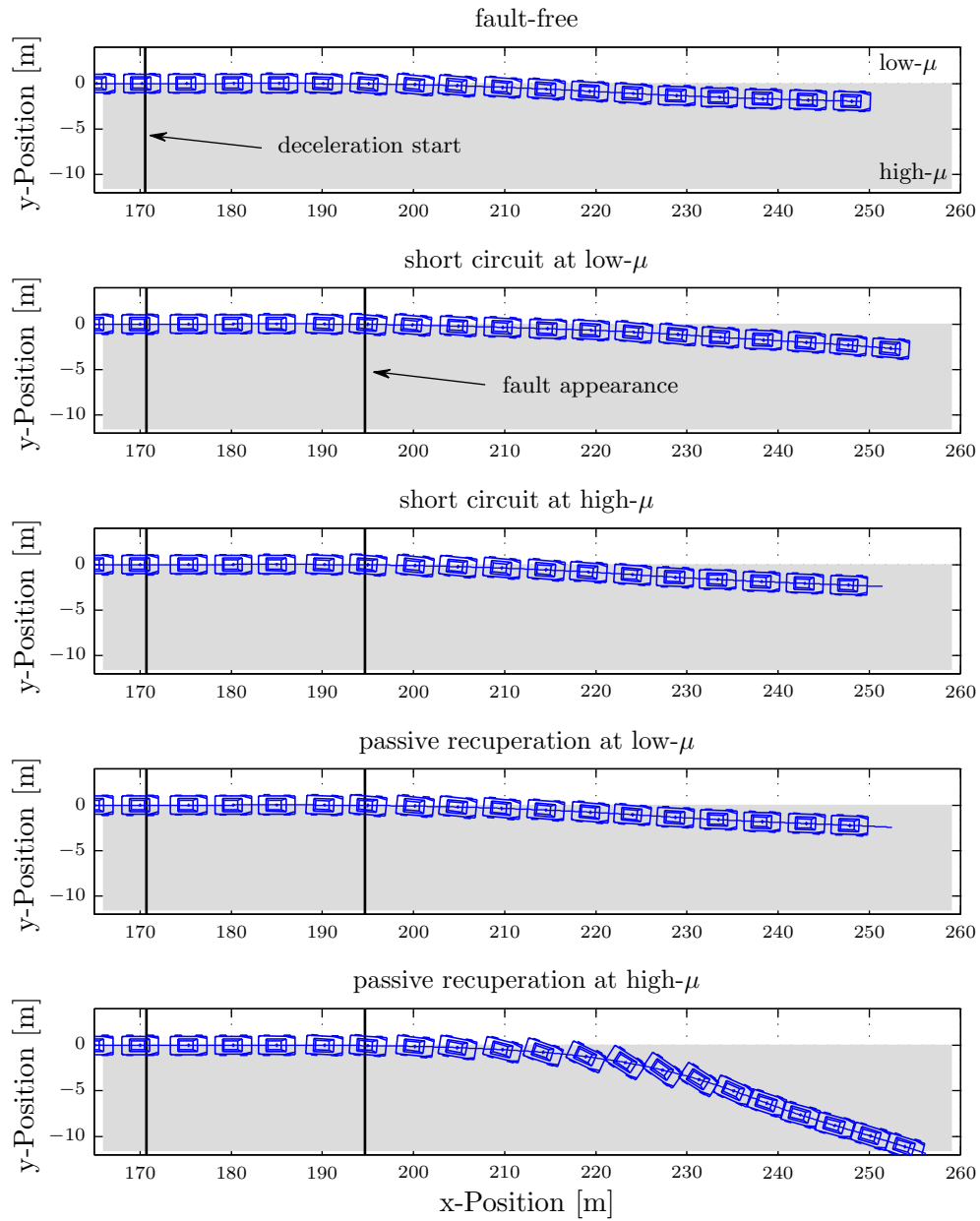


Figure 8.6: Comparison of different system faults during split- $\mu$  braking (bird's-eye view). Immediately after the fault occurs, a yaw torque is introduced into the vehicle. In the last case, an undesired yaw motion arises. As soon as the recuperation torque is zero, the vehicle can be stabilized.

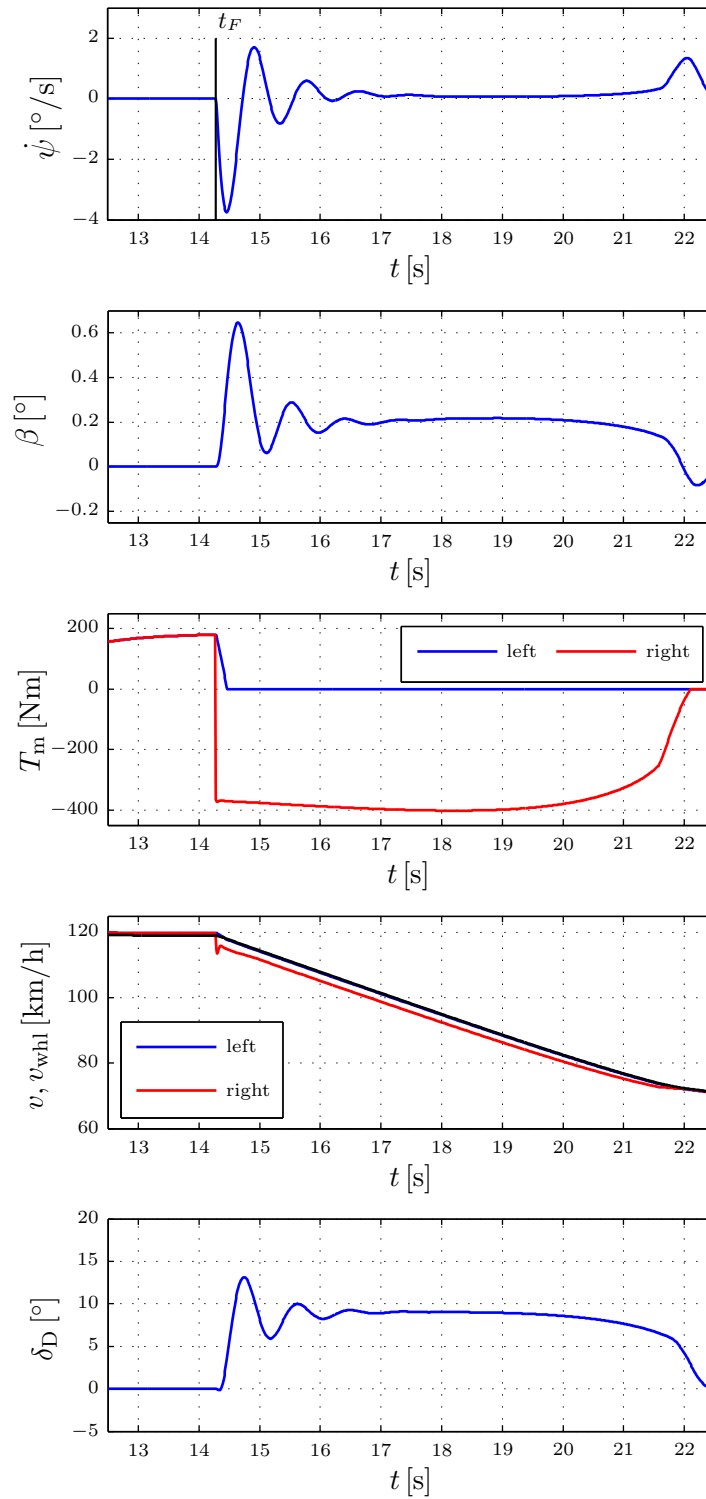


Figure 8.7: Passive recuperation on the right-hand side during straight-ahead driving. The driver must establish a wheel steering angle of  $\approx 10^\circ$ . The control system is parameterized such that the vehicle speed is slowly reduced below the critical wheel.

<i>Evaluation criterion</i>	<i>Fault free</i>	<i>Fault right</i>	<i>Fault left</i>
maximum yaw rate	11.5°/s	11.9°/s	33.9°/s
minimum yaw rate	9.5°/s	7.1°/s	-12.7°/s
maximum sideslip angle	-2.2°	-1.1°	1.1°
minimum sideslip angle	-1.8°	-2.3°	-33.4°
vehicle speed @ $t = 18.5\text{s}$	87.6km/h	71.7km/h	43.4km/h

Table 8.4: Simulation results for vehicle cornering

### 8.3 Electric system faults during vehicle cornering

The final maneuver for fault analysis is the vehicle cornering (left curve). As in Section 7.4.2, the steering wheel amplitude is fixed to  $\delta_D = 90^\circ$ . Since simulations showed that short circuits have a minor influence on the yaw motion, the achieved results are not explicitly shown here. A major drawback of short circuits in this type of situation is that it is no longer possible to make the vehicle sporty by means of torque vectoring. In terms of safety, a short circuit is not critical.

The yaw torque that arises from passive recuperation has a larger impact on the vehicle behavior. Figure 8.8 shows the simulation results for passive recuperation and fault-free conditions. The fault occurs at  $t_F = 13.7\text{s}$ . If the passive recuperation occurs on the rear right corner (curve outside), a negative yaw torque arises, which forces the vehicle to be more understeered. The resulting sideslip angle is less than the sideslip angle in the fault-free case. This is also evident in Figure 8.9, which depicts the maneuvers from the bird's-eye view. The recuperation causes a negative propulsion torque. As the aforementioned vehicle understeering is not critical for the driver, the propulsion torque on the left side can be positive, which compensates for the negative propulsion torque on the right-hand side. The friction brake is not utilized in this situation.

Nevertheless, a passive recuperation on the left-hand side (inner wheel) has a significant influence on the cornering behavior. As the recuperation torque causes an additional yaw torque, an oversteering behavior is unavoidable. From Figure 8.8 and Table 8.4, it is clearly visible that the sideslip angle and the yaw rate reach higher values than in the two previous cases. To keep the sideslip angle values low, the right-hand side also initiates recuperation. As shown in Figure 7.4, the yaw torque can be damped slightly. Furthermore, the negative propulsion torques on both sides cause a rapid decrease in velocity. Therefore, passive recuperation lasts until  $t = 14.7\text{s}$ . An additional utilization of the friction brake is not necessary, as the traction machine on the right side is powerful enough. Stabilizing the vehicle during the presence of the fault torque is not possible. For vehicle safety, it is recommended to keep the time where the fault torque influences the vehicle very brief (e.g. by disconnecting the machine from the wheel). Furthermore, the support of the front axle to stabilize the vehicle needs to be enforced. Once the recuperation torque has been eliminated, it is possible to stabilize the vehicle.

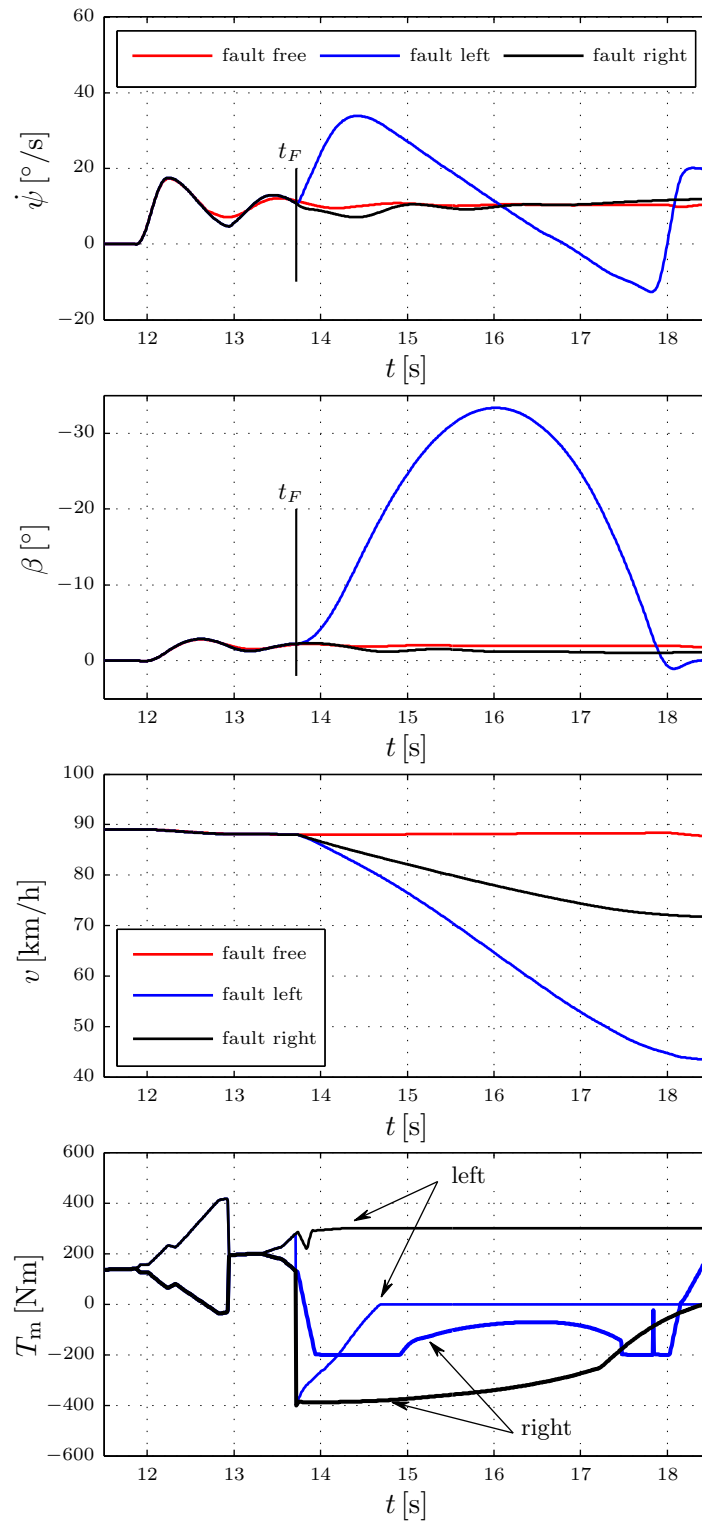


Figure 8.8: Comparison of passive recuperation on different rear axle wheels during vehicle cornering. When the fault occurs on the left-hand side, the induced yaw torque causes a fast increase of the yaw rate and the sideslip angle. The control system forces the vehicle to reduce speed immediately. As soon as the recuperation torque on the inner wheel reaches zero, the vehicle can be stabilized.

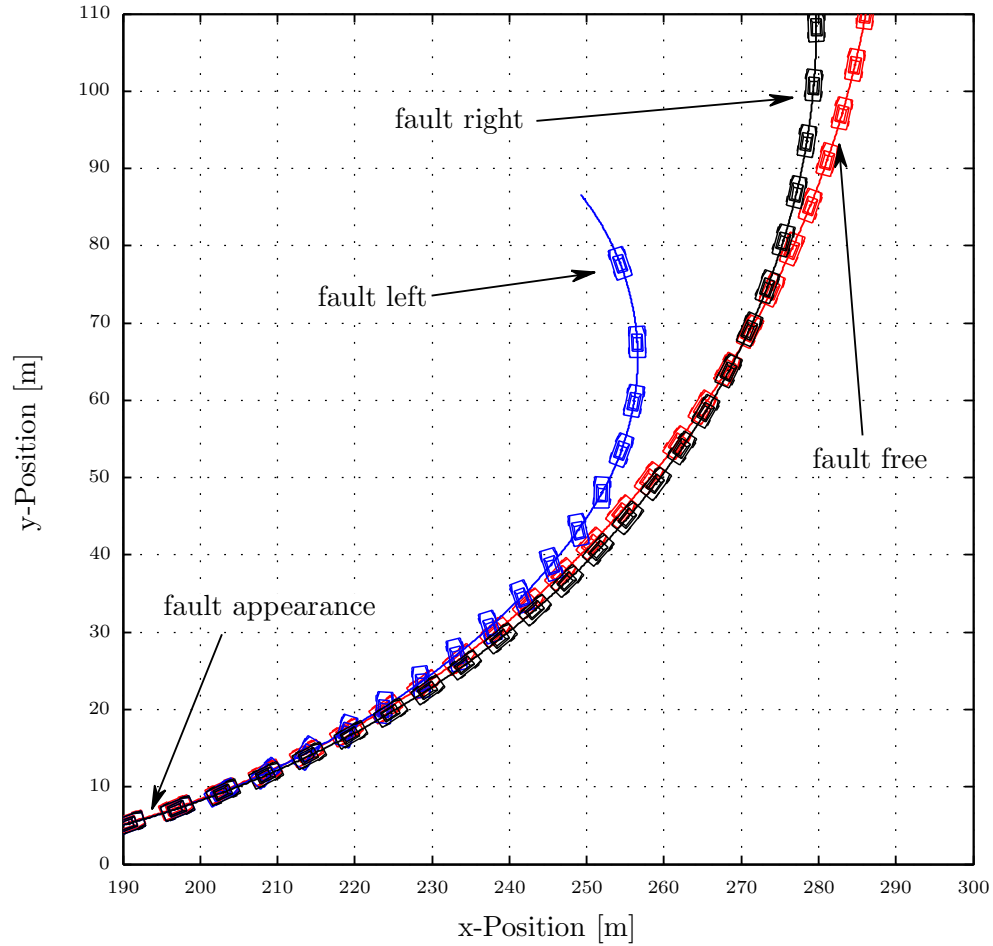


Figure 8.9: Comparison of passive recuperation on different rear axle wheels during vehicle cornering (bird's-eye view). From the bird's-eye view, it is clearly visible, that the fault on the rear right wheel (outer wheel) has almost no impact on the cornering performance. Only the yaw torque induced by the rear left wheel causes oversteering behaviour.

## 8.4 Summary

Table 8.5 provides a brief overview of the results discussed in Sections 8.1-8.3. It can be concluded that the influence on the vehicle behavior depends strongly on the driving situation and on the type of fault.

For straight-ahead driving and braking, the influence of the fault torques is less than for cornering maneuvers. While machine short circuits limit the functionalities of the overall system, it has been shown that no critical situations arise. When passive recuperation occurs, the amount of introduced yaw torque may cause undesired oversteering.

If the machine torques are less than intended, the friction brake can compensate for this shortage. If the machine torque is higher than allowed, additional measures are required, which must protect the vehicle from introducing undesired yaw torques (see Figures 8.6 and 8.9).

<i>Test maneuver</i>	<i>Influence on vehicle dynamics</i>
braking under low- $\mu$ conditions	braking distance degradation no influence on lateral vehicle stability
braking under high- $\mu$ conditions	braking distance degradation no influence on lateral vehicle stability
braking under split- $\mu$ conditions	increase of lateral path deviation minor effects when fault occurs on the low- $\mu$ side additional safety measures for passive recuperation required
straight ahead driving	propulsion torque reduction required prevention for exceeding critical velocity recommended
vehicle cornering	short circuits have less influence on lateral vehicle stability propulsion torque reduction required additional safety measures for passive recuperation required

Table 8.5: Summary of fault test simulation results

## Chapter 9

# Conclusion and Outlook

Statistics have shown that electric traction machines will play a key role in the future of automotive propulsion. Furthermore, increasing the safety of modern cars is one of the main topics in the automotive industry. The challenging objective of combining driving efficiency and vehicle safety requires a new topology of vehicle motion control. Thus, a vehicle dynamics controller for electric and hybrid electric vehicles which coordinates chassis actuators and the drivetrain actuators in a concurrent manner is being developed. This thesis introduced one possible concept that is based on the example of an electric vehicle equipped with single-wheel traction machines on the rear axle.

The initial chapters of this thesis outlined the motivation for energy-efficient driving and its harmonization with a vehicle dynamics control system. Furthermore, these chapters explained the operating principles of state-of-the-art vehicle dynamics control systems (e.g. ABS, ASC and ESC) and described the main relations of vehicle motion.

When designing a vehicle dynamics controller, it is essential to understand the operational characteristics of friction brakes and traction machines. As the traction machine plays the major role in electric vehicle propulsion, the mathematical model and the control of a permanent magnet synchronous machine were investigated in detail.

The advantages of the friction brake and the electric traction machine provide the basis for combined actuator control. Commonly used “add-on”-solutions for energy management and vehicle stability control can be extended to create an integrated solution. This enables a “concurrent” controlling the wheel motion, rather than an “either-or”-solution. With the help of a daisy chain interaction, it is possible to establish a structure of propulsion torque distribution that focuses on the actuator’s abilities. In this context, daisy chain means that the shortcomings of one actuator can be corrected by means of another actuator in order to enhance the overall system performance.

Vehicle motion control is strongly related to wheel motion control. Establishing the desired wheel motion requires a slip controller. For various reasons, controlling the wheel slip is not a trivial task (e.g. the road conditions are not known in practice). Therefore, this thesis presented a method for creating a robust wheel slip controller that can cope with system uncertainties. The controller was tested both in simulation and on an ABS test bench, which confirmed the power of combined actuator control. Furthermore, the

benefits compared to state-of-the-art control approaches were highlighted.

Conventional motion control systems halt energy recuperation when controller interventions are needed. Using the approach developed here, it is not always necessary to stop energy recuperation. In contrast to state-of-the-art strategies, a slight reduction of recuperation torque may be sufficient. The ability of the traction machines to change their torques faster than mechanical actuators can be exploited to enhance vehicle safety. For example, this thesis has shown, that braking distances are reduced, and functionalities (e.g. torque vectoring) can easily be utilized for vehicle motion control purposes.

Controlling the propulsion torques of the rear axle wheels independently from each other provides new means of vehicle motion control. In order to exploit this potential, a vehicle yaw motion controller is utilized. To cope with plant uncertainties, it is proposed to use a cascaded sliding mode control concept. This concept applies an inner yaw motion control loop and an outer sideslip angle control loop for motion control purposes. The performance of the vehicle motion controller was tested in simulations with the help of standardized driving maneuvers, and it was found that the combined control of single-wheel traction machines and conventional friction brake has advantages compared to solely using conventional brakes.

Besides the functional benefits, the direct utilization of electric propulsion torques is also associated with challenges in terms of vehicle safety. Especially in the case of electric system faults, the traction machines influence the wheel propulsion torque. To investigate this topic, two typical electric system faults were chosen to investigate the impact of unintended yaw motion generation. The results provide a good basis for understanding when additional efforts are required to reach a high safety level.

The present results provide the starting point for further research activities in the field of electric vehicle motion control. The modular structure of the presented control approaches (actuator control, integrated actuator control and yaw motion control) are not limited to single-wheel application. They can easily be extended to other topologies, such as single-motor topologies. In the near future, the concepts will be implemented on prototype vehicles and will be evaluated in practice.

Finally, since the approaches presented here focus on independent actuator accessibility, they can also be used for so-called “by-wire applications”, which makes them well suited for future vehicle technologies.

# Appendix A

## Sliding mode control

In this chapter the basics of sliding mode control are explained. This explanation is based on the assumption that the equilibrium point  $x_e = 0$  of the first order system

$$\dot{x} = a(x) + bu \quad (\text{A.1})$$

has to be stabilized. In general,  $a(x)$  can be nonlinear in  $x$ . If the control input  $u$  is chosen as

$$u = u(x) = \frac{1}{b}(-a(x) - kx), \quad (\text{A.2})$$

the closed loop dynamics is given by the linear system

$$\dot{x} = -kx. \quad (\text{A.3})$$

From linear system theory it is known, that  $x_e$  is asymptotically stable if  $k > 0$ . When the system starts at the initial condition  $x_0 = x(t = 0)$ , it takes an infinite time to reach  $x_e = 0$  as

$$x(t) = x_0 e^{-kt}. \quad (\text{A.4})$$

In contrast, a choice of the control law such that

$$u = \frac{1}{b}(-a(x) - k \operatorname{sgn}(x)), \quad (\text{A.5})$$

with

$$\operatorname{sgn}(x) = \begin{cases} +1, & \text{if } x > 0, \\ 0, & \text{if } x = 0, \\ -1, & \text{if } x < 0, \end{cases} \quad (\text{A.6})$$

leads to the closed loop dynamics

$$\dot{x} = \begin{cases} -k, & \text{if } x > 0, \\ 0, & \text{if } x = 0, \\ k, & \text{if } x < 0. \end{cases} \quad (\text{A.7})$$

The time  $\tau_e$  for reaching  $x_e$  can be calculated with

$$\tau_e = \frac{|x_0|}{k}, \quad (\text{A.8})$$

i.e. system (A.7) allows finite-time convergence to the equilibrium point  $x_e$ . The drawback of control law (A.5) is that its realization requires an ideal application of the sgn-function. As in reality only finite switching frequencies are available, the undesired chattering effect [SL99] occurs in the system. To avoid chattering the sgn-function is replaced by a saturation-function which reads as

$$\text{sat} \left( \frac{x}{\phi} \right) = \begin{cases} +1, & \text{if } \frac{x}{\phi} > 1, \\ \frac{x}{\phi}, & \text{if } -1 \leq \frac{x}{\phi} \leq 1, \\ -1, & \text{if } \frac{x}{\phi} < -1, \end{cases} \quad (\text{A.9})$$

Replacing the sgn-function by (A.9), control law (A.5) results in

$$u = \frac{1}{b} \left( -a(x) - k \text{sat} \left( \frac{x}{\phi} \right) \right). \quad (\text{A.10})$$

In (A.10) the strictly positive parameter  $\phi$  characterizes the width of the so-called boundary layer. When

$$|x| > \phi \quad (\text{A.11})$$

there is no difference between (A.5) and (A.10). If

$$|x| \leq \phi, \quad (\text{A.12})$$

the closed loop dynamics reads as

$$\dot{x} = -\frac{k}{\phi}x. \quad (\text{A.13})$$

Figure A.1 shows a timing characteristic of  $x$  when the control laws (A.5) and (A.10) are applied to system (A.1). The system response is the same for both controllers as long as the boundary layer is reached. When  $|x| \leq \phi$ , the controller (A.5) needs a finite time to achieve  $x = 0$ . On the contrary, controller (A.10) requires a finite time to reach  $x = 0$ , but the workload for the actuator is less than for the actuator driven by controller (A.5).

In most cases, the system to be controlled has uncertainties  $\Delta$  which are not known exactly. System (A.1) can be represented as

$$\dot{x} = a(x) + bu + \Delta. \quad (\text{A.14})$$

In general, these uncertainties can be state-dependent and time-dependent, but are assumed to be bounded

$$|\Delta| = |\Delta(x, t)| \leq \Delta_{\max}. \quad (\text{A.15})$$

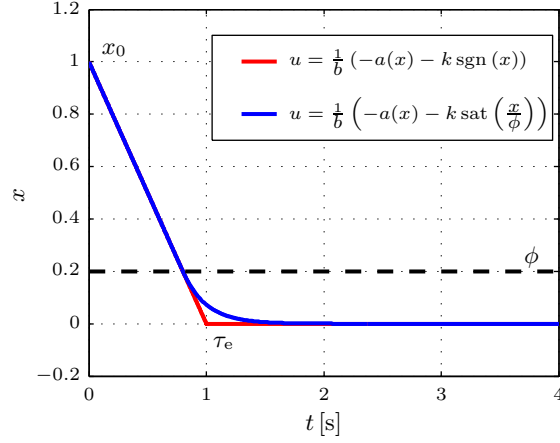


Figure A.1: Sliding mode control with/without boundary layer

When control law (A.5) is applied to system (A.14), the closed loop dynamics result in

$$\dot{x} = -k \operatorname{sgn} x + \Delta. \quad (\text{A.16})$$

As in practical implementations the control law (A.10) is applied, the closed loop dynamics within the boundary layer results in

$$\dot{x} = \Delta - \frac{k}{\phi} x. \quad (\text{A.17})$$

This means, that instead of the desired equilibrium point  $x_e = 0$ , the equilibrium point

$$x_e = \frac{\phi \Delta}{k} \quad (\text{A.18})$$

is reached. One possibility to overcome this situation is to insert integrating behavior, i.e. increase the system order. Therefore, the design should now be extended to systems of higher order. Exemplary, the design is shown for a second order system

$$\begin{aligned} \dot{x}_1 &= x_2 \\ \dot{x}_2 &= a(x_1, x_2) + bu. \end{aligned} \quad (\text{A.19})$$

As in the case of the first order system, the equilibrium point  $x_{1,e} = 0$ ,  $x_{2,e} = 0$  should be stabilized. If  $x_2$  could be chosen arbitrarily, the choice

$$x_2 = -\gamma x_1 \quad (\text{A.20})$$

would yield

$$\dot{x}_1 = -\gamma x_1. \quad (\text{A.21})$$

With the tuning parameter  $\gamma > 0$ , this would lead to

$$\lim_{t \rightarrow \infty} x_1(t) = 0 \quad (\text{A.22})$$

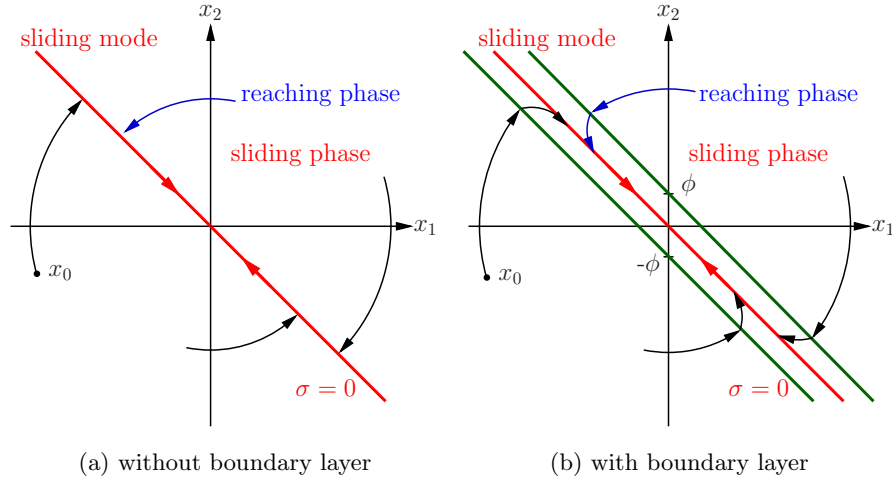


Figure A.2: Sliding mode control

which implies

$$\lim_{t \rightarrow \infty} x_2(t) = \lim_{t \rightarrow \infty} (-\gamma x_1(t)) = 0. \quad (\text{A.23})$$

As  $x_2$  cannot be chosen arbitrarily, a new variable  $\sigma$  is introduced.  $\sigma$  denotes the “sliding variable”, which can be defined as

$$\sigma = x_2 + \gamma x_1. \quad (\text{A.24})$$

If the “sliding surface”

$$\sigma = 0 \quad (\text{A.25})$$

is reached, then the system is in “sliding mode” where relation (A.20) holds. It takes a finite time to reach the sliding surface (reaching phase). Once on the sliding surface, it takes an infinite time to end up in  $x_{1,e} = 0$ ,  $x_{2,e} = 0$  (sliding phase).

The graphical representation for different initial points is shown in Figure A.2a. Figure A.2b shows the system behavior if a boundary layer is applied. It takes a finite time to enter the boundary layer and an infinite time to end up in  $x_{1,e} = 0$ ,  $x_{2,e} = 0$ , as well but the workload for the actuator is less than for the actuator driven by (A.5).

The task is now to find a control input  $u(x_1, x_2)$  such that  $\sigma$  is driven to zero in finite time. Equations (A.19) and (A.24) yields

$$\dot{\sigma} = a(x_1, x_2) + bu + \gamma x_2. \quad (\text{A.26})$$

Defining the  $\sigma$ -dynamics as

$$\dot{\sigma} \stackrel{!}{=} -k \operatorname{sgn}(\sigma) \quad (\text{A.27})$$

leads to the control law

$$u = \hat{u} + u_{\text{sw}}, \quad (\text{A.28})$$

where

$$\hat{u} = -\frac{1}{b}(a(x_1, x_2) + \gamma x_2) \quad (\text{A.29})$$

is the so-called equivalent control and

$$u_{sw} = -\frac{k}{b} \text{sgn}(\sigma) \quad (\text{A.30})$$

is the discontinuous part [UGS99]. Following the statements in [SL99] it is possible to extend this design technique to higher order systems as well.

Furthermore, asymptotic stability of (A.25) can be proven. According to Lyapunov's second stability theorem [Kha96], the equilibrium point  $\sigma = 0$  of the autonomous system  $\dot{\sigma} = f(\sigma)$  is asymptotically stable in the sense of Lyapunov if a function  $V(\sigma)$  with continuous first partial derivative can be found such that

- $V(\sigma)$  is positive definite and
- $\dot{V}(\sigma) = \frac{\partial V(\sigma)}{\partial \sigma} f(\sigma)$  is negative definite.

Therefore, the globally positive definite Lyapunov candidate

$$V(\sigma) = \frac{1}{2}\sigma^2 \quad (\text{A.31})$$

is chosen. With

$$\dot{V}(\sigma) = \sigma \dot{\sigma} = -k\sigma \text{sgn}(\sigma) = -k|\sigma| < 0 \quad (\text{A.32})$$

asymptotic stability can be guaranteed.

# Appendix B

## Test bench

The wheel slip controller derived in Chapter 6 is tested in simulations and on a test bench at the Alpen-Adria University Klagenfurt. This chapter describes the setup of the test bench and provides additional information about the measurement results shown in Chapter 6.

### B.1 Test bench layout

The test bench is shown in Figure B.1, and its schematic is depicted in Figure B.2. It mainly consists of the Electric Traction Drive (ETD) and the hydraulic friction brake B, which represent an HAS.

Besides the main components, further devices are required. In order to make the brake tests reproducible, the friction brake must be actuated with the help of the pump  $P$  and the actuation valve  $V$ . The pump therefore operates at constant speed, while the actuation valve (proportional actuation characteristic) controls the inflow into the actuation cylinder. This inflow causes the brake pedal to move, which leads to a pressure in the main brake cylinder and to a brake pressure  $p_{\text{brk}}$ . In addition, a standard ABS valve block is installed. An ECU is required for controlling the actuation valve and the ABS valve block. Furthermore, the ETD is connected to a power inverter, which ensures the proper operation of the machine.

In addition to controlling the wheel slip, it is possible to change the wheel load force  $F_z$ . The required hydraulic circuit is not shown in Figure B.2. Controlling the load force during a braking maneuver is not possible.

As Figure B.1 shows, the test bench is equipped with a moped tire. Therefore, the simulation results and the measured test bench results in Chapter 6 do not fully match. However, a verification of the properties of the HAS is certainly possible.

For safety reasons, the maximum wheel velocity is limited to  $v_{\text{whl}} = 40\text{km/h}$ . The angular velocity of the road cylinder corresponds to the vehicle velocity  $v$ .

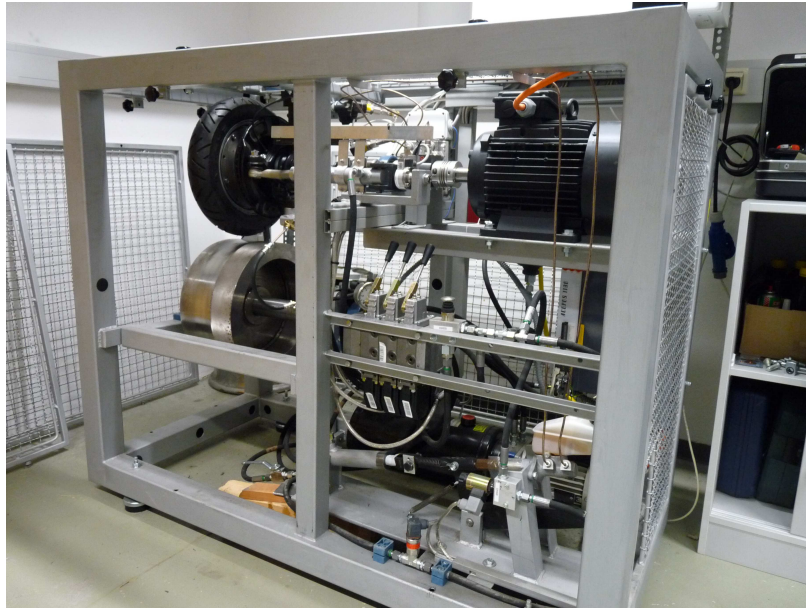


Figure B.1: Test bench

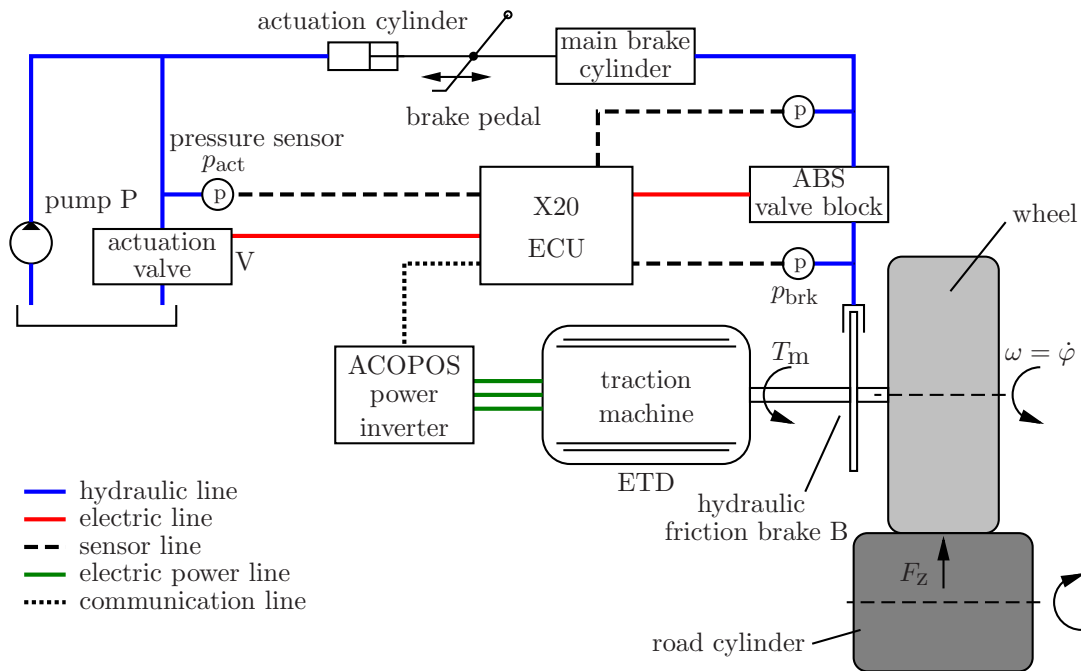


Figure B.2: Test bench (schematic)

## B.2 Test bench control layout

From Figure B.2, it can be seen that two control units are used to operate the test bench. Thus, the algorithms for wheel slip control and HAS control have to be separated into two parts, located on the ACOPOS and on the X20 ECU. Figure B.3 shows the structure of the control software. It includes all software parts that are required for the wheel slip control, as well as for an automated execution of the experiments.

As shown in Figure B.3, the traction machine controller and the wheel slip controller are implemented on the ACOPOS power inverter. In addition, a mode selection module and a torque assignment module are required on the ACOPOS, so that different modes (e.g. the modes presented in Chapter 6), can be realized with one software. Furthermore, the machine control requires a software module for sensor evaluation. Implementing the brake control on the power inverter as well would be beneficial for the control performance, but is not possible due to limited hardware resources. Therefore, the X20 ECU covers all modules which are required for the friction brake control (friction brake controller, mode selection module and sensor evaluation module). Additionally, the modules for establishing the desired starting conditions (e.g. parameter setup, mode selection, EM and velocity control) are located within the X20 ECU. Safety functions and functions required for the system startup are integrated into the general coordination module.

The software for the ECU is generated directly from Simulink<sup>TM</sup> by using automated code generation. The code for the inverter is programmed in the B&R specific language called *function block coding*. Communication between ECU and inverter is established via Ethernet. It lasts for time delays up to  $\Delta t \approx 70\text{ms}$  per direction. This communication delay is a property of the test bench, which limits the ability to prove the real performance of the combined HAS control. For vehicle applications, this communication delay should be reduced significantly. Computing the controllers on only one ECU (e.g. on the inverter) would completely eliminate these communication efforts.

All measurements are conducted with B&R Automation Studio. The required B&R hardware specifications and software support can be accessed at [BR12].

## B.3 Wheel slip control with on/off-valves

The test bench includes a standard ABS valve block (see Figure B.4), which can be used to control the wheel brake pressure  $p_{\text{brk}}$ . It consists of two on/off valves  $V1$ ,  $V2$  and a pump  $P1$  (see Figure B.4), which enable a fast brake pressure change. For economic reasons, the ABS valves can only remain in their “open” position or their “closed” position. Therefore, the wheel slip control is only possible by opening and closing  $V1$  and  $V2$ . In order to increase the response of the brake pressure, it is also possible to access pump  $P1$ . The valve block is used such that connection 1 is connected to the main brake cylinder, and connection 2 is coupled to the brake caliper.

The ABS valve block is used to change the brake pressure when the system is operated in the *ABS braking* mode. For all other modes (e.g. combined control and friction brake control), the aforementioned actuation valve  $V$  is used to set up  $p_{\text{brk}}$ .

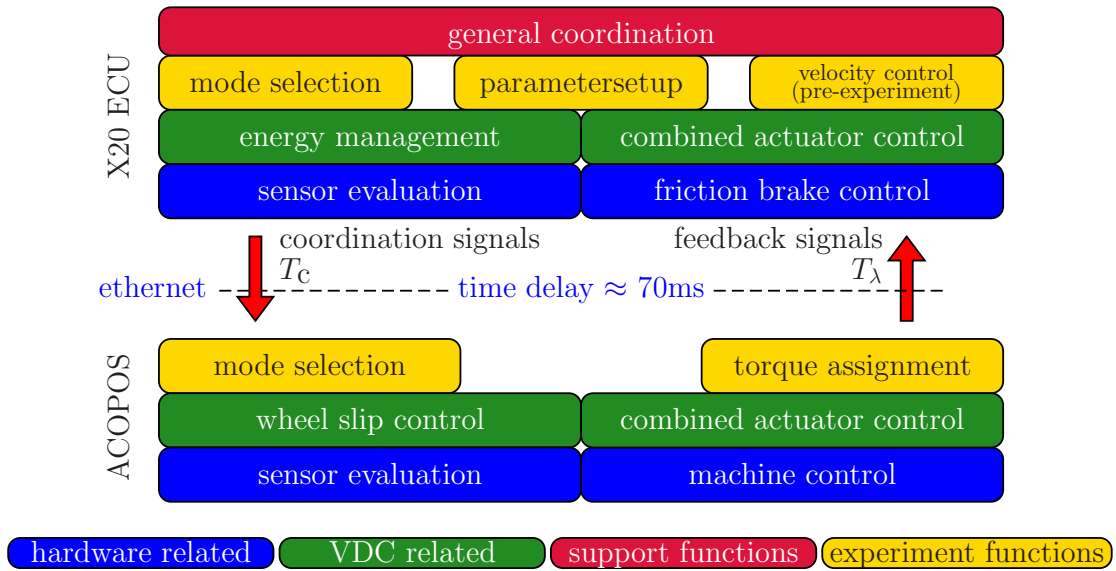


Figure B.3: Test bench software structure

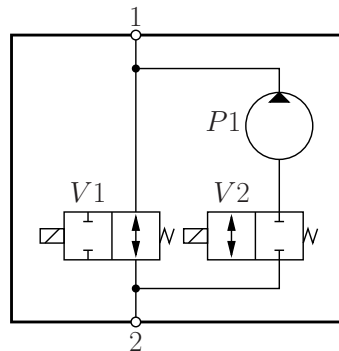


Figure B.4: ABS valve block (schematic layout)

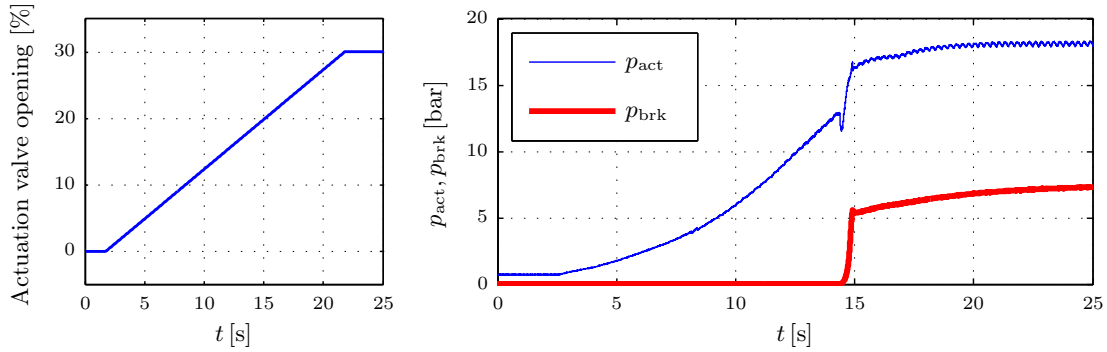


Figure B.5: Stickslip in the hydraulic circuit during pressure increase

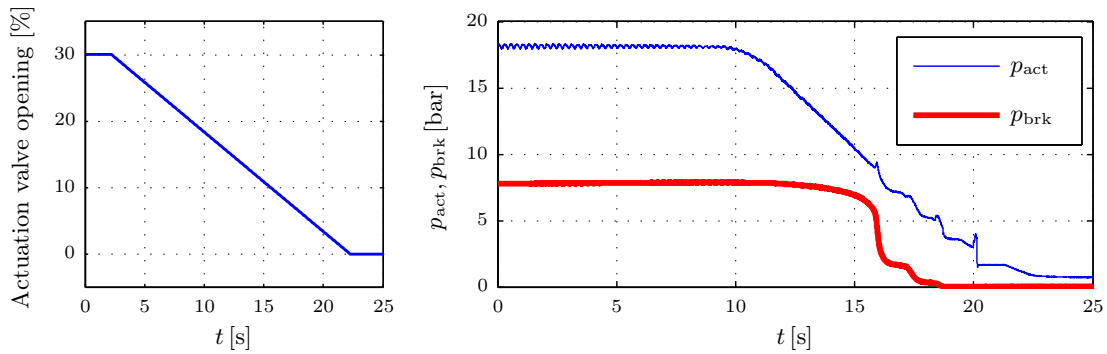


Figure B.6: Stickslip in the hydraulic circuit during pressure decrease

## B.4 Stick slip effects

As mentioned in Section 6.3.2, stick slip phenomena influence the performance of the HAS friction brake. When the brake pressure  $p_{\text{brk}}$  is established by actuating valve  $V$ , the stick slip effects of the actuation cylinder and the main brake cylinder arise. This can be verified by measurements. As shown in Figure B.5, the actuation valve has to reach a certain position before the actuation pressure changes. The main cylinder piston overcomes the friction force if  $p_{\text{act}} > 13\text{bar}$ . The resulting brake pressure  $p_{\text{brk}}$  immediately changes to a high value.

The same effect appears when a pressure decrease is required. As shown in Figure B.6,  $p_{\text{act}}$  changes its value if  $p_{\text{act}} < 9\text{bar}$ . Comparing the pressure level in Figure B.6 with the required pressure levels in Section 6.3 confirms that the stick slip effects are dominant in this control application. Even though a cascaded control loop with a robust controller is used (as proposed in [LSH13]), the effects of stick slip are observable in the measurements.

## B.5 Load force variation

From the measurement results in Section 6.3, it is apparent that the wheel slip  $\lambda$  never reaches the desired constant value  $\lambda_d$ . Even if the traction machine controls the wheel slip, this is not possible (see Figure B.7a). As analyzed in Figure B.7b, the wheel slip oscillates by a wheel travel of  $\Delta x\text{-Position} \approx 1.25\text{m}$ . This is exactly the circumference of the moped tire. In Figure B.8, a change of tire load force is observable. From  $t = 0$  to

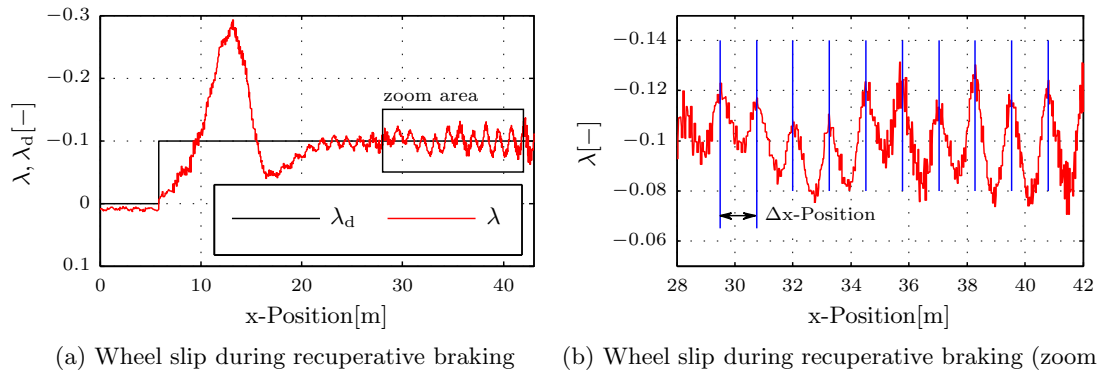


Figure B.7: Wheel slip variation due to load force change

$t \approx 4s$ , the wheel is at rest (see Figure B.8a). Afterwards, it is accelerated to a wheel speed of  $v_{whl} = 2km/h$ . Based on the angular wheel position  $\varphi$ , the vertical load force varies between  $F_z = 55N$  and  $F_z = 100N$  (see Figure B.8b). This periodic change in the load force has the same effect as a change in the road surface friction coefficient  $\mu$ . Thus, periodic wheel slip oscillations occur.

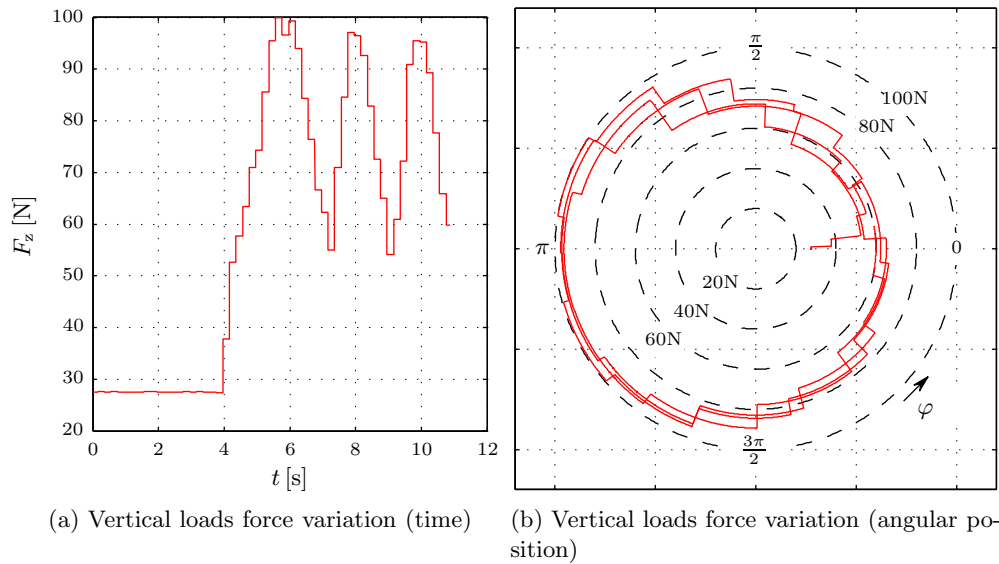


Figure B.8: Vertical loads force variation

# Bibliography

- [Amm97] D. Ammon. *Modellbildung und Systementwicklung in der Fahrzeugdynamik*. B. G. Teubner Stuttgart, 1997.
- [Ant08] S. Antonov. *Model-based Vehicle Dynamics Control*. Shaker Verlag, 2008.
- [AS01] W. Achenbach and U. Stoll. Weltneuheit bei den Bremsen: Die Sonsotronic Brake Control (SBC). *Sonderausgabe ATZ - Automobiltechnische Zeitschrift*, 103:92–99, 2001.
- [BB07] B. Breuer and K.H. Bill. *Brake Technology Handbook*. SAE International, 2007.
- [Böc11] J. Böcker. Controlled Three-Phase Drives. Technical report, Fachgebiet Leistungselektronik und Elektrische Antriebstechnik, Universität Paderborn, 2011.
- [BGA07] F. Busch, S. Grošanić, and S. Assenmachten. eSafety-Implementation Status Survey 2007. Technical report, Technische Universität München, 2007.
- [Bic04] M. Bichler. Torque Vectoring - Beurteilung von Antriebssträngen mit variabler Kraftverteilung in Bezug auf Fahrdynamik und Traktion. Master's thesis, Technische Universität München, 2004.
- [Bün98] T. Bünte. *Beiträge zur robusten Lenkungsregelung von Personenkraftwagen*. PhD thesis, RWTH Aachen, 1998.
- [BR12] Bernecker and Rainer. B&R Industrie-Elektronik GmbH. <http://www.br-automation.com>, 2012. [Online; last accessed 20-October-2012].
- [Bre11] D. Brenner. Methoden zur Online-Schätzung fahrdynamischer Kenngrößen. Master's thesis, Graz University of Technology, 2011.
- [Bun08] Bundesrepublik Österreich. *Bundesgesetzblatt für die Republik Österreich: 46. Bundesgesetz, mit dem das Normverbrauchsabgabengesetz und das Mineralölsteuergesetz 1995 geändert werden - Ökologisierungsgesetz 2007 ÖkoG2007*. Bundesrepublik Österreich, 2008.
- [Cha02] P. D. Chandana. *Sensorless Control of Permanent-Magnet Synchronous Motor Drives*. PhD thesis, Aalborg University, 2002.

- [dCAF12] R. de Castro, R. E. Araújo, and D. Freitas. Wheel Slip Control of EVs based on Sliding Mode Technique with Conditional Integrators. In *IEEE Transactions on Industrial Electronics*, 2012.
- [DDKAF11] M. Duval-Destin, Th. Kropf, V. Abadie, and M. Fausten. Auswirkungen eines Elektroantriebs auf das Bremssystem. *ATZ - Automobiltechnische Zeitschrift*, 113:638–643, 2011.
- [Deu89] Deutsches Institut für Normung. ISO 7401: Straßenfahrzeuge - Testverfahren für querdynamisches Übertragungsverhalten. 1989.
- [Deu94] Deutsches Institut für Normung. DIN 70000 - Fahrzeugdynamik und Fahrverhalten. 1994.
- [ERWL05] A. Emadi, K. Rajashekara, S. S. Williamson, and S. M. Lukic. Topological overview of hybrid electric and fuel cell vehicular power system architectures and configurations. In *IEEE Transactions on Vehicular Technology*, 2005.
- [Eur07] European Union. *Verordnungen des europäischen Parlaments Verordnung (EG) Nr. 715/2007 des europäischen Parlaments und des Rates*. European Union, 2007.
- [Eur10] European Union. EU Energy and Transport in Figures; Statistical Pocketbook 2010. Technical report, Publication Office of the European Union, 2010.
- [Fac99] M. Fach. *Lokale Effekte der Reibung zwischen Pkw-Reifen und Fahrbahn*. PhD thesis, Technische Universität Darmstadt, 1999.
- [Fei12] H. J. Feigel. Integriertes Bremssystem ohne funktionale Kompromisse. *ATZ - Automobiltechnische Zeitschrift*, 114:612–617, 2012.
- [Föll93] O. Föllinger. *Nichtlineare Regelungen II*. Oldenbourg Verlag, 1993.
- [Föll08] O. Föllinger. *Regelungstechnik-Einführung in die Methoden und ihre Anwendung*. Hüthig, 2008.
- [FLH13] J. Feustel, St. Lang, and M. Hand. Der Supersportwagen SLS AMG Electric Drive. *ATZ - Automobiltechnische Zeitschrift*, 115:8–15, 2013.
- [HE08] B. Heissing and M. Ersoy. *Fahrwerkshandbuch*. Friedrich Vieweg & Sohn, 2008.
- [HHR08] M. Horn, A. Hofer, and M. Reichhartinger. Control of an electronic throttle valve based on concepts of sliding-mode control. In *International Conference on Control Applications*, 2008.
- [Hir07] W. Hirschberg. TM simple 4.0: A Simple to Use Tyre Model. Technical report, Graz University of Technology, 2007.
- [Hof10] P. Hofmann. *Hybridfahrzeuge*. Springer-Verlag, 2010.

- [HR08] M. Horn and M. Reichhartinger. Second-order sliding mode control of electronic throttle valves. In *International Workshop on Variable Structure Systems*, 2008.
- [HS09] St. Hillenbrand and I. Stolpe. Optimierung der Reibwertausnutzung der Reifendurch aktive Antriebsmomentenverteilung. In *at-Automatisierungstechnik*, volume 57, pages 223–229. Oldenbourg Wissenschaftsverlag, 2009.
- [IKYK94] S. Ingaki, I. Kshiro, M. Yamamoto, and T. Kaisha. Analysis on vehicle stability in critical cornering using phase-plane method. *Proc. of the International Symposium on Advanced Vehicle Control*, 1994.
- [Int06] International Organization for Standardization. ISO 9816: Passenger cars - Power off reaction of a vehicle in a turn - Open-loop test method. 2006.
- [Int11a] International Energy Agency. CO<sub>2</sub> emission from fuel combustion. Technical report, International Energy Agency, 2011.
- [Int11b] International Energy Agency. Technology Roadmap - Electric and plug-in hybrid electric vehicles. Technical report, International Energy Agency, 2011.
- [Int11c] International Organization for Standardization. ISO 3888-2: Passenger cars - Test track for a severe lane-change manoeuvre. 2011.
- [Int12a] International Organization for Standardization. ISO 26262-1:2012: Road vehicles-Functional safety-Part 10: Guideline on ISO 26262. 2012.
- [Int12b] International Organization for Standardization. ISO/CD 26262:2012: Road vehicles-Functional safety. 2012.
- [Ise06] R. Isermann. *Fahrdynamik-Regelung*. Friedrich Vieweg & Sohn, 2006.
- [Jaz09] R. N. Jazar. *Vehicle Dynamics - Theory and Application*. Springer-Verlag, 2009.
- [JC99] T. M. Jahns and V. Caliskan. Uncontrolled Generator Operation of Interior PM Synchronous Machines Following High-Speed Inverter Shutdown. In *IEEE Transactions on Industry Applications*, 1999.
- [Jon09] M. Jonasson. *Exploiting individual wheel actuators to enhance vehicle dynamics and safety in electric vehicles*. PhD thesis, Royal Institute of Technology Stockholm, 2009.
- [KAKH08] W. Kober, U. Angeringer, M. Kreutz, and M. Horn. Vernetzung von Längs- und Querdynamikregelungsfunktionen bei Einsatz von aktiven Fahrwerks- und Antriebsstrangkomponenten. In *4. VDI Fachtagung Steuerung und Regelung von Fahrzeugen und Motoren - AUTOREG*, 2008.
- [Kha96] H. K. Khalil. *Nonlinear systems*. Prentice Hall, 1996.

- [KN00] U. Kiencke and L. Nielsen. *Automotive control systems*. Springer-Verlag, 2000.
- [Kra06] F. Kramer. *Passive Sicherheit von Kraftfahrzeugen*. Friedrich Vieweg & Sohn, 2006.
- [Kra07] F. Kramer. Aktive und passive Sicherheit. In H. Burg and A. Moser, editors, *Handbuch Verkehrsunfallrekonstruktion*. Vieweg, 2007.
- [Kri01] R. Krishnan. *Electric Motor Drives: Modelling, Analysis, and Control*. Prentice Hall, 2001.
- [LEH11] C. Lex, A. Eichberger, and W. Hirschberg. Methoden zur Ermittlung des Reifen-Fahrbahn-Kraftschlusspotentials für Fahrerassistenzsysteme. *ATZ - Automobiltechnische Zeitschrift*, 113:992–997, 2011.
- [LMSN05] E. K. Liebemann, K. Meder, J. Schuh, and G. Nenninger. Safety and Performance Enhancement: The Bosch Electronic Stability Control (ESP). Robert Bosch, 2005.
- [LS08] D. Lindvai-Soos. Entwurf und Bewertung von Fahrdynamik-Regelstrategien. Master’s thesis, Graz University of Technology, 2008.
- [LSH13] D. Lindvai-Soos and M. Horn. Modelling, control and implementation of an electro-mechanic braking force actuator for hev and ev. In *IFAC Symposium on Advances in Automotive Control*, 2013.
- [Lun08] J. Lunze. *Regelungstechnik 2*. Springer-Verlag, 2008.
- [MGB07] M. Meyer, T. Grote, and J. Böcker. Direct Torque Control for Interior Permanent Magnet Synchronous Motor with Respect to Optimal Efficiency. In *European Conference on Power Electronics and Applications*, 2007.
- [MM95] W. F. Milliken and D. L. Milliken. *Race Car Vehicle Dynamics*. Society of Automotive Engineers, 1995.
- [MW04] M. Mitschke and H. Wallentowitz. *Dynamik der Kraftfahrzeuge*. Springer-Verlag, 2004.
- [NAI13] NAIAS LCC. North American International Auto Show. <http://www.naias.com/>, 2013. [Online; last accessed 30-March-2013].
- [Nat07] National Highway Traffic Safety Administration. *Federal Motor Vehicle Safety Standard - Electronic Stability Control Systems, 49 CFR Parts 571 & 585*. National Highway Traffic Safety Administration, 2007.
- [Ore06] R. Orend. *Integrierte Fahrdynamikregelung mit Einzelradaktorik*. Shaker Verlag, 2006.
- [Pfe11] P. Pfeffer. Neuheiten beim Chassis: Potentiale und Innovationsfelder. *ATZ - Automobiltechnische Zeitschrift*, 113:971–989, 2011.

- [Pla08] G. Plapp. Future Brake Systems for Future Powertrain Technology. *brake.tech 2008*, 2008.
- [Ram05] F. Ramusch. Methoden zur Komplexitätsreduktion bei der Berechnung des Gierratensollwerts für Fahrzeugregelsysteme. Master's thesis, Carinthia University of Applied Sciences, 2005.
- [Ras09] Th. Raste. Fahrerassistenz auf Stabilisierungsebene. In *Handbuch Fahrerassistenzsysteme*. Winner, H. and Hakuli, St. and Wolf, G., 2009.
- [Rau07] M. Rau. *Koordination aktiver Fahrwerk-Regelsysteme zur Beeinflussung der Querdynamik mittels Verspannungslenkung*. PhD thesis, University of Stuttgart, 2007.
- [Rei07] K. Reif. *Automobilelektronik*. Vieweg & Teubner, 2007.
- [RH11] M. Ringdorfer and M. Horn. A Robust Wheel Slip Controller for a Hybrid Braking System. In *International Conference on Control, Automation, Robotics and Vision*, 2011.
- [Rie09] P. Rieth. Das mechatronische Fahrwerk der Zukunft. In *Handbuch Fahrerassistenzsysteme*. Winner, H. and Hakuli, St. and Wolf, G., 2009.
- [RS40] P. Riekert and T. E. Schunck. Zur Fahrmechanik des gummiereiften Kraftfahrzeugs. *Archives of Applied Mechanics*, 11:2101–224, 1940.
- [SBTF03] R. Schwarz, U. Bauer, St. Tröster, and St. Fritz. ESP 2 Fahrdynamik der nächsten Generation. *ATZ - Automobiltechnische Zeitschrift*, 105:1178–1182, 2003.
- [Sch04] T. Schrüllkamp. Fahrwerksentwicklung an ika und fka. In *Tag des Fahrwerks 2004*, 2004.
- [SE02] W. L. Soong and N. Ertugrul. Field-Weakening Performance of Interior Permanent-Magnet Motors. In *Transactions of Industry Applications*, 2002.
- [Shi06] J. Shi. Integrated Global Chassis Control - A Top-Down Design Approach. In *Proceedings of the Vehicle Dynamics Expo*, 2006.
- [SL99] J. J. Slotine and W. Li. *Applied Nonlinear Control*. Prentice Hall, 1999.
- [Sma00] H. Smakman. *Functional Integration of Slip Control with Active Suspension for Improved Lateral Vehicle Dynamics*. PhD thesis, Technical University Delft, 2000.
- [SP96] S. Skogestad and I. Postlethwaite. *Multivariable feedback control: analysis and design*. John Wiley & Sons, 1996.
- [SSWM11] R. Schwarz, S. Strasser, M. Wein, and J. Maerkl. The electric quattro - opportunities and challenges. *chassis.tech plus 2011*, pages 785–793, 2011.

- [STP11] R. Stroph, M. Teitzer, and A. Pruckner. Simulation eines ABS-Systems in Kombination mit generatorischem Bremsen mittels E-Antrieben. *ATZe - Automobiltechnische Zeitschrift elektronik*, 6:58–62, 2011.
- [Tod11] J. Todt. Promoting advanced vehicle safety technologies. Technical report, eSafetyAware, 2011.
- [Trä05] A. Trächtler. Integrierte Fahrdynamikregelung mit ESP, aktiver Lenkung und aktivem Fahrwerk. In *at-Automatisierungstechnik*, volume 53, pages 11–19. Oldenbourg Wissenschaftsverlag, 2005.
- [UGS99] V. Utkin, J. Guldner, and J. Shi. *Sliding Mode Control in Electromechanical Systems*. CRC Press, 1999.
- [VB08] P. Vaclavek and P. Blaha. Interior Permanent Magnet Synchronous Machine High Speed Operation using Field Weakening Control Strategy. In *International Conference on Systems*, 2008.
- [Ver13] Verband der Automobilindustrie. IAA - Internationale Automobilausstellung. <http://www.iaa.de/>, 2013. [Online; last accessed 30-March-2013].
- [VHG10] Ch. Voser, R. Y. Hindiyeh, and J. Ch. Gerdes. Analysis and control of high sideslip manoeuvres. In *Vehicle System Dynamics*, volume 48, pages 317–336, 2010.
- [Vol13] Volvo Car Group, Global Newsroom. Volvo Recharge Concept . <https://www.media.volvocars.com/global/en-gb/media/photos/12201>, 2013. [Online; last accessed 08-October-2013].
- [VZ05] A. Van Zanten. In *Fahrdynamik und Fahrdynamikregelsysteme*. Car Training Institute, 2005.
- [Wag06] M. Wagner. *Gleichzeitige Nutzung von längs-, quer- und vertikaldynamisch wirkenden Regelsystemen für Personenkraftwagen*. VDI Verlag GmbH, 2006.
- [Web05] I. Weber. *Verbesserungspotential von Stabilisierungssystemen im Pkw durch eine Reibwertsensorik*. PhD thesis, Technische Universität Darmstadt, 2005.
- [Wil02] G. Wilson. *Embedded systems and computer architecture*. Reed Educational and Professional Publishing Ltd, 2002.
- [Wil11] J. Willberger. *AC Motor Design for Passenger Cars - Design and Energy Efficient Control of In-Wheel Motors*. PhD thesis, Graz University of Technology, 2011.
- [YTS<sup>+</sup>10] M. Yamakado, J. Takahashi, S. Saito, A. Yokoyama, and M. Abe. Improvement in vehicle agility and stability by g-vectoring control. In *Vehicle System Dynamics*, volume 48, pages 231–254, 2010.
- [Zeh07] J. Zehetner. *Automotive Regelungssysteme - Ansätze und Werkzeuge zur strukturvariablen Regelung*. PhD thesis, Graz University of Technology, 2007.

# List of Figures

1.1	Passenger travel and road accident statistics [Eur10]	14
1.2	Road accident and fatality statistics	14
1.3	Active and passive safety [Kra06]	15
1.4	Active and passive safety systems [Sch04]	15
1.5	CO <sub>2</sub> emission statistics [Int11a]	16
1.6	Annual global EV and PHEV sales [Int11b]	17
1.7	Structures of electrical and hybrid electrical drivetrains [Hof10]	18
1.8	EV concept drivetrain (with kind permission of [Vol13])	19
1.9	Electric vehicle topology	20
1.10	Thesis content structure	21
2.1	Longitudinal tire force characteristic	23
2.2	ABS control loop [Ise06] (with adaptations by the author)	23
2.3	Typical ABS control cycle [KN00]	24
2.4	Typical ABS cycle for high- $\mu$ braking	25
2.5	Vehicle motion and traction force potential on $\mu$ -split conditions	25
2.6	Typical ABS cycle for split- $\mu$ braking	26
2.7	Yaw motion control interventions [Ant08]	27
2.8	ESC control loop [Rau07] (with adaptations by the author)	27
2.9	Parallel vehicle control system structure	28
2.10	Combined vehicle control system structure	29
2.11	Hybrid actuator system	30
2.12	Chassis /Drivetrain topology	31
3.1	Wheel coordinate system and tire forces	32
3.2	Longitudinal/lateral tire forces for different road friction coefficients $\mu$	33
3.3	TM simple tire forces parameters	34
3.4	Combined TM simple tire forces	35
3.5	<i>Kamm's</i> circle	36
3.6	Tire force approximation	37
3.7	Vehicle geometries	38
3.8	Wheel motion model	38
3.9	Bicycle model	39
3.10	Two-track model	41
4.1	Conventional brake system	43

4.2	HEV/EV brake system . . . . .	43
4.3	Brake system response . . . . .	44
4.4	Permanent magnet electric machines classification [Cha02] . . . . .	45
4.5	PMSM rotor magnet locations [Cha02] . . . . .	46
4.6	PMSM torque characteristic . . . . .	46
4.7	B6-Inverter bridge . . . . .	47
4.8	Three-phase system . . . . .	47
4.9	Coordinate transformation: a-b-c system $\leftrightarrow$ $\alpha$ - $\beta$ system $\leftrightarrow$ d-q system . . .	48
4.10	Control loop for field-oriented control . . . . .	50
4.11	PMSM decoupling network . . . . .	50
4.12	Reference currents for Maximum Torque Per Ampere mode . . . . .	52
4.13	Field-weakening constraints . . . . .	54
4.14	Reference currents for constant torque during field weakening . . . . .	54
4.15	Phasor diagram of PMSM during uncontrolled generator mode operation . .	56
4.16	PMSM malfunction torques . . . . .	58
4.17	Traction machine response (PMSM) . . . . .	59
4.18	PMSM representation . . . . .	59
5.1	Vehicle dynamics control topology (ESC) . . . . .	61
5.2	Wheel motion control loop . . . . .	61
5.3	Conventional EV/HEV topology (ESC and EM) . . . . .	61
5.4	Wheel motion control loop (EV) . . . . .	62
5.5	Brake control . . . . .	63
5.6	Torque response based to the friction brake . . . . .	64
5.7	Combined EV/HEV topology (VDC and EM) . . . . .	65
5.8	Wheel motion control loop (combined control) . . . . .	66
5.9	Traction machine control . . . . .	67
5.10	Torque response with combined actuator control ( $\mathcal{P}_1$ ) . . . . .	68
5.11	Torque response with combined actuator control ( $\mathcal{P}_2$ : fast response) . . . .	69
6.1	Model uncertainty . . . . .	73
6.2	ABS braking under high- $\mu$ conditions . . . . .	77
6.3	ABS braking under low- $\mu$ conditions . . . . .	78
6.4	HAS braking under high- $\mu$ conditions . . . . .	79
6.5	HAS braking under low- $\mu$ conditions . . . . .	80
6.6	Longitudinal tire forces during ABS and HAS braking . . . . .	81
6.7	Wheel slip control using the conventional ABS (test bench) . . . . .	85
6.8	HAS wheel slip control using the friction brake (test bench) . . . . .	86
6.9	HAS wheel slip control using energy recuperation (test bench) . . . . .	87
6.10	HAS wheel slip control using energy recuperation and friction brake (test bench) . . . . .	89
7.1	Yaw motion reference values for high- $\mu$ . . . . .	91
7.2	VDC yaw rate control loop . . . . .	94
7.3	Estimation of yaw torque potential . . . . .	94
7.4	Yaw torque potential . . . . .	95
7.5	Torque coordinator . . . . .	97

7.6 VDC sideslip angle control loop . . . . . 99

7.7 Vehicle yaw motion phase plane (uncontrolled vehicle) . . . . . 101

7.8 Vehicle yaw motion phase plane (controlled vehicle) . . . . . 102

7.9 VDC system states during yaw motion control for different initial states . . 103

7.10 VDC braking under low- $\mu$  conditions. Both HAS actuators are utilized for vehicle deceleration as the traction machine cannot provide sufficient propulsion torque. The friction brake torque is reduced as soon as the recuperation torque increases. When the vehicle shows an unintended yaw motion, the friction brake torque on the left-hand side is reduced such that  $T_z \neq 0$ . The vehicle yaw motion is corrected without reducing recuperation. 105

7.11 VDC braking under split- $\mu$  conditions. As the right-hand side of the vehicle is at high- $\mu$ , the wheel torque can achieve higher absolute values than the left-hand side. This causes an introduction of unintended yaw motion. To keep the vehicle on a straight run, the friction brake torque is reduced based on  $T_z$ . Yaw motion control and a good braking performance can be achieved, as well as energy recuperation. . . . . 106

7.12 Steering wheel step (bird’s-eye view). For high- $\mu$ , nearly the same cornering performance for ESC and VDC is observable. At low- $\mu$ , the determination of  $\dot{\psi}_d$  requires the consideration of  $a_y$  in order to prevent the vehicle from spinning. Although the VDC reduces sideslip angle, it causes a slightly increased cornering radius. . . . . 108

7.13 Steering wheel step. VDC applications can achieve less yaw rate overshoot and less sideslip angle overshoot. The correction torque is calculated when the yaw rate control and sideslip angle control are active.  $T_z$  results from different propulsion torques of the rear axle HAS. . . . . 109

7.14 Power lift-off. The application of VDC results in less deviation from the comparative signal values and a reduced path deviation. The induced reaction of the VDC-equipped vehicle is less marked compared to the vehicle equipped with ESC. . . . . 111

7.15 Power lift-off (bird’s-eye view). Due to the faster vehicle response, the vehicle applying VDC shows a better oversteering suppression performance. 112

7.16 Steering wheel input for the sine with dwell maneuver . . . . . 112

7.17 Sine with dwell. Electric torque vectoring improves the stabilization performance of the vehicle (reduced sideslip angle and higher yaw rate convergence speed). It requires control mode changes where recuperated energy is transferred from the right wheel corner to the left wheel corner, or where the left wheel corner is switched off. . . . . 113

7.18 Sine with dwell (bird’s-eyes view) . . . . . 114

7.19 VDA lane change. Applying the VDC leads to a reduced sideslip angle. Additionally, the vehicle velocity can be increased due to torque vectoring functionality. . . . . 115

7.20 VDA lane change (bird’s-eye view) . . . . . 115

7.21 VDA lane change (bird’s-eye view zoomed). The reduced vehicle oversteering leads to a slightly different trajectory. This enables the increase of the longitudinal velocity. . . . . 116

8.1 HAS braking under low- $\mu$  conditions and machine short circuit on the right-hand side. When the short circuit appears, the recuperation torque on the right-hand side changes immediately. The friction brake increases brake pressure in order to compensate for the missing wheel torque. At lower speeds, the brake pressure is reduced as the recuperation torque increases. . . . . 118

8.2 HAS braking under low- $\mu$  conditions and passive recuperation on the right-hand side. When the fault occurs, the wheel speed on the right-hand side changes immediately, and the recuperation torque is nearly constant for a second. A friction brake intervention is required when the recuperation is zero. From that time onwards, the friction brake maintains the wheel motion control. 120

8.3 HAS braking under high- $\mu$  conditions and machine short circuit on the right-hand side. As soon as the recuperation torque reaches low values due to the machine short circuit, the friction brake increases brake pressure. The tire force potential is sufficiently high to maintain a desired wheel motion. 122

8.4 HAS braking under high- $\mu$  conditions and passive recuperation on the right-hand side. When the fault appears, the friction brake increases brake pressure. The brake pressure is adapted to achieve a desired wheel motion. When the recuperation torque reaches zero, the friction brake controls the right wheel motion, while the traction machine controls the wheel motion on the left-hand side. . . . . 123

8.5 Comparison of different system faults during split- $\mu$  braking (yaw control performance). It is possible to maintain safe vehicle motion for all driving situations except for case e. Although the yaw motion controller tries to correct the vehicle motion, large values in the yaw rate and in the sideslip angle arise. . . . . 124

8.6 Comparison of different system faults during split- $\mu$  braking (bird's-eye view). Immediately after the fault occurs, a yaw torque is introduced into the vehicle. In the last case, an undesired yaw motion arises. As soon as the recuperation torque is zero, the vehicle can be stabilized. . . . . 126

8.7 Passive recuperation on the right-hand side during straight-ahead driving. The driver must establish a wheel steering angle of  $\approx 10^\circ$ . The control system is parameterized such that the vehicle speed is slowly reduced below the critical wheel. . . . . 127

8.8 Comparison of passive recuperation on different rear axle wheels during vehicle cornering. When the fault occurs on the left-hand side, the induced yaw torque causes a fast increase of the yaw rate and the sideslip angle. The control system forces the vehicle to reduce speed immediately. As soon as the recuperation torque on the inner wheel reaches zero, the vehicle can be stabilized. . . . . 129

8.9 Comparison of passive recuperation on different rear axle wheels during vehicle cornering (bird's-eye view). From the bird's-eye view, it is clearly visible, that the fault on the rear right wheel (outer wheel) has almost no impact on the cornering performance. Only the yaw torque induced by the rear left wheel causes oversteering behaviour. . . . . 130

A.1	Sliding mode control with/without boundary layer . . . . .	136
A.2	Sliding mode control . . . . .	137
B.1	Test bench . . . . .	140
B.2	Test bench (schematic) . . . . .	140
B.3	Test bench software structure . . . . .	142
B.4	ABS valve block (schematic layout) . . . . .	142
B.5	Stickslip in the hydraulic circuit during pressure increase . . . . .	143
B.6	Stickslip in the hydraulic circuit during pressure decrease . . . . .	143
B.7	Wheel slip variation due to load force change . . . . .	144
B.8	Vertical loads force variation . . . . .	144

# List of Tables

1	Vehicle related symbols . . . . .	9
2	Vehicle dynamics controller related symbols . . . . .	10
3	Traction drive related symbols . . . . .	11
4	Mathematical and control related symbols . . . . .	12
6.1	Simulation results for ABS/HAS braking . . . . .	82
6.2	Simulation results for ABS/HAS braking (robustness) . . . . .	83
6.3	Test bench results for ABS and HAS braking . . . . .	88
7.1	Simulation results for emergency braking . . . . .	107
7.2	Simulation results for steering wheel step . . . . .	108
7.3	Simulation results for power lift-off . . . . .	110
7.4	Simulation results for sine with dwell . . . . .	111
7.5	Simulation results for the VDA lane change . . . . .	114
7.6	Summary of simulation results . . . . .	116
8.1	Simulation results for low- $\mu$ braking . . . . .	119
8.2	Simulation results for high- $\mu$ braking . . . . .	121
8.3	Simulation results for split- $\mu$ braking . . . . .	125
8.4	Simulation results for vehicle cornering . . . . .	128
8.5	Summary of fault test simulation results . . . . .	131